20 years of research on the Alcator C-Mod tokamak a)

M. Greenwald, A. Bader, S. Baek, M. Bakhtiari, H. Barnard, W. Beck, W. Bergerson, I. Bespamyatnov, P. Bonoli, D. Brower, D. Brunner, W. Burke, J. Candy, M. Churchill, I. Cziegler, A. Diallo, A. Dominguez, B. Duval, E. Edlund, P. Ennever, D. Ernst, I. Faust, C. Fiore, T. Fredian, O. Garcia, C. Gao, J. Goetz, T. Golfinopoulos, R. Granetz, O. Grulke, Z. Hartwig, S. Horne, N. Howard, A. Hubbard, J. Hughes, I. Hutchinson, J. Irby, V. Izzo, C. Kessel, B. LaBombard, C. Lau, C. Li, Y. Lin, B. Lipschultz, A. Loarte, E. Marmar, A. Mazurenko, G. McCracken, R. McDermott, O. Meneghini, D. Mikkelsen, D. Mossessian, R. Mumgaard, J. Myra, E. Nelson-Melby, R. Ochoukov, G. Olynyk, R. Parker, S. Pitcher, Y. Podpaly, M. Porkolab, M. Reinke, J. Rice, W. Rowan, A. Schmidt, S. Scott, S. Shiraiwa, J. Sierchio, N. Smick, J. A. Snipes, P. Snyder, B. Sorbom, J. Stillerman, C. Sung, Y. Takase, V. Tang, J. Terry, D. Terry, C. Theiler, A. Tronchin-James, N. Tsujii, R. Vieira, J. Walk, G. Wallace, A. White, D. Whyte, J. Wilson, S. Wolfe, G. Wright, J. Wright, S. Wukitch, and S. Zweben

Articles you may be interested in

Stationary density profiles in the Alcator C-mod tokamak
Phys. Plasmas **19**, 122511 (2012); 10.1063/1.4773215

Wide-view charge exchange recombination spectroscopy diagnostic for Alcator C-Moda)
Rev. Sci. Instrum. **79**, 10F529 (2008); 10.1063/1.2979865

Operation of Alcator C-Mod with high-Z plasma facing components and implicationsa)
Phys. Plasmas **13**, 056117 (2006); 10.1063/1.2180767

Edge-localized mode dynamics and transport in the scrape-off layer of the DIII-D tokamak
Phys. Plasmas **12**, 072516 (2005); 10.1063/1.1949224

Active and fast particle driven Alfvén eigenmodes in Alcator C-Moda)
Phys. Plasmas **12**, 056102 (2005); 10.1063/1.1865012

20 years of research on the Alcator C-Mod tokamak[a)]

M. Greenwald,[1,b)] A. Bader,[2] S. Baek,[1] M. Bakhtiari,[2] H. Barnard,[1] W. Beck,[1]
W. Bergerson,[3] I. Bespamyatnov,[4] P. Bonoli,[1] D. Brower,[3] D. Brunner,[1] W. Burke,[1]
J. Candy,[5] M. Churchill,[6] I. Cziegler,[7] A. Diallo,[6] A. Dominguez,[6] B. Duval,[8] E. Edlund,[6]
P. Ennever,[1] D. Ernst,[1] I. Faust,[1] C. Fiore,[1] T. Fredian,[1] O. Garcia,[9] C. Gao,[1] J. Goetz,[2]
T. Golfinopoulos,[1] R. Granetz,[1] O. Grulke,[10] Z. Hartwig,[1] S. Horne,[11] N. Howard,[12]
A. Hubbard,[1] J. Hughes,[1] I. Hutchinson,[1] J. Irby,[1] V. Izzo,[7] C. Kessel,[6] B. LaBombard,[1]
C. Lau,[13] C. Li,[1] Y. Lin,[1] B. Lipschultz,[14] A. Loarte,[15] E. Marmar,[1] A. Mazurenko,[16]
G. McCracken,[17] R. McDermott,[18] O. Meneghini,[5] D. Mikkelsen,[6] D. Mossessian,[19]
R. Mumgaard,[1] J. Myra,[20] E. Nelson-Melby,[21] R. Ochoukov,[18] G. Olynyk,[22] R. Parker,[1]
S. Pitcher,[15] Y. Podpaly,[23] M. Porkolab,[1] M. Reinke,[14] J. Rice,[1] W. Rowan,[4] A. Schmidt,[24]
S. Scott,[6] S. Shiraiwa,[1] J. Sierchio,[1] N. Smick,[25] J. A. Snipes,[15] P. Snyder,[5] B. Sorbom,[1]
J. Stillerman,[1] C. Sung,[1] Y. Takase,[26] V. Tang,[24] J. Terry,[1] D. Terry,[1] C. Theiler,[8]
A. Tronchin-James,[27] N. Tsujii,[26] R. Vieira,[1] J. Walk,[1] G. Wallace,[1] A. White,[1] D. Whyte,[1]
J. Wilson,[6] S. Wolfe,[1] G. Wright,[1] J. Wright,[1] S. Wukitch,[1] and S. Zweben[6]

[1]*MIT Plasma Science and Fusion Center, Cambridge, Massachusetts 02139, USA*
[2]*Department of Physics, University of Wisconsin, Madison, Wisconsin 53706, USA*
[3]*UCLA, Institute of Plasma and Fusion Research, Los Angeles, California 90095, USA*
[4]*Fusion Research Center, University of Texas, Austin, Texas 78712, USA*
[5]*General Atomics, P.O. Box 85608, San Diego, California 92186, USA*
[6]*Princeton Plasma Physics Laboratory, Princeton, New Jersey 08540, USA*
[7]*Center for Momentum Transport and Flow Organization, UCSD, San Diego, California 92093, USA*
[8]*Ecole Polytechnique Federale de Lausanne, Centre de Recherches en Physique des Plasmas, Lausanne 1015, Switzerland*
[9]*Department of Physics and Technology, University of Tromsø, N-9037 Tromsø, Norway*
[10]*MPI for Plasma Physics, EURATOM Association, D-17491 Greifswald, Germany and Ernst-Moritz-Arndt University, D-17489 Greifswald, Germany*
[11]*Energetiq Technology, 7 Constitution Way, Woburn, Massachusetts 01801, USA*
[12]*Oak Ridge Institute for Science and Education (ORISE), Oak Ridge, Tennessee 37830, USA*
[13]*ORNL, P.O. Box 2008, Oak Ridge, Tennessee 37831, USA*
[14]*York University, Heslington, York YO10 5DD, United Kingdom*
[15]*ITER Organization, 13067 St. Paul-lez-Durance, France*
[16]*Block Engineering, 377 Simarano Dr., Marlborough, Massachusetts 01752, USA*
[17]*UKAEA Culham Centre for Fusion Energy, Abingdon, OX14 3DB Oxfordshire, United Kingdom*
[18]*MPI für Plasmaphysik, EURATOM-Association, D-85748 Garching, Germany*
[19]*AllianceBernstein, 1345 Avenue of the Americas, New York, New York 10105, USA*
[20]*Lodestar Research Corporation, 2400 Central Avenue P-5, Boulder, Colorado 80301, USA*
[21]*Raytheon Co., 1151 E Hermans Rd., Tucson, Arizona 85756, USA*
[22]*McKinsey & Co., 110 Charles Street West, Toronto, Ontario M5S 1K9, Canada*
[23]*National Institute of Science and Technology, 100 Bureau Drive, Stop 1070, Gaithersburg, Maryland 20899, USA*
[24]*LLNL, 7000 East Ave., Livermore, California 94550, USA*
[25]*GT Advanced Technologies, 243 Daniel Webster Highway, Merrimack, New Hampshire 03054, USA*
[26]*University of Tokyo, Tokyo 113-033, Japan*
[27]*Facebook LLC, 1601 Willow Road, Menlo Park, California 94205, USA*

The object of this review is to summarize the achievements of research on the Alcator C-Mod toka-mak [Hutchinson *et al.*, Phys. Plasmas **1**, 1511 (1994) and Marmar, Fusion Sci. Technol. **51**, 261 (2007)] and to place that research in the context of the quest for practical fusion energy. C-Mod is a compact, high-field tokamak, whose unique design and operating parameters have produced a wealth of new and important results since it began operation in 1993, contributing data that extends tests of critical physical models into new parameter ranges and into new regimes. Using only high-power radio frequency (RF) waves for heating and current drive with innovative launching structures, C-Mod operates routinely at reactor level power densities and achieves plasma pressures higher than any other toroidal confinement device. C-Mod spearheaded the development of the vertical-target divertor and has always operated with high-Z metal plasma facing components—approaches subsequently adopted for ITER. C-Mod has made ground-breaking discoveries in diver-tor physics and plasma-material interactions at reactor-like power and particle fluxes and elucidated

---

[a)]Paper AR1 1, Bull. Am. Phys. Soc. **58**, 21 (2013).
[b)]Invited speaker.

the critical role of cross-field transport in divertor operation, edge flows and the tokamak density limit. C-Mod developed the I-mode and the Enhanced Dα H-mode regimes, which have high performance without large edge localized modes and with pedestal transport self-regulated by short-wavelength electromagnetic waves. C-Mod has carried out pioneering studies of intrinsic rotation and demonstrated that self-generated flow shear can be strong enough in some cases to significantly modify transport. C-Mod made the first quantitative link between the pedestal temperature and the H-mode's performance, showing that the observed self-similar temperature profiles were consistent with critical-gradient-length theories and followed up with quantitative tests of nonlinear gyrokinetic models. RF research highlights include direct experimental observation of ion cyclotron range of frequency (ICRF) mode-conversion, ICRF flow drive, demonstration of lower-hybrid current drive at ITER-like densities and fields and, using a set of novel diagnostics, extensive validation of advanced RF codes. Disruption studies on C-Mod provided the first observation of non-axisymmetric halo currents and non-axisymmetric radiation in mitigated disruptions. A summary of important achievements and discoveries are included. © *2014 AIP Publishing LLC*. [http://dx.doi.org/10.1063/1.4901920]

I. INTRODUCTION—ADVANTAGES OF HIGH MAGNETIC-FIELD FOR FUSION

While it is common and correct to frame pure plasma physics phenomena in terms of dimensionless plasma parameters,[1,2] practical fusion energy requires prescribed levels of absolute performance. This can be easily understood as a consequence of non-plasma dimensionless parameters, particularly the ratio of plasma temperature to the characteristic energies required for the fusion nuclear reaction ($kT/E_{nuclear}$) and to the characteristic energies for atomic ionization, recombination, and molecular bonding (kT/E_{atomic}). The first of these leads directly to the Lawson criterion for the minimum ion temperature in an energy producing fusion plasma. The second is important for edge plasma and plasma-wall interactions and will be discussed in Secs. I A and III. Economic and engineering considerations dictate the optimum level of neutron wall loading in a fusion reactor[3] (about 3–4 MW/m^2) and consequently to an optimum absolute plasma pressure and density. At the same time, all of the operating limits for a tokamak increase with the magnetic field; the maximum plasma current, which largely determines confinement, and the maximum plasma density are proportional to B,[4,5] and the maximum pressure is proportional to B^2.[6] Thus, absolute performance increases with field, as does robustness against disruptions due to the proximity of operational limits. It is worth noting that the requirement for operation near an optimum density can be problematic for very large low-field fusion reactor designs, since this density range may be above the tokamak density limit.[7] Prospective tokamak reactor designs like ARIES-AT assume operation near or above all of these limits[8] raising concern about achieving this level of performance and robustness with respect to disruptions. Research at fusion-relevant absolute parameters is required since the plasma and non-plasma physics couple in complicated ways that are well beyond our current abilities to model.

The economic advantage of high fields can be understood by considering the total fusion power from a tokamak device, which is proportional to $(\beta_N/q)^2 R^3 B^4$, where β_N is the plasma pressure normalized to the Troyon limit[6] and q is the tokamak "safety" factor, the inverse of the rotational transform. Plasma physics sets the upper limit for β_N and the lower limit for q. The overall cost for a fusion facility is proportional to the mass of the fusion "core" and thus to the magnetic stored energy $\propto R^3 B^2$. From these arguments, it is clear that the most cost effective fusion devices would operate with the highest fields that can be safely engineered. On several previous occasions when the U.S. was planning to build its own burning plasma devices, CIT, BPX, and FIRE,[9,10] the price to performance argument led to compact high-field designs. Looking forward and considering the substantial costs and extended construction schedule for ITER, which was designed with "well-known" moderate-field superconducting magnet technology, a development path that features higher field seems attractive.

A discussion of the practical limits for the strength of magnetic field in a fusion device is beyond the scope of this paper, but it is worth noting the opportunities presented by recent developments in high temperature superconductors. These materials, YBCO (Yttrium Barium Copper Oxide), for example, have demonstrated significantly higher critical currents at fields above 20 T.[11] By operating at elevated temperatures where heat capacities are higher, it should be possible to build magnets with field-demountable joints, allowing much more favorable modes for construction and maintenance. A design concept for a high-field pilot plant has been developed, demonstrating the advantages of this approach.[12] A limiting factor, of course, would be the ability to provide the mechanical support for the magnetic stresses produced by high-field magnets, though the design efforts described above suggest that this should be achievable.

A. Consequences of high-field operation in C-Mod

Alcator C-Mod is the third in a series of compact high-field tokamaks built and operated on the MIT campus.[13,14] Supporting the arguments provided above, these machines have demonstrated high performance at a moderate size and cost—the previous device, Alcator C, being the first controlled fusion experiment to exceed the Lawson product for density times confinement.[15] An important early goal of the C-Mod program was to provide a database that is relevant to high-field regimes. This goal encompassed support for the

design and operation of ITER, whose toroidal field (TF) of 5.4 T exceeds every other shaped and diverted tokamak in the world except for C-Mod. Table I provides a summary of basic parameters for the device.

    Operation at high field also allows attainment of uniquely ITER/reactor-relevant physics regimes. Consider, for example, the boundary plasma, where the plasma interacts with the wall, neutral fuel gas, and impurities. The nature of these interactions depends strongly on the plasma temperature normalized to atomic binding energies, which are on the order of a few eV. Thus, survival of plasma-facing components (PCMs) depends on lowering the plasma temperature at the interface to less than 10 eV. Fixing this value as a requirement for safe operation, the remaining boundary plasma parameters depend on the pressure. C-Mod, operating at reactor-like magnetic fields, operates at reactor-like boundary plasma pressures and thus has the same absolute power and particle loads, plasma density, and neutral opacity. As a consequence, a wide range of boundary phenomena can be studied directly on C-Mod, without resort to scaling arguments or excessive dependence on models. Similarly for radio frequency (RF) physics, C-Mod can run with the same cyclotron frequency (same field) and plasma frequency (same plasma density) as ITER and by carrying out experiments with the same RF frequencies can operate with identical wave physics. Figure 1 shows a selection of C-Mod parameters compared to other tokamaks and to the projected parameters for ITER. Data are taken from the International Tokamak Physics Activity (ITPA) H-mode database and also includes the C-Mod I-modes for comparison. These parameter plots are grouped based on the relevant physics—Fig. 1(a) plots ν^* vs β_N, which are important for core Magneto-Hydro-Dynamic (MHD), Fig. 1(b) shows ω_{pe} (electron plasma frequency) vs ω_{ce} (electron cyclotron frequency), which characterize RF physics, and Fig. 1(c) plots the parameters that characterize the boundary plasma challenge as discussed in Sec. III, PB/R vs plasma pressure (where the core pressure stands in as a proxy for the divertor pressure, for which a broad range of data is less available). At the same time, by operating in a unique range of field, input power, and size, C-Mod has made critical contributions to

multi-machine databases, which break parameter covariances when combined with larger low-field devices. For example, the inclusion of C-Mod data led to the ITER98 scalings for energy confinement in the H-mode, in which an unconstrained regression yielded a dimensionally correct fit.[16] Previous regressions carried out before C-Mod data were available were not dimensionally correct and in fact failed to predict the eventual C-Mod results, pointing out the risks in extrapolating from inadequately conditioned data.[17] In a
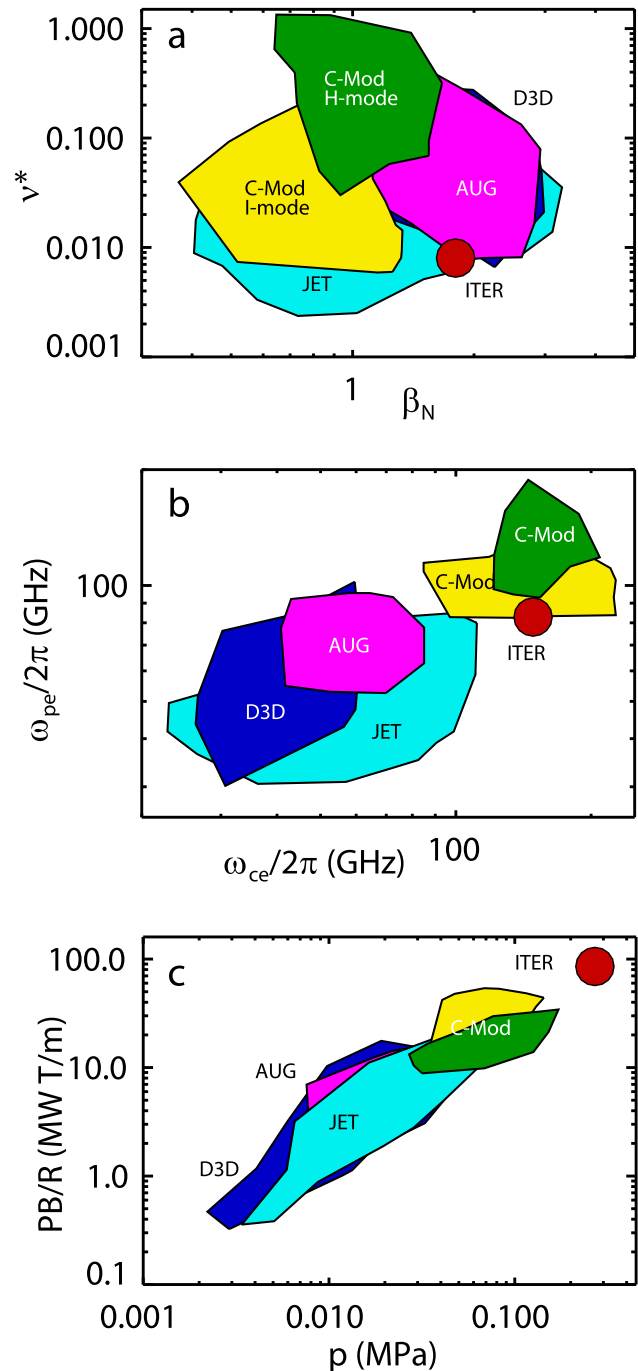

FIG. 1. C-Mod parameters are compared to other tokamaks and those projected for ITER as relevant to physics for (a) core MHD, (b) RF heating and current drive, and (c) boundary plasma physics where PB/R is a proxy for the divertor heat load and the core pressure a proxy for the divertor pressure. Data are mainly from the ITPA H-mode data base and includes C-Mod I-modes for comparison.

TABLE I. C-Mod physics parameters and symbols used in this manuscript.

Parameter	Symbol	Range	Units/definition
Major radius	R	0.67	M
Minor radius	a	0.22	M
Plasma elongation	κ	1.0–1.9	
Plasma triangularity	δ	0.0–0.85	
Plasma volume	V	1	m^3
Toroidal magnetic field	B_T	2.4–8.1	T
Plasma current	I_P	0.24–2.0	MA
Average plasma density	n_e	0.2–8.0	$10^{20}/m^3$
Central electron temperature	T_e	<9	keV
Central ion temperature	T_i	<6	keV
Average plasma pressure	p	<0.18	MPa
Normalized gyro-radius	ρ^*	0.002–0.006	ρ_i/a
Normalized pressure	β_N	<1.8	$\beta_T/I_P/aB_T$
Normalized collisionality	ν^*	0.06–1.0	$\nu_{ei}qR/\varepsilon^{3/2}v_i$

similar vein, C-Mod provided critical data for disruption physics, the L-H threshold, boundary plasmas, H-mode pedestals, and core particle transport used for defining the ITER operational baseline.[7,18] Given this background—the ability to operate in relevant regimes, with a good diagnostic set—it was inevitable that C-Mod would make a series of discoveries and address issues important for fusion energy.

II. C-MOD—FEATURES AND ENGINEERING

A. Magnets, structure, and control

C-Mod's unique physics capabilities flow directly from its high-field magnet technology.[19] The TF magnet consists of 20 6-turn copper coils carrying 225 kA at full field. Each coil is rectangular and composed of 4 straight segments with sliding joints at the corners. The joints are not pinned but rather are free to move under full current, transferring most of the magnetic stress from the coil to an external structure. The magnetic forces, which can reach up to 110 MN, are supported by a cylinder, 0.15 m thick, 4.9 m in diameter together with top and bottom domes, each 0.66 m thick with all three parts forged from high strength 316LN stainless steel and precision machined. The domes are fastened to the cylinder by 96 pretensioned INCONEL 718 drawbars forming a massive pressure vessel. Weighing about 30 tons each, the domes and cylinder were some of the largest stainless steel forgings ever made. A pair of monolithic wedge plates holds the magnet bundles in place and restrains the overturning forces of the magnet. Internal stresses in each bundle are supported by the high-strength copper and reinforced by stainless steel plates that are inserted, with insulation, between each turn. Figure 2 shows a schematic of the machine and the major components mentioned here. A great deal of R&D went into the felt-metal sliding connections that are the key to this design.[20] With 120 turns, each made of 4 segments, there are a 480 joints that must slide under full current and full mechanical load with minimal wear,
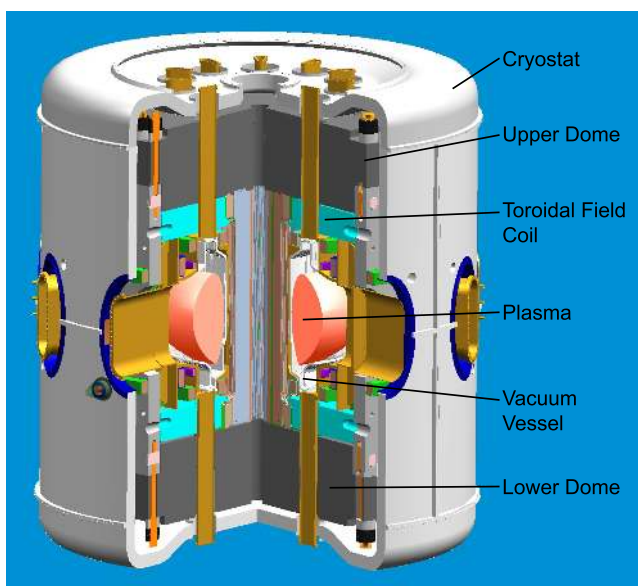
while maintaining very low electrical resistivity. Each joint has 4 felt-metal pads, with a total area of 72 cm^2, made of copper wire, sintered onto a copper substrate, silver plated, and coated with colloidal graphite. Spring-plates are hydraulically driven in between the TF joint fingers to provide the required contact pressure. The resulting resistance is below 1.5 $\mu\Omega$ for each joint. The TF magnet is disassembled for inspection roughly every 5000 pulses. The TF and poloidal field (PF) magnets are all cooled to LN$_2$ temperatures to reduce their electrical resistance. Thermal management in C-Mod is challenging, requiring that the vessel and ports be kept at room temperature while the magnets are kept cold. Clearances are small due to the compact size of the device. Table II provides a summary of C-Mod engineering parameters.

Another critical innovation was made in the buss connections, which bring power to several of the PF magnets. To accommodate the high current densities required and dimensional changes during heating and cooling, compliant buss connections were fabricated with electro-forming technology, an additive manufacturing process that produces stress-free high strength joints—compared to standard welding or brazing techniques, which anneal and weaken underlying material. The poloidal field magnets themselves are of more conventional design. The Ohmic Heating (OH) coil is made of 3 segments and is wound directly on the TF central column. The C-Mod OH coils require 30 kA currents to be supplied across magnetic fields above 17 T. A coaxial design allows the inner and outer conductor forces to react against each other to produce a very strong structure. The connection to the OH stack includes electric-discharge-machined 25 μm wide slots acting as springs along with a Belleville stack to provide compliance to the feltmetal contacts. This design has performed extremely well in handling both the extreme electromagnetic forces and the thermal stresses over many thousands of C-Mod shot cycles. The remaining PF coils are supported by the vacuum vessel, which is a structural element of the machine with thickness varying from 1.5 to 5 cm. Power for the magnets is provided by an alternator and flywheel storing 2 GJ of kinetic energy and driven by a 4000 horse-power motor. 250 MV A can be extracted from the

FIG. 2. A schematic of the C-Mod tokamak showing the major components.

TABLE II. C-Mod engineering parameters.[19]

Parameter	Range	Units/definition
Vessel volume	4	m^3
Vessel toroidal and poloidal resistance	40, 10	$\mu\Omega$
Vessel L/R time	20–50	ms
Effective pumping speed (turbopumps)	500 (D$_2$)	l/s
Effective pumping speed (cryopump)	10 000 (D$_2$)	l/s
Ohmic heating power	1.0–2.7	MW
ICRF source power	8	MW
Lower hybrid source power	3	MW
Peak utility power	24	MW
Peak extracted alternator/flywheel power	250	MV A
Alternator/flywheel stored energy	2	GJ
Toroidal field magnet current	0.225	MA
Toroidal magnet turns	120	
Forces from toroidal field	110	MN

alternator during a pulse and is supplemented by 24 MV A from the local electrical utility. Twelve independent power convertors supply current to the machine's magnets. For the first 14 years of its operation, C-Mod plasma control was via a hybrid digital-analog controller provided through a collaboration with the CRRP-EPFL.[21] More recently, an all digital real-time control system was implemented using a conventional linux server and I/O cards on a CompactPCI bus.[22] Instrumentation and control is handled by $\approx$30 industrial programmable logic controllers with mimic screens in the control room.[23] Pulse coordination, data acquisition, data management, and automated analysis are provided through the MDSplus data system.[24] The client-server capabilities of MDSplus allowed C-Mod to demonstrate the first remote operation of a fusion experiment.[25]

B. Internal hardware

From the start, plasma facing components (PFCs) in C-Mod were built to withstand the very high heat fluxes and mechanical loads that were anticipated. The design featured a vertical target lower divertor and refractory metals on all surfaces that could come into contact with the plasma. The machine can also run with an upper x-point on a flat target divertor behind which is installed a toroidal cryopump with an effective pumping speed of 10 000 l/s for D_2. The choice of high-Z metals was controversial at the time as earlier experience with tungsten limiters on PLT (Princeton Large Torus)[26] convinced a generation of fusion scientists that these materials were not practical. However, the C-Mod team believed that graphite and carbon composites would not be acceptable materials in a reactor and that the fusion program needed data that could demonstrate the advantages and overcome the challenges of refractory metals. The 20 years of experience gained on C-Mod in the relevant operational space has been a critical element in decisions made for the ITER first wall design. The C-Mod wall was originally faced with 7000 tiles made of the molybdenum alloy TZM (99.5% Mo, 0.5% Ti, and 0.08% Zr) installed on backing plates made of INCONEL or stainless steel depending on the strength required.[27] The large number of relatively small tiles was required to limit the forces due to eddy currents induced in the vessel during disruptions. The metallurgy of the raw material was important for the ability of these tiles to survive the thermal and mechanical shocks that they were subjected to. A belt of tungsten tiles was installed in the highest heat flux areas for several run periods for evaluation of a possible ITER design and to allow measurements of material erosion and migration. Figure 3 is a recent image of the internal hardware, showing the divertor, inner wall tiles, RF launchers, and internal diagnostics. Because of the compact size of the device and port space further limited by the heavy build of the magnets, a large amount of hardware is mounted on the tokamak wall. Over time, the C-Mod team has learned how to design, fabricate, and install hardware that can be subject to significant heat loads and disruption forces.

For machine conditioning, the thick, low-resistance vacuum vessel precluded any possibility of pulsed "Taylor"

discharge cleaning, which had been the standard procedure on previous Alcator devices. Instead, C-Mod surfaces are prepared for operation via Electron Cyclotron Discharge Cleaning (ECDC) using a 2.5 kW klystron operating at 2.54 GHz.[28] The toroidal field is operated near 0.09 T and slowly swept so that the discharge intercepts all of the internal structures. After a period of baking, discharge cleaning and initial operations, the plasma facing surfaces are typically covered with a thin film of boron by running discharge cleaning with deuterated diborane (10% B_2D_6 in 90% He background). Approximately 100 nm is deposited weekly when operating.[29]

C. Impact of the machine design for the C-Mod physics program

While the nature of the C-Mod device allows operation in a wide parameter space, it also drove a research program that was required to address and solve a set of critical scientific and technological challenges imposed by its design. These are prototypical of next-generation devices like ITER or Demo so that research on C-Mod, which was required operationally, is directly and uniquely relevant to meeting future challenges. The necessity of addressing these issues has focused effort on areas that many other research groups could ignore or defer. Among these challenges were

- Discharge startup with a highly conductive vacuum vessel: The vacuum vessel provides structural support for many of the poloidal field coils and thus was heavily built (1.5–5 cm thick) and with no electrical break. The toroidal resistance of the vessel is 40 $\mu\Omega$, and its L/R time is 20 ms. The TF support structure, while farther from the coils, has even lower resistance. The result is that at startup, up to 0.5 MA flows in each of these two structures presenting complications for diagnosis and control.[13]
- Very high power outflow: In a compact high-field device running at high absolute pressure, high performance necessarily implies high absolute power and particle loads to the first wall. C-Mod was constructed from the beginning with a divertor design and first wall material that would withstand these loads (by contrast, low-field devices tend
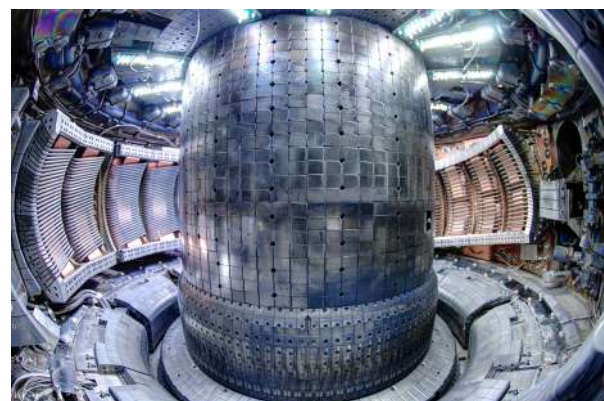

FIG. 3. Photo taken inside C-Mod, showing internal components including the divertor and inner wall limiter tiles as well as ICRF antennas and numerous diagnostics.

to run into β limits at high power well before they attain reactor-like heat fluxes).

- High-Z metal plasma facing components: The choice of refractory metals meant that solutions to contamination by high-Z impurities needed to be found and required research into the sources and transport of these impurities.
- Very high input power densities: To attain high-performance regimes, launchers for ion cyclotron range of frequency (ICRF) heating and lower hybrid (LH) current drive needed to operate routinely and reliably at high power densities ($\sim 10\,MW/m^2$).
- High efficiency, off-axis current drive at higher densities than previously achieved.
- High plasma performance without $T_i > T_e$, momentum input or core particle sources: The heavy magnet build precludes tangential port space sufficient for high-power neutral beams, thus all auxiliary heating on C-Mod is from RF, which does not directly supply particles or torque to the plasma core and mainly heats electrons. In contrast, on other devices, beams produce high external torque, core fueling, and ion heating, which are all correlated with good confinement.

III. DIVERTOR AND BOUNDARY PLASMA STUDIES

A. Overview of divertor experiments

A fitting preface to a discussion of boundary experiments on C-Mod is a 1983 quote from Peter Stangeby of the University of Toronto "*Right now everyone is worried about getting and keeping heat in. Eventually the main problem will be how to handle the heat coming out.*" From its inception, the C-Mod team understood that handling power exhaust would be one of its most significant challenges. The operating space for C-Mod is uniquely relevant and reactor prototypical in the following sense. The plasma in contact with material walls is subject to physics scaled to the energy of atomic bonds. Strong interactions with neutrals and impurities through ionization, recombination, and other atomic processes are critical elements for transport of heat, mass, and momentum in this region. Perhaps most importantly, erosion, caused by sputtering processes, drives a requirement to limit ion impact energies below a material-dependent threshold related to the bonding energy in the substrate. These arguments tell us that a reactor must operate with the plasma that is in contact with the wall at a fixed, low temperature. With that temperature at the ~ 2–$10\,eV$ required, the operating density is given by the plasma pressure and only C-Mod operates at reactor-relevant plasma pressures. Thus, the C-Mod experiments are carried out with the power and particle fluxes, plasma density, neutral density, neutral-neutral collisionality, neutral opacity, and photon opacity similar to what is expected in a reactor. These experiments are not "wind tunnels" with appropriately scaled parameters but are rather discharges with the actual reactor-like values. Experimental results under these conditions are particularly critical as the edge plasma and plasma-material interactions remain far beyond our modeling capabilities. The main difference between C-Mod and a reactor in this

region is in the length of the discharges. C-Mod cannot adequately address the set of issues related to machine lifetime and that show themselves only over millions of seconds.

All modern tokamaks are constructed with a toroidal divertor, designed to isolate plasma-wall interactions and to spread heat loads over as broad an area as practical. C-Mod innovated the vertical target divertor, as shown in Fig. 4. The key features of this configuration are a shallow angle between the magnetic field (0.5–1.5°, depending on the plasma equilibrium) and an extended divertor leg.[30,31] In this geometry, neutrals arising from recombination at the divertor strike point are directed toward the divertor channel, enhancing reionization and providing a natural baffling. Neutrals created in the divertor are isolated from the main chamber by the divertor plasma itself. One result is better isolation between the divertor and main plasma, leading to a lower density threshold for divertor detachment as discussed below in Sec. III C. The advantages of the vertical target divertor are now widely recognized, and the concept has been adopted for ITER.

B. Experience with a high-Z metal first wall

Also pioneered by C-Mod and adopted by ITER is the use of high-Z metals as a divertor material. C-Mod research has highlighted the advantages and the challenges of these materials and ultimately demonstrated their practicality. Any divertor material needs to withstand steady-state heat loads and to survive transient loads, which cannot be completely eliminated. In a reactor, operating with high availability for extended periods of time, two additional requirements become critical. First, the net erosion rate must be held below 1 sputtered atom for every 10^6 incident plasma ions.[32,33] Second, for safety and limits in supply, the retention of tritium fuel must be kept very low—less than 1 atom
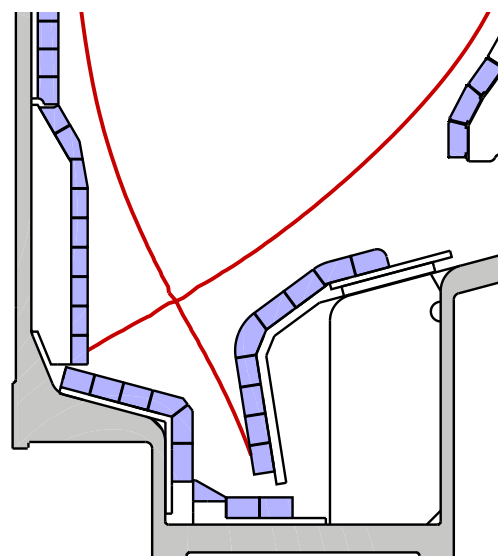

FIG. 4. The C-Mod vertical target divertor features a small incident angle between the magnetic field and the wall, a long divertor leg and natural baffling of neutrals. The separatrix for a typical MHD equilibrium is plotted in red.

of tritium fuel can be retained in the wall for every 10^7 plasma ions incident.[34,35] These requirements effectively rule out low Z materials like carbon even when they can withstand the heat loads. Graphite or carbon composites are a popular choice in current experiments because when introduced as an impurity into the plasma, the power loss from radiation is usually tolerable. High temperature plasmas consisting almost entirely of carbon ions, though useless for fusion, can be sustained. In contrast, the concentration of high-Z impurities must be strictly reduced—for example, concentrations of tungsten in ITER will need to be kept below 2×10^{-5}.[36] Because refractory metals offered the promise to control erosion and fuel retention, but presented a severe challenge for impurity control, the C-Mod team felt that this was the correct choice—the fusion program would eventually have to step up to this challenge and C-Mod seemed like an ideal platform to begin that research.

Experiments on C-Mod have addressed a large set of operational issues presented by the metal walls. These find no "show stoppers" that would rule out high-Z materials, but do reaffirm previous concerns about impurity sources and point out the need for additional research, particularly at the higher wall temperatures that will be typical of a fusion reactor. Plasma startup is not problematic with metal walls even after disruptions or other deconditioning events. This contrasts to the situation with carbon walls where some form of wall conditioning is typically required to reestablish operations.[37] Density control and fueling with metal walls are also straightforward, and recycling is generally high, certainly well above 90% in equilibrium, with the walls adjusting to significant changes in a few shots, i.e., a few seconds of discharge time. In the L-mode, the discharges can be readily gas fueled up to the density limit at currents up to 1 MA ($\bar{n}_e = 6.5 \times 10^{20}$/m^3). Access to the H-mode is comparably easy, compared to carbon machines—for example, at low q_{95}, Ohmic H-modes are regularly attained.[38] The density in the H-modes, normalized to the density limit, is typically 0.5–0.7, a bit below that seen in lower field, neutral beam heated devices. One reason for this is that the very strong gas puffing required for higher densities interferes with ICRF antenna operation,[39] though the lack of beam fueling may also be a factor[40] along with limitations of fueling and transport through a high-opacity edge and pedestal.[41] (The new field-aligned (FA) antenna described in Sec. VI has shown better behavior at very high neutral densities.) Since fusion plasmas have much lower tolerance for high-Z impurities, control of the sources from the wall is critical, especially during ICRF. The first experiments with high power ICRF and bare molybdenum walls found sharply increased molybdenum content, increased core radiation, and difficulty in achieving the high quality H-modes.[17,42] It was not clear what parts of the vessel were the principal sources of these impurities. Boronization, as described above, was employed and had the effect of sharply reducing radiation from molybdenum[43] and allowing the production of the high quality H-modes.[17] Research on impurity challenges in ICRF heated plasmas is described in greater detail in Sec. VI. Operational issues with tungsten plasma facing components are now also under intensive study by the AUG and JET devices.[44]

To keep the surface temperature of divertor plates within acceptable limits in a reactor, finite heat conduction dictates that no more than a few mm of material can intervene in front of the cooling channels. Thus, net erosion must be kept on the order of 1 mm over the lifetime of the first wall. One of the key advantages of refractory metals is their potential for lower levels of sputtering when exposed to ions (including impurities) accelerated through the plasma sheath. The energy threshold for sputtering from refractory metals is much higher than for low-Z materials like carbon or beryllium, with exponentially smaller sputtering yields if the edge plasma electron temperature can be held at sufficiently low values. Erosion rates for molybdenum were first determined on C-Mod by analysis of divertor tiles removed between experimental campaigns and measuring the change in depth of a thin chromium marker layer using Rutherford backscattering.[45] Net erosion was highest near the outer divertor strike-point, reaching 150 nm for the 1200 s of discharge time during the campaign, equivalent to removal of 4.5 mm/discharge-year. Gross erosion rates were estimated from physical sputtering yields using measured plasma conditions and were somewhat higher than the measured net erosion—partly attributed to prompt redeposition of sputtered ions. Installation of a toroidally continuous row of bulk tungsten tiles enabled measurement of erosion and migration onto other plasma facing components.[46] In this case, the surfaces were analyzed after removal by measuring x-ray emission stimulated by exposure to a 2 MeV proton beam. Analysis of the x-ray spectra allowed determination of the quantity of tungsten on otherwise molybdenum substrates. Figure 5 shows the pattern of deposition found at different poloidal locations. The pattern suggests that scrape-off layer (SOL) flows play an important role in movement of sputtered materials to distant locations. Integration of migrated material yields an estimate for tungsten erosion of 0.014 nm/s or less
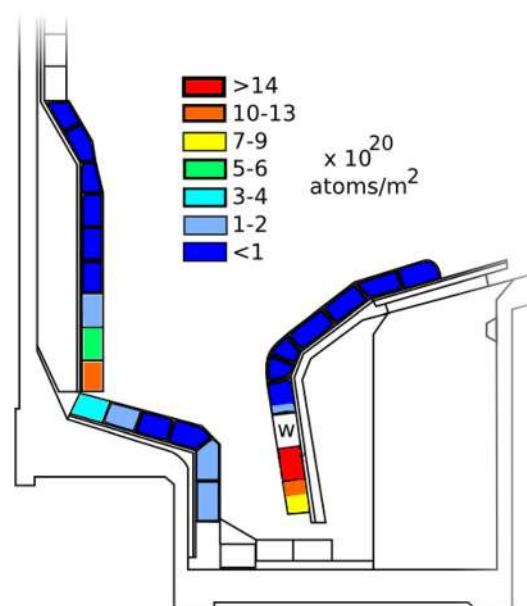

FIG. 5. Tungsten redeposition thickness in nm, from a toroidal belt of tiles on the outer divertor (marked "W"). The material deposited can be integrated to estimate the average erosion rate. Reprinted with permission from Barnard *et al.*, J. Nucl. Mater. **415**, S301 (2011). Copyright 2011 Elsevier.[46]

than a mm per discharge-year—though we must note that the plasma strike-point was not in contact with the row of tungsten divertor tiles at all times during the experiments carried out in this campaign. The values for measured molybdenum and tungsten erosion were, respectively, 10–100 times lower than what has been found for graphite.[47] Gross erosion may be a more important measure of acceptable plasma-wall interaction since changes in surface morphology and chemistry associated with redeposition may lead to unacceptable changes in physical properties like thermal conduction. Gross erosion may also increase the amount of dust—a safety issue in a reactor—or allow the build-up of poorly bonded flakes, which would subsequently enter the plasma and cause harmful disruptions.

The retention of tritium fuel within the first wall materials is another critical plasma-wall issue for ITER and for future reactors where safety considerations limit tritium inventory to about 1 kg. Using the expected plasma parameters, we find the acceptable limit is less than 1 tritium ion retained for every 10^7 incident on the plasma wall. A similar number is obtained from economic considerations, given the modest tritium breeding ratios that are expected. The requirement for low fuel retention also drives the interest in high-Z metal walls, since the solubility and reactivity of hydrogen in such metals is much lower than for carbon. Experiments on C-Mod measured retention of D_2 gas over a single discharge by "static gas balance," that is, by looking at the equilibrium pressure attained after running a plasma discharge with all torus pumps valved off compared to a case with the same gas puffing but without a plasma.[48] In these experiments, roughly 1% of the incident deuterium ion fluence is retained with no indication that the retention rate is decreasing after 25 s of integrated plasma exposure. The magnitude of retention is significantly larger than what is expected from extrapolation of laboratory results.[49] The interpretation of the result is that "traps" are created in the molybdenum substrate by the high incident particle flux.[49] The traps are defects in the molecular structure that can hold deuterium atoms, which are otherwise insoluble in the unperturbed matrix. In contrast to single shots, the campaign-integrated retention is about $1000\times$ lower. The difference is apparently due to the occasional disruption, which removes deuterium through transient heating of the tile surfaces. These results point out the importance of conducting experiments at reactor-relevant temperatures, which is with the wall at about 1000 K, where defects in the wall molecular structure are expected to be annealed and retention would be dramatically reduced.

An example of material changes that can be induced by plasma interactions is the growth of tungsten nano-structures ("fuzz") that has been observed in plasma-wall test stands under suitable conditions.[50] The working hypothesis for their formation is that the structures, which consist of small filaments, are extruded by pressure from helium bubbles captured in the metal substrate. An open question was whether the same phenomena would occur on the wall of a confinement experiment or if other plasma-wall processes would destroy the structures before they could grow to significant size. On C-Mod, a careful experiment was performed to raise a tungsten sample to the correct surface temperature, about 2000 K, and expose it to helium plasmas for a sufficient time to match the fluxes and fluences employed on the test stand. Nano-structures, shown in Fig. 6, were created with nearly identical morphology and growth rates (tendril diameter $\sim$100 nm and growth rate $\sim$600 nm in 13 s of exposure at temperature).[51,52] Helium concentrations in the fuzz layers were measured at 1%–4%, which is well above natural solubility of helium in tungsten, but below the values expected for pressure-driven growth. Erosion rates from sputtering of the tungsten sample were well below the fuzz growth rate; however nearby, molybdenum surfaces operating at lower temperatures were predicted to have faster sputtering than growth. As expected, these surfaces did not show evidence of surface nano-structures. Overall, we conclude that the tokamak environment has little or no impact on tungsten fuzz growth when compared to linear plasma devices. This provides confidence that key growth parameters identified in linear devices can be used to predict surface behavior in future devices. None-the-less, a number of critical questions must still be answered. Largely unknown are the effects of the fuzz on tokamak operations, including wall recycling, fuel retention, erosion, and dust production. Research is also required to clarify the effects on fuzz growth of large Edge Localized Modes (ELMs), impurity seeding, and mixed wall materials.

Post-campaign *ex-situ* measurements usually represent inadequately defined averages over discharge conditions from an entire campaign rather than carefully controlled conditions. A measurement from a single point in time is typically all that is available for an inherently dynamic and complicated process, and the progress is correspondingly difficult and slow. To overcome these limitations, a new diagnostic has been developed and deployed on C-Mod, which is capable of time resolved, *in-situ* measurements of surface erosion and fuel retention. This diagnostic, AIMS (Accelerator Based *in-situ* Materials Surveillance), employs a 1 MeV D+ beam that is injected into the torus between shots and steered by the magnetic field produced by running small currents in the TF and PF coils.[53] A large selection of
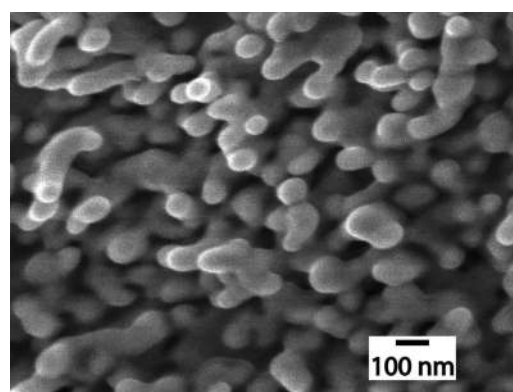

FIG. 6. A micrograph of tungsten nanostructures produced by 13 s of helium discharge time on a target operating at about 2000 K. The morphology and growth rate are essentially identical to what is produced in a linear plasma device under similar conditions. Reprinted with permission from Wright *et al.*, Nuclear Fusion **52**, 042003 (2012). Copyright 2012 IOP.[51]

TABLE III. A few of the nuclear reactions that can be employed by the AIMS diagnostic.

Probe ion	Target	Detected particle	Surface measurement
D^+	D	n	Fuel retention
D^+	Li^6, Be^9, B^{11}	γ	Erosion of surface coating
D^+	C^{12}, N^{14}, O^{16}	γ	Surface impurities

wall locations can be accessed by this method and tested between plasma discharges. The beam induces nuclear reactions that allow characterization of the surface composition. Some of the possible reactions and their application to surface analysis are listed in Table III. By preparing tiles with coupons of selected materials, the scope of possible measurements can be further increased, for example, to measure the erosion of high-Z plasma-facing components. A drawing of the AIMS system is shown in Fig. 7.[54] Early results have proven the principle of the technique and shown that measurements could be routinely made between shots.[55–57]

C. Divertor regimes and detachment physics

Meeting the challenges of divertor power handling and erosion require better understanding of the underlying physics, through which improved designs and operating regimes can be achieved. The operating point of the divertor depends in large measure on the balance between parallel and perpendicular transport. Three regimes of parallel transport were identified in C-Mod experiments and are illustrated in Fig. 8, which compares electron pressure and temperature at the midplane to the corresponding profiles measured at the divertor target.[58,59] The midplane profiles are measured with fast-scanning Langmuir probes and the divertor profiles with fixed probes that are imbedded in the tiles. At the lowest densities, when the parallel electron mean free path is long compared to the connection length ($\sim qR$), electron temperature and pressure are constant along the field lines. The divertor sheath supports the entire temperature drop from the midplane to the tile surface. In this "sheath limited" regime, the
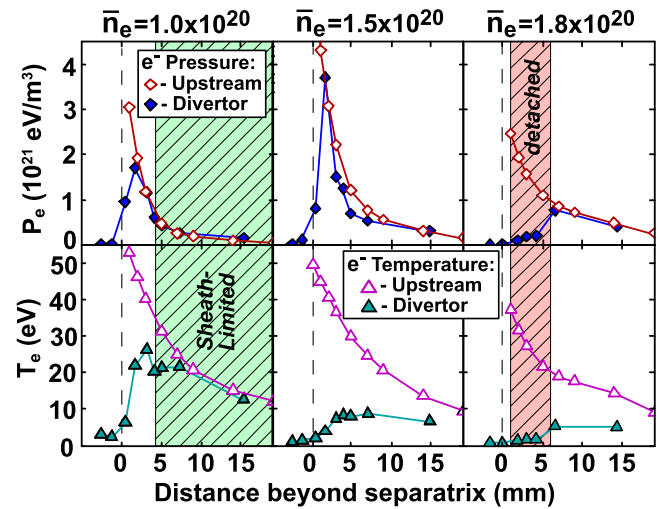

FIG. 8. Three divertor regimes that are produced at increasing density, are identified in this plot of pressure and temperature profiles in the SOL. Reproduced with permission from Phys. Plasmas **2**, 2242 (1995). Copyright 1995 AIP Publishing LLC.[58]

divertor temperature is too high and would lead to unacceptable divertor erosion rates for a reactor. At moderate densities, collisions reduce the parallel thermal conduction and produce a parallel temperature gradient. This results in lower temperatures at the target, about 10 eV, and correspondingly lower erosion rates. The pressure along the field lines is still constant so the density increases near the divertor and supports the required power conduction. At higher densities still the plasma interacts more strongly with neutrals (which increase nonlinearly with plasma density), transferring plasma momentum and energy to them. The momentum transfer causes the plasma pressure to drop, and energy transfer lowers the temperature to the point where volumetric recombination occurs, further reducing the plasma pressure. In this "detached" stage, the temperature at the target drops to about 2 eV and the heat is largely removed from the plasma by radiation and charge exchange, spreading the heat
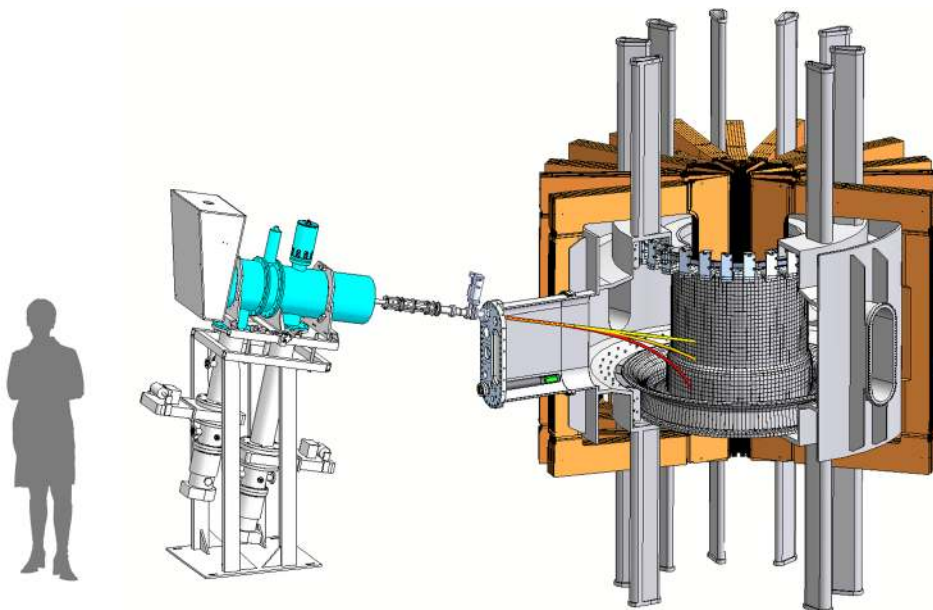

FIG. 7. The AIMS diagnostic makes the first time-resolved, in-situ measurements of plasma-wall interactions. It utilizes a 1 MeV deuterium beam, which can be steered between shots by magnetic fields and induce nuclear reactions in the materials of the first wall. Reproduced with permission from Rev. Sci. Instrum. **84**, 123503 (2013). Copyright 2013 AIP Publishing LLC.[54]

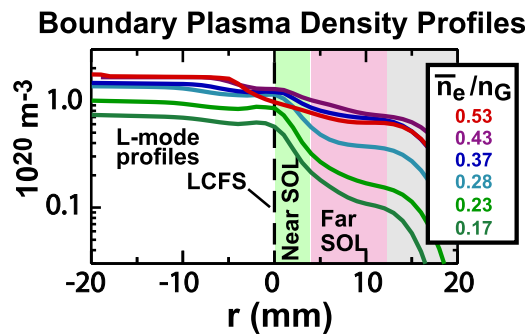## Boundary Plasma Density Profiles

FIG. 9. Typical SOL density profile as a function of global normalized density. Reproduced with permission from Phys. Plasmas **15**, 056106 (2008). Copyright 2008 AIP Publishing LLC.[91]

load over a much larger area. From the point of view of erosion and divertor survival, it is highly desirable to operate the divertor in the detached state.[34]

The border between the three regimes can be characterized as fractions of the density limit, with the boundaries shifting to higher densities with increased input power. The density and power dependences are partly attributed to the increase in collisionality, consistent with the observations of anomalous cross-field transport discussed in Sec. III E. In typical SOL profiles, such as those shown in Figs. 8 and 9, detachment starts near the strikepoint first and grows outward as the density is raised. Experiments were carried out to explore the role of divertor geometry in the detachment phenomena, comparing the standard vertical target configuration to a flat plate and slot divertor by moving the strike point across the divertor surfaces. Detachment occurred with the vertical target at about half the density of the flat plate with a slight further improvement for the slot divertor.[60] These experiments suggest that the main effect is an increase in the interaction between recycled neutrals and the divertor leg for the vertical target. The increase in divertor leg length is apparently a secondary effect. It is worth noting that detachment in C-Mod occurs well below the density limit for all three cases.

With the high plasma pressures that were accessible, C-Mod discovered the importance of volume recombination, neutral collisionality, and Lyman α photon opacity on divertor behavior. Modeling of the ITER divertor has confirmed the importance of these parameters.[61] At the low temperatures and high densities seen in the detached regime, the plasma can begin to recombine volumetrically, a process that otherwise occurs only on surfaces as recycling. Recombination was confirmed by the distribution of line intensities in the Balmer spectrum, which is markedly

different in ionizing and recombining plasmas.[62,63] Extensive modeling of the spectra and atomic physics allowed determination of the recombination rate and of the plasma parameters in those regions. Under the conditions that prevailed, the plasma became opaque to Ly$_\alpha$ photons,[63] with the photon mean free path dropping to about 1 mm, modifying the recombination rate. Also affected by the operation at high densities is the transport of neutrals, with the mean free path for neutrals in C-Mod closer to what is expected in ITER than in any other device. Studies carried out to explore the dynamics and distribution of neutrals showed they are trapped in the divertor by the plasma, providing a natural baffling and building up the neutral pressure in the divertor chamber to levels exceeding 100 mT in some cases.[64,65] Recycling impurity gases are preferentially compressed and enriched in the divertor region.[66,67] Detachment can be enhanced by injection of impurities, which radiate inside the separatrix and in the divertor, reducing parallel heat exhaust. This effect can be exploited to reduce the divertor heat load, but care must be taken to avoid degrading core performance. The detachment front can be unstable along the field line and move to the x-point where the colder plasma can reduce the H-mode pedestal. Modeling of the divertor region was carried out with the impact of each of these factors assessed.[68,69] Even with all of the known effects included, there were important experimental features that could not be modeled. The crucial missing physics may be the spatially dependent, nonlinear cross-field transport that is the subject of Sec. III E.

D. Divertor heat load

The heat load on the divertor is determined by the physics of the boundary plasma and the geometry of the magnetic field and first wall. While the process is simple to define, critical gaps in our understanding prevent reliable prediction and extrapolation to ITER and to future fusion reactors. C-Mod has carried out important research to help fill these gaps and to make direct measurements of the heat footprint under reactor-like conditions. The measurement of the heat load footprint is challenging on C-Mod for reasons very similar to those facing ITER. It is intrinsically hard to get a good view of the vertical target with an infra-red camera due to its geometry and the highly reflective metal walls have low emissivity. Moreover, the surface emissivity is not constant over time since changes in coatings or surface conditions are routine in the high heat-flux areas under study. To meet these challenges, an innovative set of diagnostics was deployed, summarized in Table IV and shown in

TABLE IV. Heat-flux footprint diagnostics.

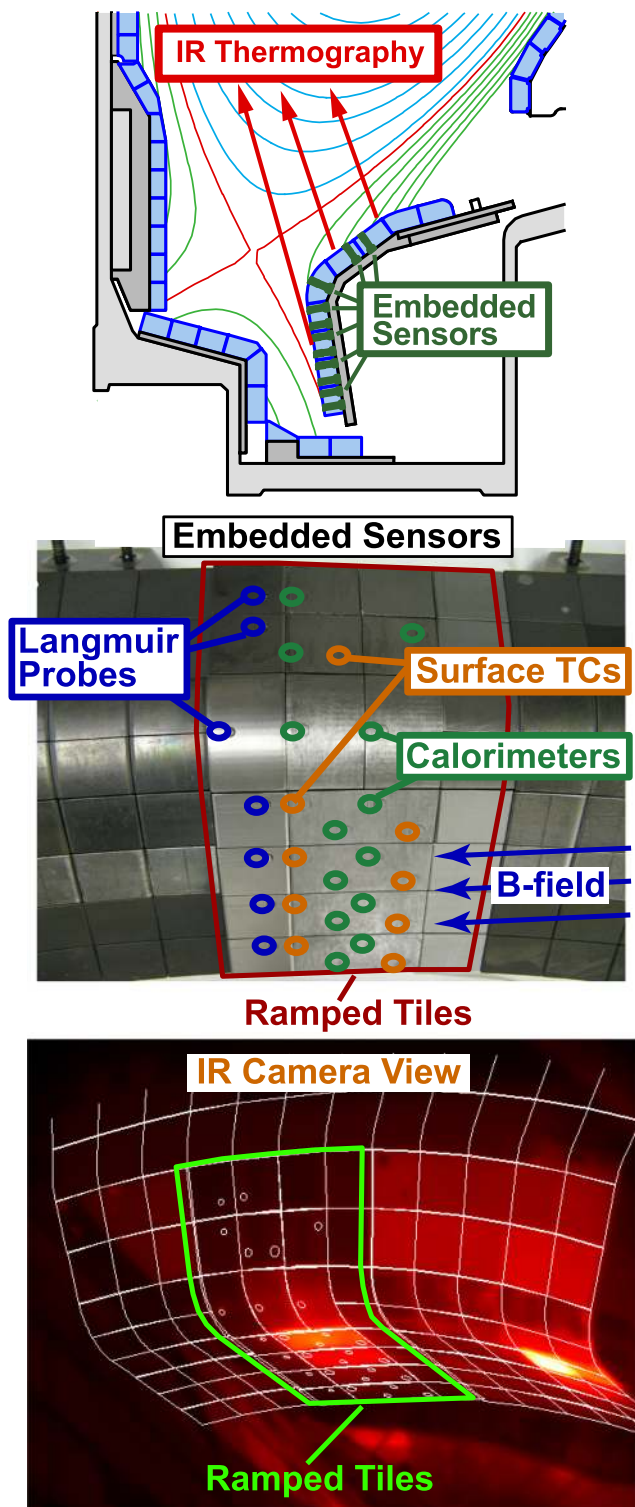| Diagnostic	Measurement	Analysis/calibration scheme	References
Langmuir probes	Plasma T_e, n_e	Hat flux compared to surface thermocouples through sheath theory	73 and 74
Retarding field analyzer	Plasma T_i	Compared to CXRS B^{5+} ion temperature	76 and 77
Surface thermocouples	Instantaneous surface temperature and heat flux	Integrated and compared to calorimeters	74
Calorimeters	Bulk temperature and integrated heat flux	Ice-point compensated	73
IR camera	Instantaneous surface temperature	Emissivity calibrated by comparison with thermocouples imbedded in viewed tiles	70

Parallel Heat Flux Density

Full-width, half-max: 1.8 mm

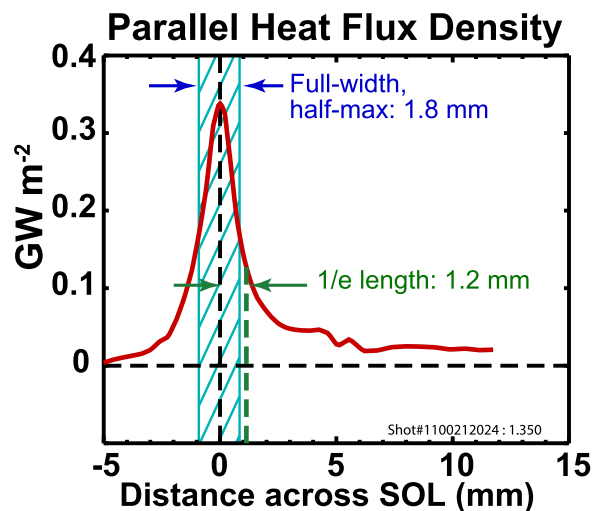1/e length: 1.2 mm

Shot#1100212024 : 1.350

FIG. 11. The heat flux profile measured with the infra-red camera and calibrated against probes and thermocouples. These profiles show the narrowest width and highest power flux measured on any magnetic confinement experiment. Reproduced with permission from Phys. Plasmas **18**, 056104 (2011). Copyright 2011 AIP Publishing LLC.[72]

FIG. 10. Divertor heat flux diagnostics. Reproduced with permission from Phys. Plasmas **18**, 056104 (2011). Copyright 2011 AIP Publishing LLC.[72]

Fig. 10.[70–74] The diagnostics targeted a region of the outer divertor that was modified to provide a slight radial ramp, ensuring that no tile-to-tile shadowing interfered with accurate measurements. Physics-based calibration strategies allowed redundant cross-comparisons adding to confidence in the results. A measure of success is that the overall energy accounting for each shot—power into the plasma vs power

deposited on divertor and limiter surfaces—was balanced within 10% for discharges produced over the 3 years of experiments for which the diagnostics were in place.[75]

A typical measurement of the heat footprint, mapped to the plasma midplane, is shown in Fig. 11,[78] which features the highest peak power and narrowest width of any existing device. Surface temperatures regularly exceed 1300 K. The resulting data from C-Mod challenged empirical scalings that existed at the time.[79,80] Contrary to the earlier work, C-Mod found that the dominant scaling was $1/I_P$ (or $1/B_P$) with no dependence on B_T, q_{95}, the connection length or on conducted power.[72] Overall, the SOL power density profile at the divertor plate mapped to the pressure profile at the midplane, suggesting that critical gradient physics was responsible for setting the former quantity as well. The heat flux footprint was tied to pedestal conditions, consistent with the picture of the near-SOL and pedestal as a single integrated system. In the L-mode and a variety of H-mode regimes, higher pedestal pressures are associated with narrower heat-flux footprints. The higher pressure pedestals are also associated with better global energy confinement[17] reinforcing the inherent challenge of achieving good core performance simultaneous with an acceptable divertor solution. C-Mod heat footprint data contributed to an international database, extending the range in B_T, B_P, plasma pressure, and heat flux to ITER-like values in multi-machine empirical scaling studies.[81] The unique diagnostic set on C-Mod also allowed an accurate determination of the sheath transmission factor that relates plasma properties upstream of the sheath to the heat flux conducted to the underlying material. Theoretical calculations predict a value for this factor ≈ 7, but experimental measurements of this critical quantity have ranged from 2 to 20 (with the values below 5, physically impossible). Using the measurements from the calibrated surface thermocouples and accounting for the non-zero current flowing through the sheath, a good agreement with theoretical models was found, leading to an excellent match
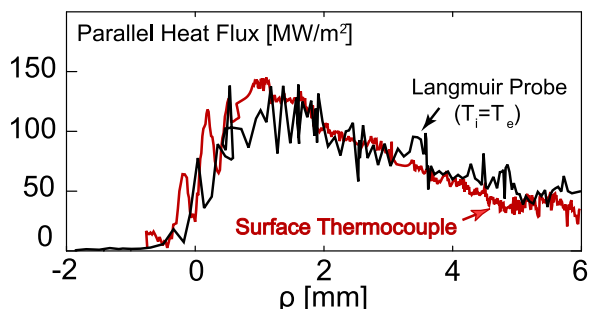
FIG. 12. Heat flux profiles calculated based on plasma measurements compare well to the values taken directly from surface diagnostics. Reproduced with permission from Rev. Sci. Instrum. **83**, 033501 (2012). Copyright 2012 AIP Publishing LLC.[74]

between the measured heat flux profile and the value calculated from probe measurements of the local plasma temperature and density (see Fig. 12).[74]

Measurement of the divertor heat flux is only half the battle. Given the narrow deposition footprints that are currently predicted for ITER,[81] methods to reduce the power load to acceptable engineering limits must be found. One solution is to inject a small level of recycling impurities that would radiate near the plasma edge and spread the heat over a larger surface area. The challenge is to effect this change without greatly reducing the heat flux across the separatrix and thus lowering the pedestal height and the overall plasma performance. Experiments were carried out to find the right types and quantities of impurity gas.[82] C-Mod was the first to demonstrate good core performance with Demo-like values of radiated power fraction. Using neon and nitrogen gases, these experiments were able to achieve H_{98} of 1 with conducted power to the divertor normalized to the loss power ($P_{LOSS} = P_{IN}$-dWdt) as low as 10% as seen in Fig. 13.[83,84] Interestingly, the impurity seeding also improved ICRF coupling.[85] That effect is not understood but believed to be caused by changes in the edge plasma profiles or fluctuations.
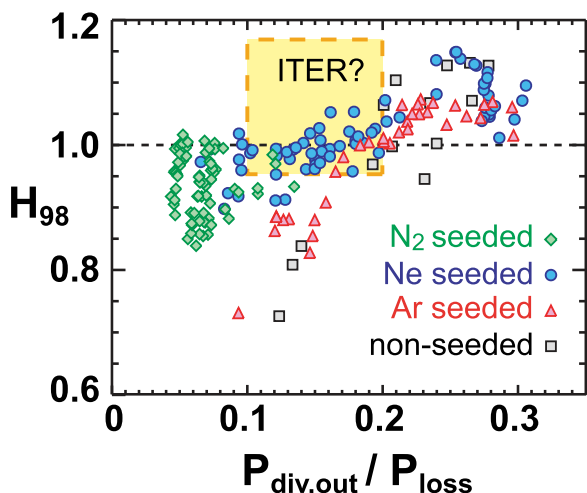
E. Cross-field transport and flows in boundary

C-Mod data have contributed to a new view of the nature and importance of cross-field transport in the tokamak boundary. Previously, transport in this region of the plasma had been assumed to be Bohm-like and poloidally symmetric (and often chosen arbitrarily as a free parameter to be adjusted to match models). Observations on C-Mod overturned this view, showing distinctly un-Bohm-like behavior, with no dependence on B_T and a strong dependence on collisionality[86]—particle diffusivity is roughly proportional to ν^{*2} with profiles held near a critical gradient as explained by marginal stability arguments.[87,88] Figure 14 shows a set of SOL profiles for the normalized pressure gradient α_{MHD}, which is proportional to the β_P gradient. This characterization of the profiles allows them to be overlain for a wide range in operational parameters. The shape of these critical α_{MHD} profiles is consistent with a dependence on collisionality predicted by several theoretical treatments.[89,90] Fig. 15 shows the increase of the normalized pressure gradient with normalized inverse collisionality in the regime of high collisionality[88] and can be compared directly, for example, to Fig. 1 from Ref. 90. The models predict a very sharp increase in turbulence and transport when the gradient exceeds some nominal threshold, thus enforcing the marginal stability condition.

Turbulence and transport delineate two distinct regions of the boundary plasma. Typical profiles can be seen in Fig. 9.[91] In the near-SOL, typically a few mm in C-Mod, the plasma gradients are steep and apparently determined by

FIG. 13. Normalized H-mode confinement, H98 is plotted vs Pdiv/Ploss, the power conducted to the divertor normalized to the net input power. By puffing small amounts of impurities, radiation losses can be increased without degrading confinement—meeting ITER operational requirements. Reprinted with permission from Hughes *et al.*, Nuclear Fusion **51**, 083007 (2011). Copyright 2011 IOP.[83]
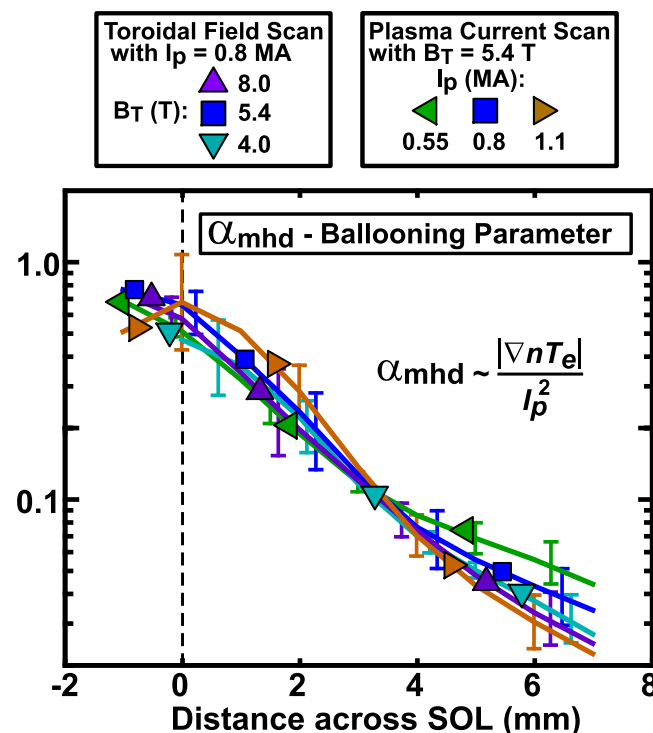

FIG. 14. Plasma profiles in the SOL overlay if they are parameterized by the α_{MHD} parameter (essentially the gradient in β_P) supporting the hypothesis that the profiles are set by cross field transport at marginal stability. Reproduced with permission from Phys. Plasmas **18**, 056104 (2011). Copyright 2011 AIP Publishing LLC.[72]
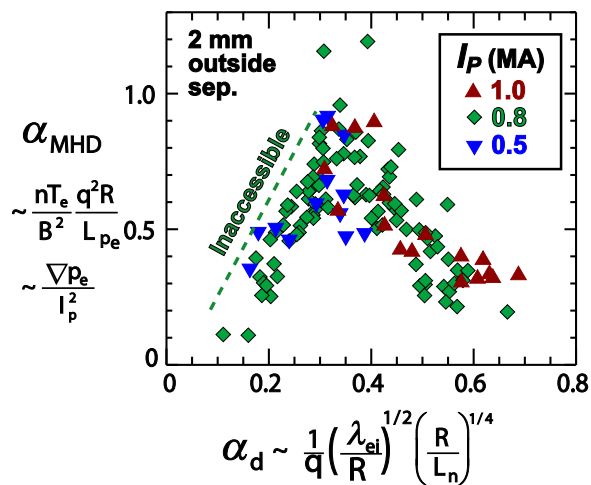
FIG. 15. The normalized pressure gradient (α_{MHD}) in the near-SOL depends on strongly on collisionality.[88] Reprinted with permission from LaBombard *et al.*, Nuclear Fusion **45**, 1658 (2005). Copyright 2005 IOP. α_d is the inverse normalized collisionality as defined in Ref. 90.

local marginal stability conditions as described above. Fluctuation statistics in this region are "normal," that is, with symmetric, Gaussian probability distributions.[87] Contrary to earlier expectations, the sharp gradients in the near-SOL profile shapes do not continue indefinitely (or until the plasma encounters a material object). Instead, after a relatively short radial distance, very large, isolated fluctuations are torn from the near-SOL and propagate radially due to un-cancelled particle drifts into the "far-SOL," creating a region of relatively weak gradients.[92] These highly intermittent fluctuations, seen in ultra-high-speed images, Fig. 16,[93,94] are often referred to as blobs because of their appearance in poloidal cross-section or as filaments because of their extended structures along the magnetic field lines.[95] They cannot be understood from local plasma instabilities in the far-SOL—the gradients are too flat—but can be understood as the byproduct of near-SOL turbulence. Under these conditions, the plasma near the wall is not a vacuum and interactions with physical structures are inevitable. That is, the transport that leads to the flat profiles does not allow isolation of the plasma-wall interactions to the divertor as previously
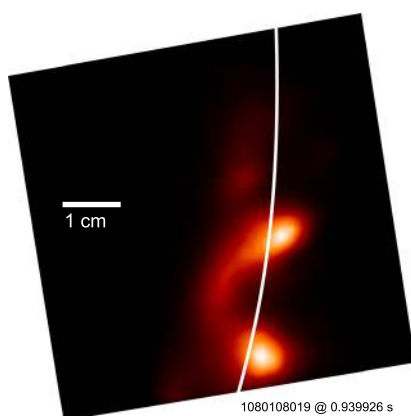
thought.[96] In particular, particle exhaust is not exclusively through the divertor leading to the phenomenon of "main chamber recycling," first recognized on C-Mod. Rather than resulting only from leakage out of the divertor, a significant neutral population is built up in the vessel outer midplane through the interaction of the far-SOL and the wall. This result was most clearly demonstrated by the installation of a novel "divertor bypass flap" system by which the divertor could be opened or closed during a C-Mod discharge.[97] With the divertor flaps open, neutral pressures in the divertor would decrease by a factor of two while midplane neutral pressured remained unchanged—that is, the pressure in the main chamber was set by its own dynamics not by leakage from the divertor.[98] These experiments also showed that divertor leakage had no effect on the L-H power thresholds or the H-mode confinement, contrary to prevailing ideas at the time. Blob dynamics have been compared to a variety of physical models, which can, at least partially, explain their propagation velocity.[99,100] A statistical model has been developed, using measurements from C-Mod, which accurately describe the observed probability distribution function over many decades by characterizing the process with just two numbers—the birth duration and the average waiting time between blobs.[101–103] These numbers provide a sensitive metric for testing numerical models of near-SOL turbulence, whose dynamics should produce the same statistical quantities.

1. The tokamak density limit as a consequence of edge turbulence

Observations in C-Mod of anomalous cross-field transport in the plasma boundary also provide a likely mechanism for the tokamak density limit,[5,104] which has an empirical scaling $n_G = I_P/\pi a^2$. There is a general agreement that the limit is associated with progressive cooling of the plasma edge, leading to a shrinkage of the current profile and MHD instability. Unlike the operational limits on safety factor or pressure, the density limit cannot be understood solely through MHD mechanisms, and despite its observation for more than 40 years, no definitive and self-consistent model for the limit has been developed. One class of models that was prevalent before the C-Mod results explains the edge cooling as a consequence, in one way or another, of impurity radiation. These models are based on the explicit dependence of radiated power on plasma density and typically the dependence of radiation cooling curves on temperature.[105,106] However, they fail to explain several important observations. First, the density limit does not depend on input power, nor on impurity content (at least for discharges with $Z_{EFF} < 2.5$), neither is the limit always associated with very high levels of radiated power. Second, while Marfes and divertor detachment can occur near the limit, often they are triggered harmlessly at substantially lower densities.[107] An alternate mechanism, tied instead to changes in plasma transport, was motivated by observed changes in particle confinement near the density limit, the nonlinear increase in gas fueling required as the normalized density, n/n_G, increased and the observation that the decrease in density during current ramp-

FIG. 16. The far-SOL plasma is composed of large amplitude structures (often called "blobs" or "filaments") that originate in the near-SOL and propagate poloidally and radially. This image is produced by the gas-puff imaging (GPI) diagnostic.
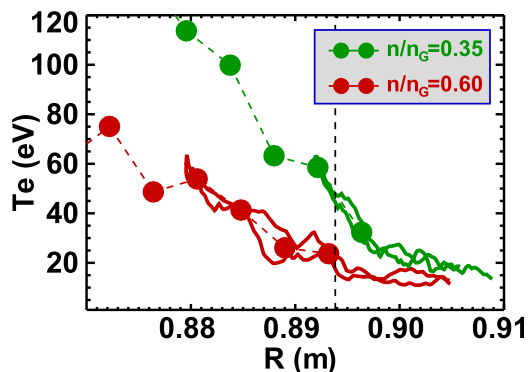
FIG. 17. Edge temperature profiles show the progressive edge cooling as the normalized density is increased toward n_G.

down at the end of a plasma shot is often at the rate required to stay just below the density limit.[5] That is, the discharge sheds particles during ramp-down to keep n/n_G just below 1.

C-Mod carried out experiments to measure the change in edge temperature along with any changes in fluctuations that accompany the approach to the density limit.[87,104] Well before the limit was reached, changes in the time-averaged SOL density profiles were observed, with progressive increases in the far-SOL density and overall flattening of the profiles even with modest increases in the separatrix density as shown in Fig. 9. At the same time, the amplitude, frequency, and velocity of blob production increased.[103,108] This picture is supported by fluid models, which predict very strong transport under these conditions.[90,109] At still higher densities, the boundary between the near-SOL and far-SOL moved inward, with the region of colder plasma, intermittent fluctuations and blob creation[110] eventually crossing the separatrix and intruding onto regions of closed field lines as

seen in Figs. 17 and 18. The net cooling mechanism is the exchange between warm plasma convected outward and cold fueling gas entering to replace it. When that boundary reaches roughly to the position of 0.85 normalized flux (a movement of about 3 cm on C-Mod), a density limit disruption is triggered. As the density limit is approached, perpendicular transport of energy is significantly increased and given the low upstream temperatures, the parallel energy transport channel is starved. This contrasts with the situation at lower density where all power is lost via the parallel channel to the divertor. In that case, the upstream temperature is pinned to a narrow range, typically to 60–100 eV, at the boundary between open and closed field lines. At densities close to the limit, perpendicular transport dominates on the open field lines and the temperatures can drop to much lower values. The appearance of Marfes or divertor detachment is then inevitable—if the plasma has not detached at lower densities, it will certainly detach near the limit where virtually no power is available in the parallel channel. While the observations coupled to the predictions of turbulence models make a compelling case for turbulence as the underlying cause of the density limit, work remains to develop a predictive model. What is required is a model that can calculate the change in the equilibrium temperature profile as the density is raised, which will require, at a minimum, a flux-driven solution to equations for turbulence and collisional plasma transport coupled to a neutral transport model.

2. Poloidally asymmetric transport and sonic SOL flows

An important prediction of turbulence models is that transport would have a significant ballooning structure, that is, the turbulence would be stronger on the low-field side (LFS) of the plasma, which has a bad curvature, compared to the high-field side (HFS) with its good curvature. This prediction was tested on C-Mod using an innovative fast-scanning probe, mounted on the inner wall and driven by the tokamak's strong toroidal field crossed with currents in a small coil in the probe mechanism.[97,111] (The design is all the more remarkable in requiring that the probe be normally
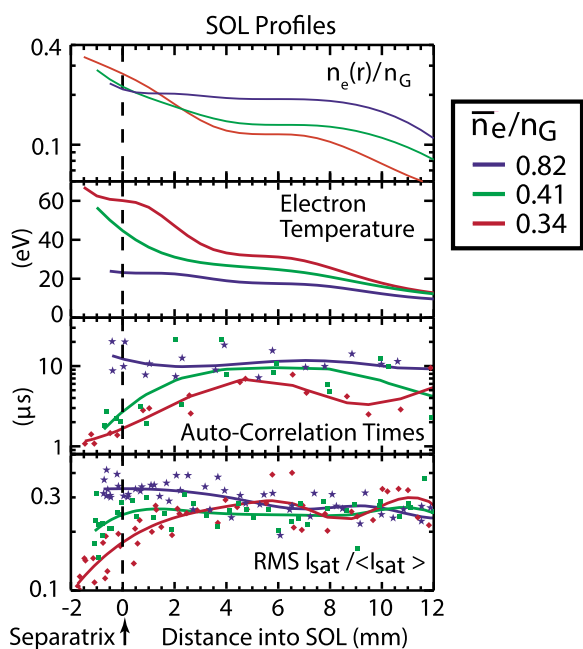

FIG. 18. Probe measurements show the increase in turbulence amplitude and intermittency that occurs as the normalized density n_e/n_G is raised. Reproduced with permission from Phys. Plasmas **8**, 2107 (2001). Copyright 2001 AIP Publishing LLC.[87]
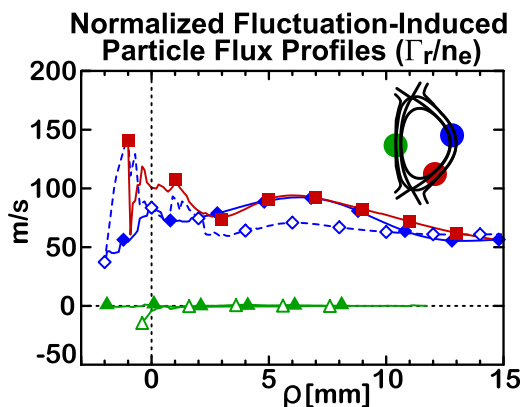

FIG. 19. Normalized turbulent flux profiles from the low- and high-field side of the discharge are compared. There is essentially no turbulent transport on the high-field side of the tokamak, consistent with an important curvature drive for the underlying instabilities. Smick *et al.*, Nuclear Fusion **53**, 023001 (2013). Copyright 2013 International Atomic Energy Agency.[114]

positioned in a protected location behind the inner-wall limiter, reducing space for the radial build for the entire mechanism to only 1 cm.) Fig. 19 shows the normalized fluctuation induced particle flux profiles from several poloidal locations.[112] The flux is computed using the measured potential and density fluctuations, accounting for their phase difference and cross-correlation. The result is clear; there is virtually no turbulent transport on the high-field side of the tokamak as expected for modes driven by pressure and curvature. This is confirmed by observations of the profiles, which for the case of carefully balanced double null plasmas find almost no plasma on the high field side.[113] For single null plasmas, this region is populated, but only through parallel flows of plasma lost on the low-field side, as shown in Fig. 20.[114] The resulting flows can be measured and are found to be near the sound speed as the plasma expands into a near vacuum.[113] The effects of these flows on the H-mode threshold are discussed in Sec. IV A.

3. Impact of cross-field transport on boundary physics

Experimental results from C-Mod have highlighted the centrality of turbulent transport to a wide range of boundary plasma phenomena. These results challenged the conventional view that anomalous cross-field transport was a secondary effect that could be represented in a simplified parametric form in plasmas that were understood mainly through the lens of collisional transport and atomic physics. Particle exhaust was found to have an important perpendicular component, wherein the plasma-wall interactions could not be isolated to the divertor. The dynamics and thresholds for divertor regimes were found to be sensitive functions of perpendicular transport, which not only competed with parallel processes but also determined the plasma-neutral
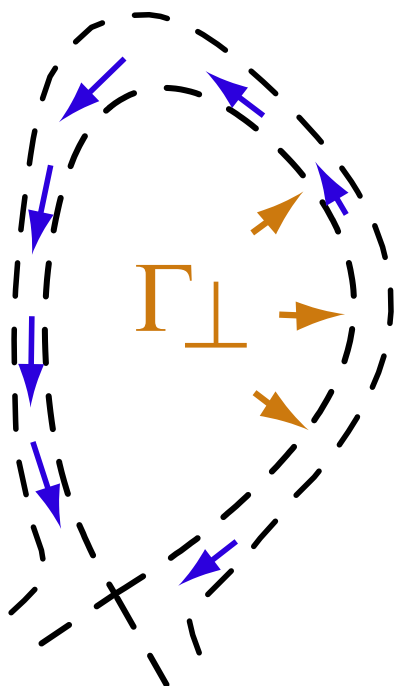

FIG. 20. Schematic showing how asymmetric transport drives sonic flows in the SOL.

interactions through the nonlinear increase in fueling required as the normalized density was increased. The same physics led to the tokamak density limit, which should be understood fundamentally as a transport phenomenon in which edge cooling is driven by collisionality-dependent turbulence. The poloidal asymmetry of turbulent transport, which is the result of curvature driven instabilities, causes sonic flows in the SOL. (We will see in Sec. IV that these are likely responsible for important variation in the L-H threshold as well.) The width of the heat-load footprint, at least in the attached state, can also be understood as a manifestation of turbulent transport since the pressure profile at the target maps to the transport-determined midplane pressure. Overall, the conclusion must be that any prediction of plasma boundary and plasma-wall prediction requires deeper understanding of cross-field transport.

IV. EDGE TRANSPORT BARRIER PHYSICS

The improvement in energy confinement provided by the H-modes is required for ITER baseline operations as well as most tokamak-based reactor designs. Edge transport barriers raise the temperature at the boundary of the plasma, increasing the core gradients through profile stiffness as described in Sec. V A. C-Mod has carried out research in all three key areas of edge barrier physics: access conditions for barrier formation; profile structures in the barrier region and relaxation mechanisms that saturate the profile at equilibrium. The emphasis has been on regimes compatible with high core performance and acceptable divertor physics—that is, on regimes featuring complete suppression of large ELMs. To support these studies, profile diagnostics with resolution close to 1 mm were designed and deployed to measure electron and ion temperature, electron density, and plasma rotation.[115–117] C-Mod is also equipped with a set of fluctuation diagnostics including Langmuir probes, magnetic probes, gas-puff imaging (GPI), correlation reflectometry, phase-contrast imaging (PCI), and polarimetry with similar spatial resolution and sensitivity to the short wavelength modes that dominate the edge.[94,118–128]

A. H-mode access and the L-H threshold

Prediction of transport bifurcations, though challenging due to the complexity of the physics, is critical for extrapolation into burning plasma regimes. Without a computable, first-principles model, prediction of the threshold has been based on empirical fits to global operating parameters. At the time that C-Mod was under construction, existing empirical scaling laws for the L-H transition predicted power thresholds that ranged from 100 kW to 10 MW. Given the expected Ohmic and auxiliary power available, the breadth of this range implied that C-Mod might be "always in H-mode" or "never in H-mode." The wide range arose because of significant correlations in the existing data where machine size, plasma current, and input power all increased together and magnetic field had only a limited variation. Thus, the covariance of the regressors was such that multivariate fits had difficulty separating the effects of the different parameters. When experiments began, C-Mod quickly found a power

threshold on the order of 1–2 MW.[38] The inclusion of C-Mod data into multi-machine databases improved their overall condition, modified the empirical fit, and led to ostensibly more reliable predictions.[129] It is worth noting however that the empirical scalings do not yet capture all of the important dependences seen in the data. A crucial question related to the threshold is the minimum power requirement for full-performance H-modes—driving a need for data that supports a prediction for ITER, where the available power is not far above the empirical scaling. C-Mod experiments showed that the H-factor increases moderately, but linearly with power conducted through the pedestal and that $H_{98} \approx 1$ could be achieved with $P_{CONDUCTED}/P_{THRESHOLD}$ of about 1 as seen in Fig. 2 of Ref. 83.

As part of its critical contributions to the ITPA databases in support of ITER, C-Mod has carried out a series of dedicated experiments aimed at elucidating the role of parameters not included in the threshold scaling studies and supporting development of first-principles models through characterization of the transition in terms of local physics values. An important observation was the so-called "low-density limit" for the L-H transition.[130] Originally characterized as a density threshold,[131] carefully controlled studies in C-Mod with otherwise fixed conditions found that the dependence of the power threshold on density, which was roughly linear for the multi-machine power-law regressions, had instead a parabolic shape, with a distinct minimum power point and stronger than linear upturns at both lower and higher densities,[132] as seen in Fig. 21. C-Mod was the first device to test directly the empirical scaling of the optimum density $n_{th,opt}$ with magnetic field, confirming that $n_{th,opt} \sim B_T$,[133] a result recently confirmed by experiments on JET.[134] The transition between the low and high density branches is consistent with the transition between the sheath-limited and conduction-limited divertor regimes, as considered by Fundamenski *et al.*,[135] although further work is required to understand this connection. Similar results were reported from other experiments, suggesting that the multi-machine fits were capturing only the average behavior of an inherently more complicated dependence. The implications for extrapolation to ITER are still unclear, but it is certain
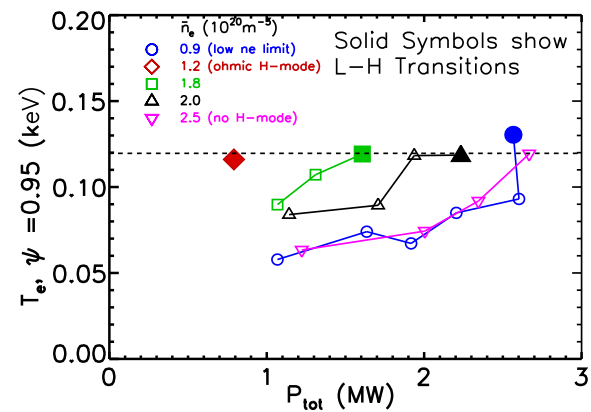
FIG. 22. The L-H transition was found to have a sharp threshold at a fixed temperature independent of density.[137] Reprinted with permission from Hubbard *et al.*, in *Proceedings of the 16th International Atomic Energy Agency Conference on Fusion Energy* (IAEA, Montreal, 1996), Vol. 1, p. 875. Copyright 1996 IAEA.

that a future machine cannot count on achieving H-mode at arbitrarily low power by simply lowering the L-mode target density. Neither can a burning plasma device assume that fusion power, increasing as the ion density squared for fixed temperature, will increase as fast as the threshold—that is, the plasma may not be guaranteed to stay in the H-mode during densification as previously assumed. The impact of divertor geometry was also studied on C-Mod where a significant drop, by as much as 50%, in the power threshold was found for a slot divertor when compared to the standard vertical target.[136] This reduction is best correlated to the extended low-field side connection length along the divertor arm. In the low density branch, the power threshold is found to be largely insensitive to divertor configuration.

C-Mod carried out some of the first studies on local edge plasma conditions at the transition, finding a critical T_e (or ∇T_e) at the threshold[137,138] that is independent of density, as seen in Fig. 22. These data were used to test emerging theoretical models.[139,140] Below the minimum threshold density, the transition may be better characterized as a critical pressure.[132] The local threshold is seen to increase roughly linearly with magnetic field, consistent with global scaling. Overall, the results suggest that some of the parametric dependence seen in the scaling laws arises from transition physics (for example, the B_T dependence) and some from the nature of L-mode turbulent transport (for example, the density dependence). Studies of hysteresis in the transition dynamics showed stable and unstable operating regions on the bifurcation curve.[141,142] The threshold L-mode profiles are roughly consistent with a model that had derived a collisionality-dependent critical pressure gradient for the transition.[90] Studies of edge turbulence with GPI have shown nonlinear turbulent kinetic energy transfer from the background drift-wave turbulence into sheared quasi-static flows.[143] As suggested by earlier work[144,145] these results found that this energy transfer rate equals the local drift-wave growth rate just before the L-H transition. The work on C-Mod showed for the first time that the large H-mode edge profile gradients develop after the transient zonal flow generation and turbulence suppression phenomena—clearly
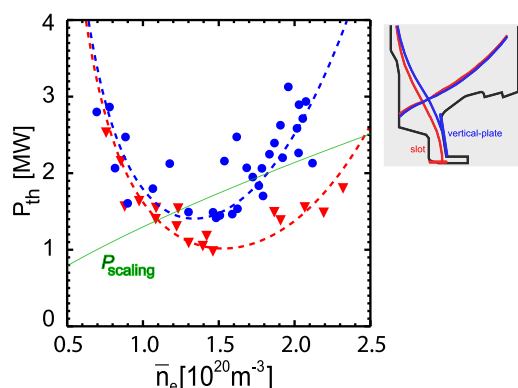

FIG. 21. The L-H power threshold vs plasma density has a distinct minimum and rises faster than linearly on either side. A strong dependence of the threshold on divertor topology is found on the high density side. Greenwald *et al.*, Nuclear Fusion **53**, 14, 104004 (2013). Copyright 2013 International Atomic Energy Agency.[197]
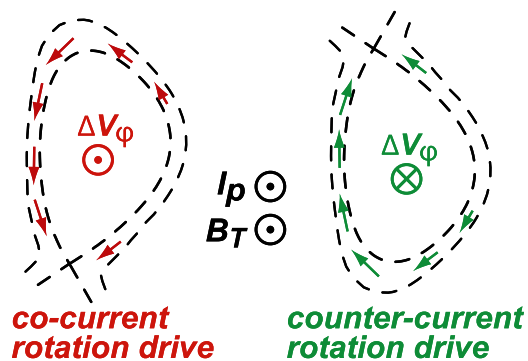
FIG. 23. The direction of SOL flows driven by poloidally asymmetric radial transport depends only on the direction of the ∇B drift relative to the direction to the x-point. For all combinations of toroidal field, plasma current or X-point direction. Reprinted with permission from LaBombard *et al.*, Nuclear Fusion **44**, 1047 (2004). Copyright 2004 IOP.[112]

demonstrating the temporal sequence of events that leads to the H-mode regime.

The topology-dependent flows seen in the C-Mod L-modes, described in Sec. III E 2 and shown in Fig. 23, have contributed toward an explanation to a longstanding mystery—that is, the effect of the ion drift direction on the H-mode threshold. Starting with the earliest work on ASDEX, all tokamaks have seen a substantially higher power threshold when the ion ∇B drift direction is away from a single-null x-point (usually called the unfavorable drift direction) when compared to otherwise identical conditions with the ion drift toward the x-point (the favorable drift direction).[137,146,147] The difference in the power thresholds, which can be a factor of 2–3, has had no satisfactory explanation. The SOL flows, we have described, are driven by poloidally asymmetric turbulent transport and are always in the co-current direction when in the favorable drift condition and in the counter-current direction for the unfavorable case. This is true for all combinations of toroidal field direction, plasma current direction, and x-point location.[113] The flows in the SOL are mirrored by intrinsic flows measured in the core.[148] This may be a result of momentum transported from the boundary into the core as described below in Sec. V B. Figure 24 shows the behavior of these flows as a function of magnetic geometry and demonstrates the strong correlation between the geometry, flows, and L-H threshold. In this plot, the x-axis variable named SSEP is the distance between the primary and secondary separatrices mapped to the midplane. Positive values of SSEP correspond to upper single-null geometries and negative values correspond to lower single-null. In this case, the ion drifts are down; thus, negative SSEP is the favorable drift direction. One can see that the flows and threshold are sensitive to geometry on the scale of a few mm—which is a scale length characteristic of the SOL. Since prevalent theories and experimental evidence for the L-H transition points toward flow shear suppression,[149] it seems plausible that this change in equilibrium flow direction results in the different power threshold observed. Confirmation will only come, however, with a comprehensive, validated, first-principles model for boundary transport and the L-H bifurcation.
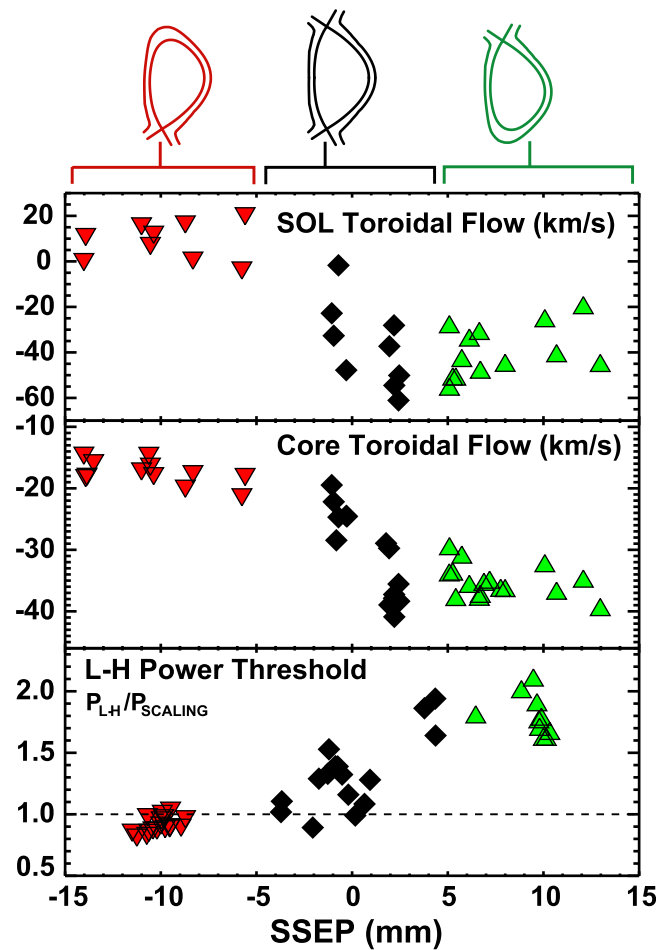

FIG. 24. The L-H power threshold is well-correlated with the topology-dependent flows seen in the plasma edge and core. The independent axis, SSEP is the distance between the primary and secondary separatrices, mapped to the midplane. Reproduced with permission from Phys. Plasmas **12**, 056111 (2005). Copyright 2005 AIP Publishing LLC.[113]

B. ELMy H-mode

The EDA (Enhanced D-Alpha described in Sec. IV C 1) was the first type of stationary H-mode seen on C-Mod and is, by far, the most prevalent H-mode regime. ELMy H-modes, common on most devices, are also routinely achieved. The ELMy form of H-mode was first seen in dimensionless scaling experiments where C-Mod was run with a shape similar to the JFT-2M tokamak.[150] These discharges have good plasma performance, with $H_{98} \approx 1$ and are stationary, with particle and impurity transport apparently controlled by the periodic ELMs and residual fluctuations seen between ELMs. The power threshold for transition to ELMy and EDA discharges are similar. A key ingredient in producing this type of discharge in C-Mod is to place the strike-point deep in the divertor slot. The recycling patterns of this geometry combined with the particle transport intrinsic to the ELMy regime, provide density control and allow operation at plasma densities lower than the more common EDA regime. This leads to lower collisionality and thus to higher edge bootstrap current. In addition the reduced shaping of the discharge in these cases lowers their stability to
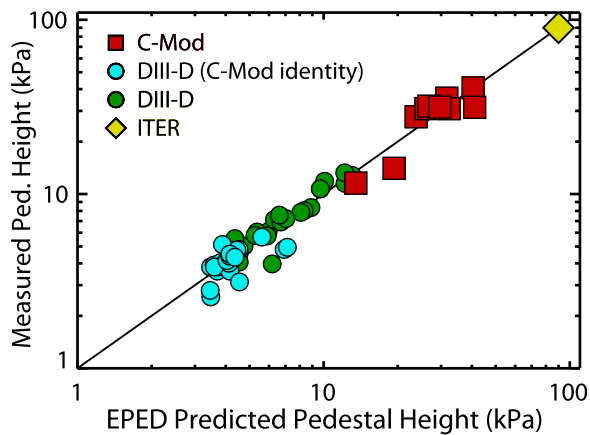
FIG. 25. The measured profile structure is consistent with the EPED model, extending the world database to within a factor of three of what is expected on ITER. Hughes *et al.*, Nuclear Fusion **53**, 8, 043016 (2013). Copyright 2013 International Atomic Energy Agency.[154]
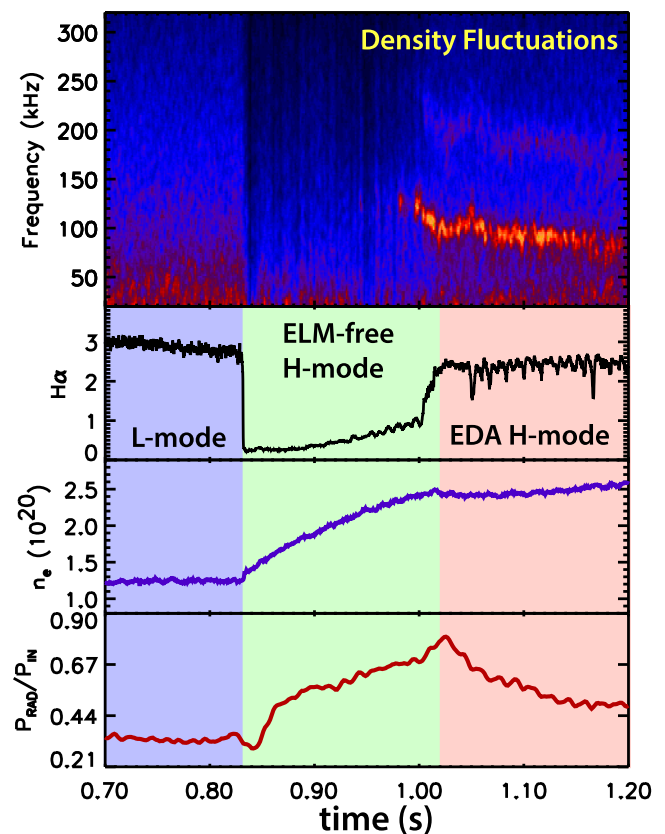

FIG. 26. A sudden transition from the ELMfree to the EDA H-mode is accompanied by a change in impurity confinement and the appearance of the QCM. Greenwald *et al.*, Fusion Sci. Tech. **51**, 266 (2007). Copyright 2007 American Nuclear Society.[185]

peeling-ballooning modes. While sufficient to bring the discharge to a stationary state, the ELMs are always "small" in the sense that the reduction in particle and energy inventory is well under 1% per ELM. Stability calculations with ELITE are consistent with operation near the high-n or ballooning side of the peeling-ballooning stability diagram.[151] This combination of conditions exist on C-Mod in a restricted window in shaping ($\delta_U < 0.3$, $\delta_L > 0.7$, and $\kappa < 1.6$).

Data from the ELMy discharges were compared successfully to the EPED model,[152] substantially extending the tested data range for magnetic field and pedestal pressure, approaching the values predicted for the ITER pedestal (see Fig. 25).[153,154] The EPED model predicts pedestal height and width through the simultaneous solution to linear stability models for MHD peeling-ballooning and kinetic-ballooning modes (KBMs). A good agreement was found, demonstrating weak β_P dependence of the pedestal width, consistent with the KBM arguments. Ideal infinite-n ballooning mode calculations as a proxy for the KBM also show marginal stability to KBM. Recent electromagnetic signatures observed between ELMs and described below are possible evidence for KBM pedestal-regulating activity.[155] Separately, ELM precursors have also been documented along with multiple "secondary" filaments following the primary ELM filament ejection.[156]

C. High-performance edge-barrier modes without ELMs

While the H-mode provides a good energy confinement needed for burning plasma devices like ITER and fusion reactors, it brings with it several unfavorable characteristics. The particle transport barrier can be too good, with the potential to accumulate high-Z impurities and the concomitant high levels of radiated power. Even more daunting is the prospect of large ELMs, resulting from an overly steep pressure gradient. In the absence of other mechanisms, large ELMs relax this gradient leading to periodic exhausts of power that cannot be tolerated in large-scale devices.[157,158] Methods of external control that increase the frequency of ELMs and thus decrease their impact are being

explored,[159,160] but their applicability and reliability in a reactor environment is uncertain. Thus, there is an unmet need for intrinsic operating regimes with a good energy confinement but with either very small ELMs or with none at all. Two such ELM-suppressed regimes have been discovered and studied on C-Mod. These are the EDA or the Enhanced D-Alpha H-mode and the "Improved" or I-mode, which are obtained at a high and low collisionality, respectively.

1. EDA H-mode

The EDA regime is the standard H-mode on C-Mod, seen early in its operation upon the first application of high-power ICRF in a well-conditioned machine.[17,161] Compared to ELM-free operation, EDA tends to be favored at higher collisionality (or higher density) and higher safety factor (q_{95}).[162] It is also found that EDA is achievable in hydrogen at lower q_{95} than it is in deuterium. A dependence on shaping has also been seen but this is complicated and not fully understood.[162,163] The EDA regime is not specific to ICRF heating as it is obtained in Ohmic H-modes when similar access conditions are met. Energy confinement in EDA can be variable, but H_{89}, the energy confinement time normalized to the ITER89 L-mode scaling[164] in the range 1.6–2.0 was readily obtained.[17] C-Mod EDA data were part of the international collection used to develop the ITER98 H-mode scaling laws.[165,166] The salient feature of the EDA regime (and the reason for its name) is the high levels of recycling
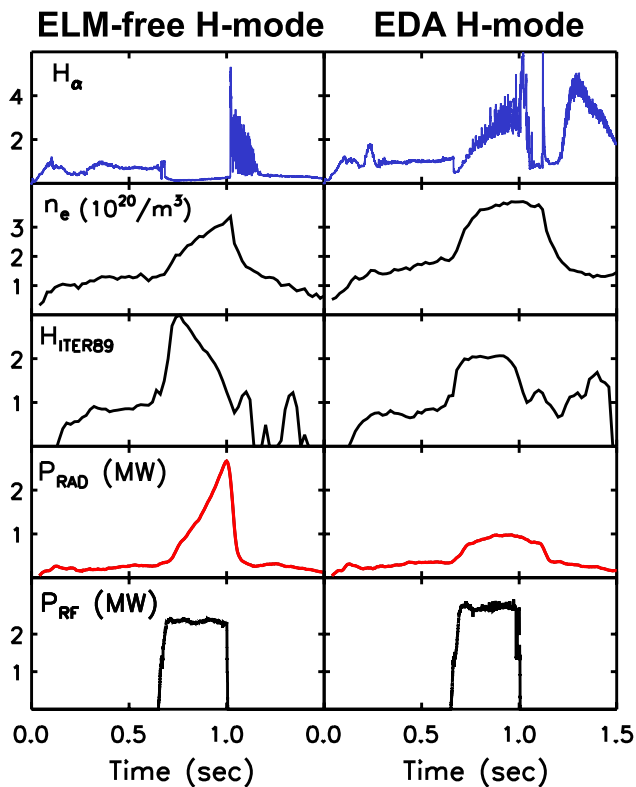
FIG. 27. A comparison of waveforms between the ELM-free and the EDA H-modes shows the essential stationary character of the EDA and the drop in particle and impurity transport. Greenwald *et al.*, Fusion Sci. Tech. **51**, 266 (2007). Copyright 2007 American Nuclear Society.[185]

light. Compared to an ELM-free H-mode, where the level of radiation from neutral deuterium (or hydrogen) drops sharply at the L-H transition and remains very low, in EDA, this signal returns quickly to or exceeds L-mode like values. The implication is that edge particle transport is much higher in EDA. Impurity transport is even more strongly affected. While impurities can accumulate in an ELM-free discharge, they pump out readily in EDA as seen in Fig. 26 as a sudden change in the time derivative of radiated power. The result is that impurity radiation and electron density are under control, allowing a stationary state to be achieved. The main features of the EDA can be seen in Fig. 27, which compares traces from similar 1 MA, 5.4 T EDA, and ELM-free discharges. Notable is the stationary particle and energy content, the lower levels of impurity radiation and the difference in deuterium Balmer-α brightness. The change in particle transport is associated with and attributed to a plasma fluctuation not seen in ELM-free discharges. The transport caused by this mode is apparently sufficient to hold the pressure gradient below the MHD stability threshold and avoid any large ELMs.[154,167] More detail on the characteristics and effects of this fluctuation, termed the "quasi-coherent mode" or QCM, are given in Sec. IV D. In some EDA discharges, typically with $\beta_N > 1.2$, very small, energetically insignificant ELMs are also observed.

The pedestal in the EDA H-mode is narrow in C-Mod, typically 2–4 mm,[168] and spans roughly the same fraction of the normalized poloidal flux as pedestals in ELMy discharges.[154] The pressure at the top of the pedestal scales

with $I_P{}^2$, with the dependence equally partitioned between density and temperature. The dependence on other parameters such as plasma density, toroidal field, or shaping is weaker—suggesting that, as in the SOL, β_P or α_{MHD} is the controlling parameter. To further investigate the importance of plasma physics vs atomic physics (i.e., neutral penetration) in determining the pedestal structure, a series of dimensionless identity experiments was carried out in collaboration with DIII-D. The experiments matched all geometric and plasma dimensionless parameters at the top of the pedestal. The result was a good match across the entire pedestal—suggesting that plasma physics alone can account for the structure of the density and temperature profiles.[169] Later similarity studies conducted in ELMy H-modes showed evidence of a mismatch in density pedestals, with the DIII-D pedestal being wider in flux space.[170] These matches required DIII-D to operate at its lowest feasible H-mode densities, in a regime known to show a dependence of the pedestal width on neutral penetration[171] that is not seen on C-Mod, suggesting that the neutral penetration range can have an effect on sufficiently transparent pedestals.[172] However, C-Mod has the highest neutral opacity of any operating tokamak and should be more prototypical of ITER/Reactor conditions.

2. I-mode

By operating at high power under conditions where the L-H threshold is elevated, C-Mod has explored a new and even more promising regime—the I-mode (short for Improved Mode).[116,173,174] The I-mode combines the H-mode like energy confinement ($H_{98} \approx 1$) with the L-mode particle and impurity confinement, and is generally ELM-free. The change in global confinement and the drop in core thermal diffusivity are mirrored by a drop in core fluctuations, with $\delta n_e/n_e$ decreasing by 30% and $\delta T_e/T_e$ by at least 70%.[175] (The I-mode regime described here must be clearly distinguished from "I-phase" a regime of fast dithering between the L and H-modes reported on some machines at powers near the L-H threshold.[176]) Most commonly, the I-mode is accessed by running with the ion ∇B drift in the direction unfavorable for the H-mode operation, though it has also been observed in the standard configuration. The window in input power is higher for the "unfavorable" field direction, and allows powers up to about $2\times$ the L-I threshold before an I-H transition is encountered. The I-mode was probably first obtained in some of the earliest ICRF heating experiments on C-Mod in 1996, where improved energy confinement and higher pedestal temperatures were seen for "reversed field L-modes." They were categorized as L-modes due to the lack of density rise that accompanies the H-mode.[17] Similar plasmas were called improved L-mode on ASDEX-Upgrade.[177] Limitations on diagnostic coverage and the lack of an accurate H-mode scaling law at the time prevented clear recognition of this phenomena as a new and distinct confinement regime. The higher local Te threshold and multi-step dynamics with unfavorable drift were later studied in more detail.[178] These early observations suggests
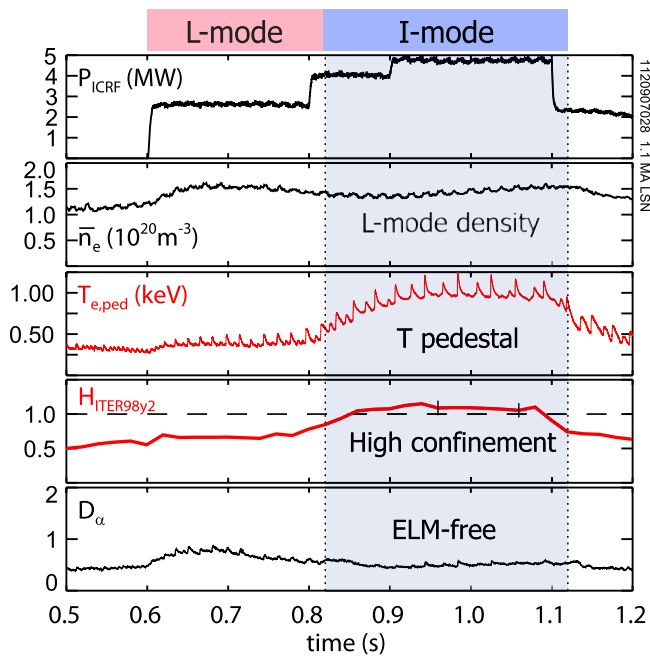
FIG. 28. The transition from the L to I-mode is shown, demonstrating the increase in energy confinement without a change in particle transport or the appearance of ELMs.[179] Reprinted with permission from Hubbard *et al.*, in *Proceedings of the 24th IAEA Fusion Energy Conference* (IAEA, San Diego, 2012), see http://www-naweb.iaea.org/napc/physics/FEC/FEC2012/papers/171_EX13.pdf. Copyright 2012 IAEA.

that the I-mode is not an exotic and elusive regime, but is rather a standard behavior under suitable conditions.

Figure 28 shows time traces from a typical I-mode and illustrates the salient characteristics.[179] While the edge temperature and stored energy increase markedly as they would in an H-mode, there is no change observed in the plasma density at the L-I transition or thereafter. This difference is
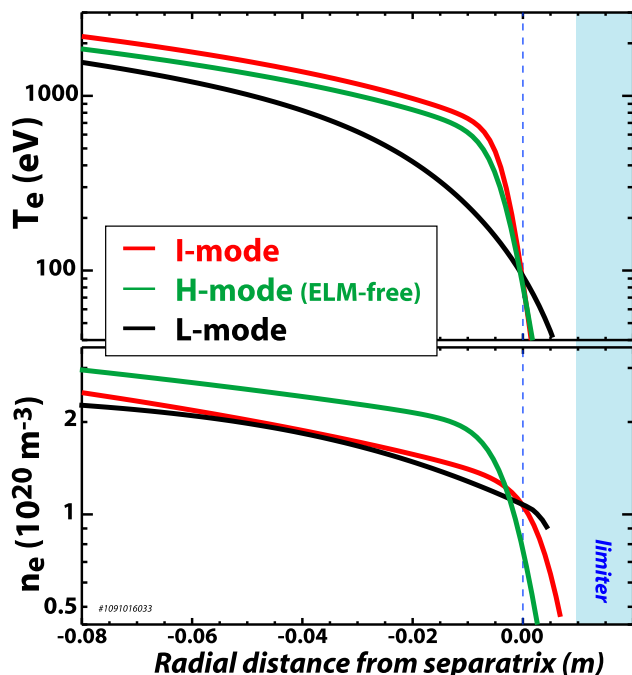
FIG. 29. The profiles of electron temperature and density are compared for the L-mode, H-mode, and I-mode.
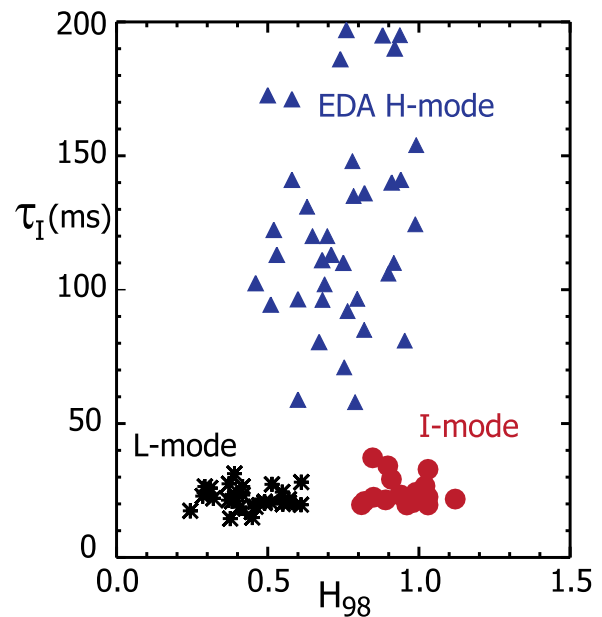

FIG. 30. The confinement times of calcium impurities, injected via the laser blow-off technique, are plotted vs normalized energy confinement and confirm the L-mode-like particle transport for the I-mode plasmas.

seen dramatically in Fig. 29, which compares the edge profiles between the L-mode, the I-mode, and the H-mode. The I-mode temperature profile is distinctly H-mode like, while the density profile retains the L-mode shape and values.[154] Just as in the H-mode, an E_r well is observed in the I-mode,[116,180] though shallower than in the H-mode. The pedestal pressure gradient is lower in the I-mode than in the H-mode and stability analysis finds it stable to peeling-ballooning.[151,154] The L-mode like density profile is probably responsible for the lack of ELMs due to its impact on the pressure gradient and a drop in the density gradient drive for bootstrap current. In contrast to the EDA regime, where high collisionality is responsible for reducing the bootstrap current, I-modes are amongst the lowest collisionality, improved confinement regimes in C-Mod, with ν^* at the top of the pedestal as low as 0.1. Weak, energetically insignificant ELMs are observed in some I-modes, arising from pedestals far from the peeling-ballooning boundary and are often triggered by sawteeth. Impurity transport in the I-mode is essentially at the L-mode levels as seen in Fig. 30, which plots the energy and impurity confinement time measured from calcium impurities injected via laser blow-off (LBO)[181] for the three regimes. As a result, the I-mode performance is considerably less sensitive to wall conditioning (boronization) than the H-mode's and more easily compatible with high Z PFCs and impurity seeding than the H-modes.

Overall, the I-mode has the advantages of the H-mode without its drawbacks. The I-mode is an ELM-suppressed, high-temperature, low collisionality regime without impurity accumulation. The density can be controlled by gas puffing, and the density profiles are mildly peaked as in the L-modes or the low-collisionality H-modes.[182] Strong fueling also seems to help avoid the I-H transition. So far, limits to the I-mode performance have been set by the power available on C-Mod (4–5 MW). Based on current results, it might be
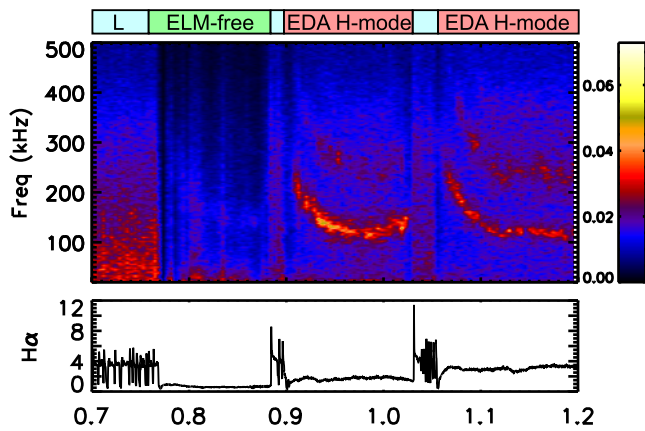
FIG. 31. The density fluctuation spectra are shown for a discharge with three H-mode periods. The first is ELM-free followed by two EDA intervals with the presence of a strong QCM. Greenwald *et al.*, Fusion Sci. Tech. **51**, 266 (2007). Copyright 2007 American Nuclear Society.[185]

possible to operate at $Q = 10$ if an I-mode could be achieved in ITER,[179] though much more information is needed on density, field, power, and size dependence for the I-mode access and on the confinement properties of the regime across a larger range of machines. The divertor heat footprint in the I-mode is somewhat wider than that in the H-mode, and more equal power sharing is seen between the inner and outer strike point—both favorable characteristics for divertor power handling.[78] And aside from the intrinsic interest in the I-mode as an attractive reactor regime, the decoupling of energy and particle barriers should also illuminate the physics of edge barriers.

D. The role of short wavelength electromagnetic modes in regulating the edge transport barrier

Short-wavelength electromagnetic fluctuations apparently play an essential role in regulating pedestal profiles in all edge barrier regimes observed on C-Mod. When sufficiently strong, these fluctuations can maintain the pressure gradient below the threshold for peeling-ballooning and effectively suppressing ELMs. These observations suggest the possibility of external control by launching waves that stimulate or destabilize this class of plasma fluctuation.

1. The QCM in EDA H-modes

In EDA H-modes, the increase of particle and impurity transport over ELM-free discharges is due to very large amplitude, narrow-band fluctuations observed by every diagnostic capable of detecting short-wavelength fluctuations in the plasma edge, including reflectometry,[119,183] phase-contrast imaging,[121] Langmuir probes,[184] magnetic loops,[120] gas-puff imaging,[110] and polarimetry.[127] The QCM frequency is typically in the range of $f \sim 50$–150 kHz and field aligned ($k \cdot B = 0$) with an outer-midplane poloidal wavenumber, $k_\theta \sim 1.5\,cm^{-1}$. As suggested by the name, the QC frequency spread is typically small, $\delta f / f \sim 0.05$–0.15. The evolution of the autopower spectrum of this mode in typical EDA H-modes is shown in Fig. 31. It may be notable that broadband fluctuations in the same ω and k range are prevalent in L-

mode discharges and believed to be a key component in boundary plasma transport. Multi-field measurements of the mode have been made recently using "mirror probe" electronics,[184] showing mode amplitudes in plasma density, $\delta n_e / n_e \sim 0.3$; electron temperature $\delta T_e / T_e \sim 0.45$, plasma potential $\delta \phi / T_e \sim 0.45$, and magnetic field, $\delta B \sim 0.4\,mT$, $\delta J \sim 25\,A/cm^2$. Measurements from an active antenna (described in Sec. IV D 4) find that the mode has weak damping or growth rates with γ / ω on the order of 5%–10%. This suggests weak nonlinearities in the mode dynamics and may explain the narrow frequency width even as the mode grows to such large amplitudes. The mode can be precisely located in Ohmic EDA H-modes, where power levels are low enough to make probe measurements across the pedestal, and is found to span the separatrix with a full-width at half maximum of 2–3 mm. That places it in a region of positive E_r, that is, with the $E \times B$ flow in the ion diamagnetic direction. These measurements allow the calculation of the wave propagation in the plasma frame, which is found to be unambiguous in the electron diamagnetic direction. As seen in Fig. 31, the mode often chirps to lower frequency as the EDA H-mode develops—likely a result of the change in the Doppler shift as the equilibrium electric field well deepens. The connection between the mode and enhanced particle transport can be seen macroscopically—as the near-SOL particle diffusivity is proportional to the mode amplitude[185]—or can be computed microscopically from the fluctuation amplitude and phase relations. The plasma potential fluctuations are found to lag the density fluctuations by 16 deg and the temperature fluctuations by 7 deg, consistent with the identification of the mode as a drift wave. The T_e response is not simple Boltzmann, perhaps not surprising given the electromagnetic character of the wave. With these observations, we would describe the mode as an electromagnetic drift-wave, driven by pressure gradients and curvature. Fluid simulations[90,186] find similar modes and suggest that the mode is probably modified by the magnetic shear near the plasma x-point.

2. The weakly-coherent mode (WCM) in the I-mode

The fluctuations apparently responsible for regulating the pedestal in the I-mode are at somewhat higher frequency than the QCM, typically in the range of 200–300 kHz and considerably broader, $\delta f / f \sim 20$%–50%, but with a similar wavelength, $k_\theta \sim 1.5\,cm^{-1}$. The WCM fluctuations can readily be seen in diagnostics looking at electron density, electron temperature, and magnetic field. The fluctuation amplitudes are smaller than for the QCM with $\delta n_e / n_e$ on the order of 10% and $\delta T_e / T_e$ in the range of 1%–2%.[187] The appearance of the WCM is accompanied by a drop in lower frequency, broad band fluctuations as seen in Fig. 32. The effective particle diffusivity, $D_{EFF} \propto \Gamma / \nabla n$, is found to be proportional to the amplitude of the WCM,[188] supporting its role in the I-mode particle transport. By contrast, the amplitude of fluctuations below 150 kHz are strongly correlated with energy diffusivity,[174] further suggesting that turbulence in this range is responsible for energy transport in the L-mode target plasmas. Geodesic Acoustic Modes (GAMs), a
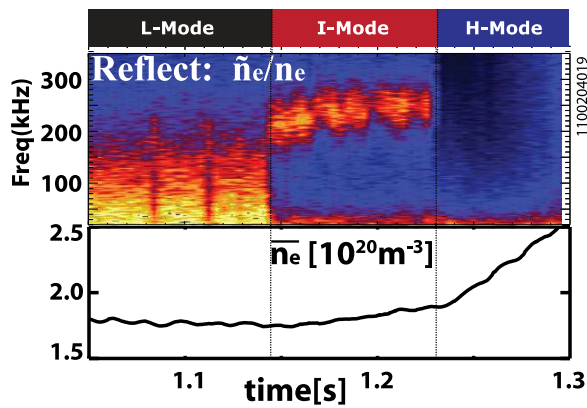
FIG. 32. Density fluctuations are shown a discharge transitions from the L- to I- to H-mode. The I-mode is typically accompanied by the appearance of a WCM at frequencies above 200 kHz and the reduction in lower frequency fluctuations. Reproduced with permission from Phys. Plasmas **18**, 056115 (2011). Copyright 2011 AIP Publishing LLC.[152]

fluctuating form of zonal flows have been observed in the I-mode and persist throughout the regime. These play a critical role in the development of the WCM as demonstrated by bispectral analysis that shows power transfer between the WCM and the GAM.[189] This observation also suggests that the GAM is responsible for depleting power from the lower frequency turbulence and thus in the suppression of energy transport in the I-mode. The I-mode is the only regime in C-Mod with coexisting strong mean and fluctuating shear flow. These observations may help us understand how the transport bifurcation occurs in two distinct steps—L to I and then I to H, along with the difference in transport characteristics in each of the regimes.

3. Fluctuations that regulate transport in ELMy discharges

Short-wavelength electromagnetic fluctuations also play a role in ELMy discharges, though in these cases the effects are not large enough to prevent the larger-scale MHD instabilities from arising. The conventional picture is that the pedestal pressure profiles come into equilibrium rather quickly between the ELMs, which are caused by unstable current profiles that take longer to evolve.[190,191] (Recent results suggest some modification of this picture, suggesting relatively rapid pedestal current evolution in the ELM cycle,[192] and detailed profile analysis has shown that more subtle evolution is possible, with pressure gradients saturating early in the ELM recovery phase, followed by a slower increase of both the pedestal height and the width that eventually results in a peeling-ballooning instability.[170]) A long-standing question concerns the transport processes that dominate the pressure profile evolution between the ELMs. As discussed above, the successful EPED pedestal model is based on the hypothesis that KBMs control the pressure profile during the build-up to an ELM.[152] On C-Mod, T_e drops after each ELM then quickly recovers. As the temperature recovers, pedestal localized fluctuations are observed to build up, as seen in Fig. 33, with $k_\theta \rho_s \sim 0.04$, that is, with wavenumbers somewhat lower than for the QCM and WCM discussed above.[155] The mode amplitude scales with electron β (T_e and T_i are
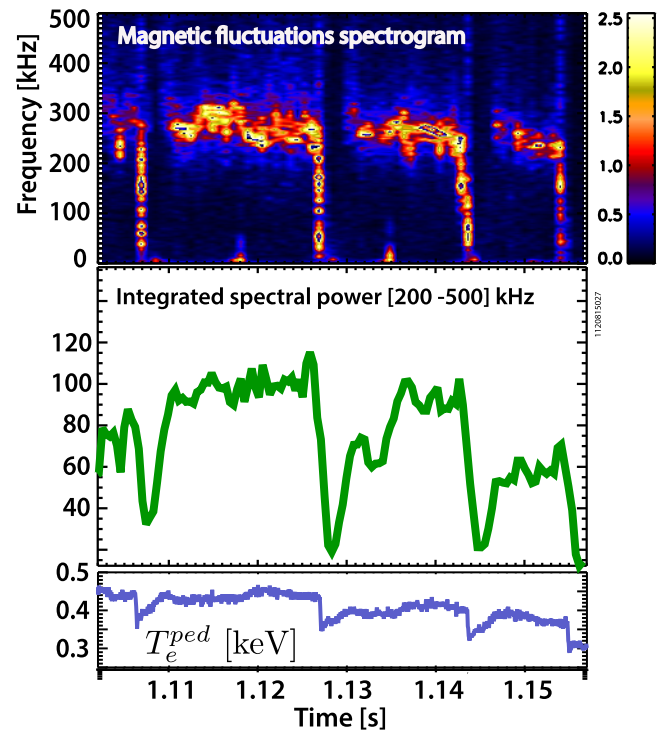

FIG. 33. Magnetic fluctuations are shown to grow rapidly as the plasma temperature recovers between the ELMs. These fluctuations may be evidence for kinetic ballooning, a key element in the EPED model for pedestal structure. Hughes *et al.*, Nuclear Fusion **53**, 8, 043016 (2013). Copyright 2013 International Atomic Energy Agency.[154]

equilibrated) consistent with expectations for the KBM. Immediately after each ELM, this mode disappears. Stability analysis with the GS2 gyrokinetic code[193] finds a mode at $k_\theta \rho_s \sim 0.03$ with KBM characteristics and work on mode identification is ongoing.

4. External control of edge transport

These results open the possibility that the pedestal transport, the overall plasma performance, and the presence of ELMs might be controlled through an external means. Early success was achieved using microwaves in the LH range of frequencies. In these experiments, a modest level of LH power at 4.6 GHz is applied to the high density EDA H-mode discharges ($n_e > 2 \times 10^{20}/m^3$) where the waves have little or no accessibility to the core plasma.[194] A large
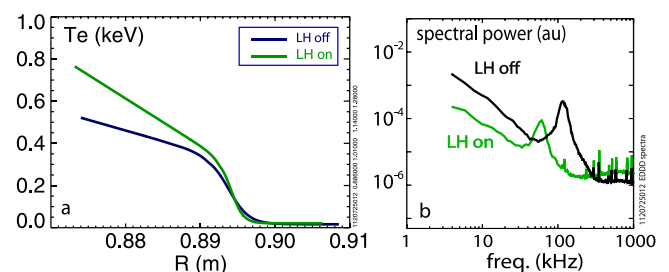

FIG. 34. (a) The increase in the temperature pedestal after the application of a small increment in RF power in the lower-hybrid range of frequencies applied to plasmas strongly heated by ICRF. (b) The increase in temperature is accompanied by a drop of almost an order of magnitude in edge fluctuations.
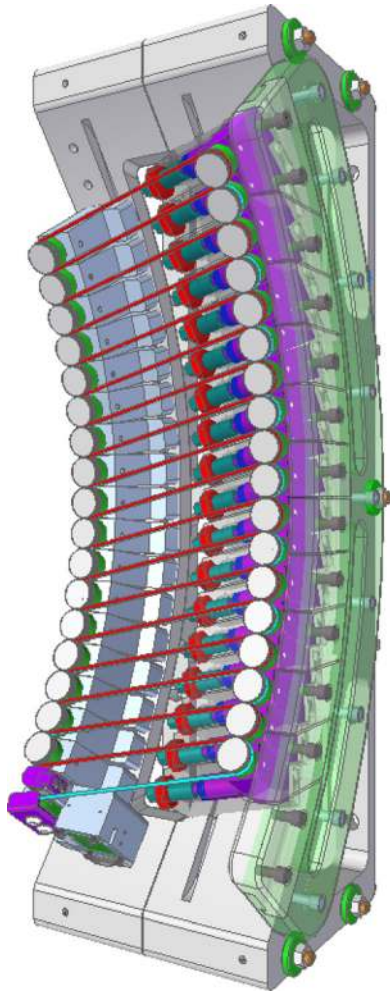
FIG. 35. A 3D rendering of the "shoelace" antenna, which can drive short wavelength magnetic perturbations in the plasma edge.
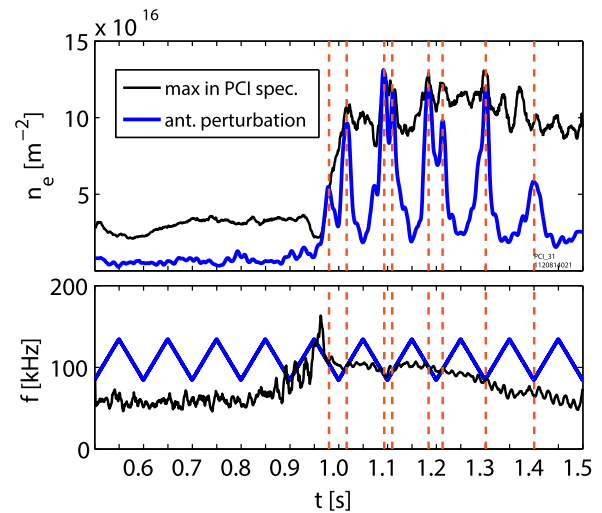

FIG. 36. The magnetic perturbation applied by the shoe-lace antenna drives a strong plasma density response when the drive frequency is at or near resonance with the naturally occurring QCM. Reproduced with permission from Phys. Plasmas **21**, 056111 (2014). Copyright 2014 AIP Publishing LLC.[113]

fraction of the launched power appears promptly on the outer divertor target, supporting modeling that shows that the waves propagate only in the plasma edge. The experimental result can be seen in Fig. 34(a), which shows an increase in pedestal temperature when the LH was applied to an ICRF heated H-mode. In the highest density cases, the overall stored energy increase can be as much as 30%, which would require almost 3 MW of additional heating if the confinement were fixed and followed the H_{98} scaling. In the experiment, this was accomplished with only 0.6 MW of the LH power. At the same time, we have observed the level of edge fluctuations on flux tubes, which pass in front of the LH launcher, to drop by almost an order of magnitude as seen in Fig. 34(b). The mechanism by which the LH decreases energy transport is under investigation.

Another approach tries to more directly mimic the intrinsic plasma behavior by driving the QCM- or WCM-like fluctuations in the plasma with an external antenna.[195] This so-called "shoe-lace" is essentially an active MHD antenna for short wavelength electromagnetic modes. The antenna is named after the geometry of the antenna winding, which can drive currents in the plasma edge in the relevant k range (see Fig. 35). An innovative matching network allows consistent coupling across a wide range of frequencies, 50–300 kHz.[196]

With the existing RF sources, the antenna currents can reach about 80 A and could be increased further without excess antenna heating. Because of the rapid fall-off in these short wavelength perturbations, the launching structure incorporates protection tiles and is designed to operate safely with no more than 1 cm clearance between the windings and the plasma edge. The antenna can be operated in a passive mode as a sensitive receiver, but the primary mode is active, where waves launched by the antenna are observed with the array of C-Mod edge fluctuation diagnostics. The antenna frequency can be swept to look for resonances with the plasma or phase locked to existing perturbations. In the H-mode, when a plasma pressure pedestal is present, the antenna will drive both the magnetic and density fluctuations. The density response is absent in the L-mode, suggesting that the antenna strongly interacts with modes that are driven by the pressure gradient. From the plasma response, a transfer function is computed, peaking when the drive frequency equals the QC frequency, as seen in Fig. 36. The density perturbation approaches the intrinsic mode amplitude when the drive is on resonance. A response is seen in the H-mode plasmas even if the QC mode is absent, indicating a damped rather than growing instability in those cases. From the transfer function calculation, it is determined that the plasma mode is propagating in the electron diamagnetic direction and is weakly damped or growing with $\gamma/\omega \sim 0.05$–0.10. This observation helps account for the high level of coherency. The narrow spectrum is consistent with the lack of strong nonlinear damping, limiting the spread in k and ω space. Future experiments will attempt use this actuator as a tool to modify pedestal transport.

V. CORE TRANSPORT

Core transport studies in C-Mod generally feature strong electron heating, equilibrated electrons and ions, no external torque, and no core particle sources. The exclusive use of RF

for heating provides a particularly good platform for studies of intrinsic rotation and particle transport. Several of the dimensioned quantities, B_T, n_e stand well apart from other experiments, but discharges with substantial overlap in dimensionless plasma parameters are also obtainable.[185,198] C-Mod provided important contributions to the H-mode confinement database. Operating at higher current and input power than other small devices, these data broke important covariances between size, current and power, the most important scaling parameters, and led to the ITER98y scaling laws.[165,166] It is worth noting that the C-Mod data, used in this database, were obtained in the ELM-suppressed regimes, with dominant electron heating, low torque, $T_e \sim T_i$, and in a device with metal walls. All of these are ITER-typical and different from conditions behind most of the data in the confinement database. Recent results from AUG and JET find a drop in energy confinement under similar conditions,[44] suggesting that ITER98 may overestimate the results that will be obtained on ITER.

A. Profile stiffness and temperature profile self-similarity

Early H-mode studies noted the simultaneous increase in core energy confinement and the formation of an edge transport barrier;[131] however, the first quantitative studies of the correlation between the pedestal and core transport were carried out in C-Mod.[17] These studies found a linear relationship between the height of the temperature pedestal and the normalized confinement time as shown in Fig. 37, unifying the C-Mod database across confinement regimes. It was found that the correlation was due to the self-similarity of temperature profiles. Figure 38 shows temperature profiles for a collection of 100 randomly chosen shots and times, at a wide variety of plasma density, heating power, impurity content, and regime (OH, L, and H).[185] The temperature is plotted on a log scale, demonstrating constancy of the logarithmic gradient $1/L_T = \nabla T/T$ over almost an order of magnitude variation in temperature magnitude. This result is consistent with transport theory that predicts a drift-wave
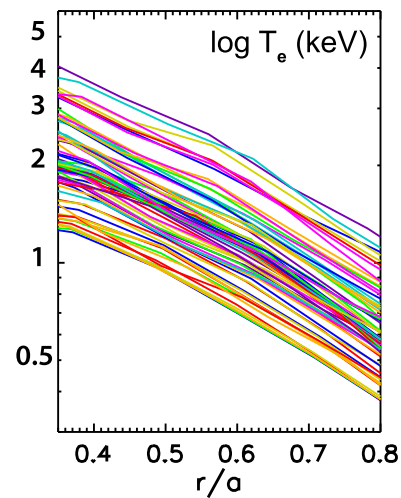

FIG. 38. Profile self-similarity is demonstrated. Te profiles are plotted, on a semi-log scale for a random selections of shots and time including the OH, L-mode, and H-modes at a wide range in density and input power. Greenwald *et al.*, Fusion Sci. Tech. **51**, 266 (2007). Copyright 2007 American Nuclear Society.[185]

stability threshold dependent on R/L_T and a strong turbulence and transport for normalized gradients that exceed the threshold.[199] These theories also predict a dependence of the critical gradient length on magnetic shear; thus, the shots in Fig. 38 were selected at the same magnetic field and plasma current. Nonlinear gyrokinetic simulations found, in fact, quantitative agreement between the experimental temperature gradient and the gradient computed to match the experimental heat flux.[200] These results also help to explain the insensitivity of the L-mode confinement to impurity radiation. It was observed that the L-mode confinement followed the empirical scaling even when virtually all power was lost through radiation before reaching the plasma edge, as seen in Fig. 39.[17] Apparently even the greatly reduced levels of heat conduction seen for the high radiated power were sufficient to sustain the plasma near the marginal stability point. In contrast, the H-modes are sensitive to the radiated power
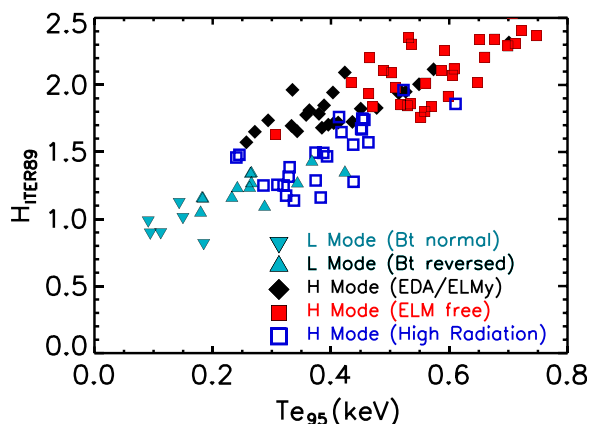

FIG. 37. The energy confinement time, normalized to the ITER89 L-mode scaling law, is plotted vs the pedestal temperature, unifying data over a wide range of parameters and confinement regimes. Reprinted with permission from Greenwald *et al.*, Nuclear Fusion **37**, 793 (1997). Copyright 1997 IOP.[17]
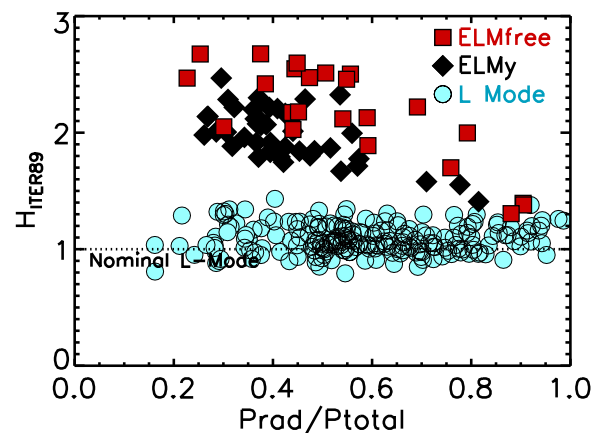

FIG. 39. Normalized energy confinement for the L-mode can be maintained, even at very low levels of conducted power. In contrast, the H-mode confinement deteriorates at a high radiated power because of the decrease in pedestal temperature. Reprinted with permission from Greenwald *et al.*, Nuclear Fusion **37**, 793 (1997). Copyright 1997 IOP.[17]

fraction through the degradation of the pedestal. Taken together, this work has suggested that the flux-gradient response is a more useful model than one that characterized heat transport in terms of the thermal diffusivity. The implications for burning plasmas, like ITER, are that fusion power will be strongly linked to the pedestal temperature. It is also worth noting that these observations combined with those for the pedestal and SOL, described in Secs. III and IV, suggest that most of the plasma is organized by marginal stability conditions.

The nonlinear flux-gradient response is mirrored by observations of core fluctuations and transient heat transport. For example, transport in the H-mode is reduced compared to the L-mode, not only at the edge but also in the core. A matched pair of the L and H-modes with the same I_P, B_T, and P_{RF} have the same temperature gradient scale length and the same heat flux but with the plasma temperature, temperature gradient, and plasma density significantly higher in the H-mode (from which one would calculate a factor of 2 reduction in thermal diffusivity).[17] The appropriate normalization for heat flux is the gyro-Bohm power $\propto nT^{3/2}$ and is thus substantially higher for the H-mode parameters, implying that the normalized heat flux is lower for the H-mode case than for the L-mode. In the experiments, fluctuations, $\tilde{n}_e/n_e$, $\tilde{T}_e/T_e$, in the core of L-mode are found to be higher, as expected from these arguments.[201] Similar observations are seen when comparing the core of the L and I-mode plasmas.[175] The rapid propagation of temperature perturbations, for example, from sawtooth oscillations is consistent with this picture.[202] The perturbations respond to the steep slope of flux vs gradient that exists at the discharge operating point. By comparison, the thermal diffusivity is simply proportional to the ratio of flux to gradient and is thus much lower than the local slope and does not predict the fast evolution of the profile that is observed.

B. Momentum transport and intrinsic rotation

Enabled by a high-resolution X-ray imaging crystal spectrometer (XICS),[203] capable of measuring plasma rotation profiles without injecting momentum (as with beam based diagnostics), C-Mod has pioneered studies of self-generated equilibrium flows.[204,205] Strong co-current rotation, with toroidal velocities up to 130 km/s (about 0.3 times the sound speed), has been observed and is strongest in enhanced confinement plasmas, i.e., the H- and I-mode. Under otherwise similar condition, the rotation state is independent of whether the plasma is heated with ICRF power or Ohmically, suggesting that the underlying mechanism is independent of the specific heating method.[206,207] As seen in Fig. 40, the core rotation velocity scales in proportion to the global plasma energy (or pressure) divided by the plasma current, that is, generally increasing with input power, but is significantly higher in the H-mode than in the L-mode for the same power.[205,208,209] Subsequent analysis of a multi-machine database found that the rotation could be characterized as a toroidal Mach number vs β_N.[209,210] By following the evolution of the profiles, it was shown that the intrinsic rotation originates at the plasma edge and propagates into
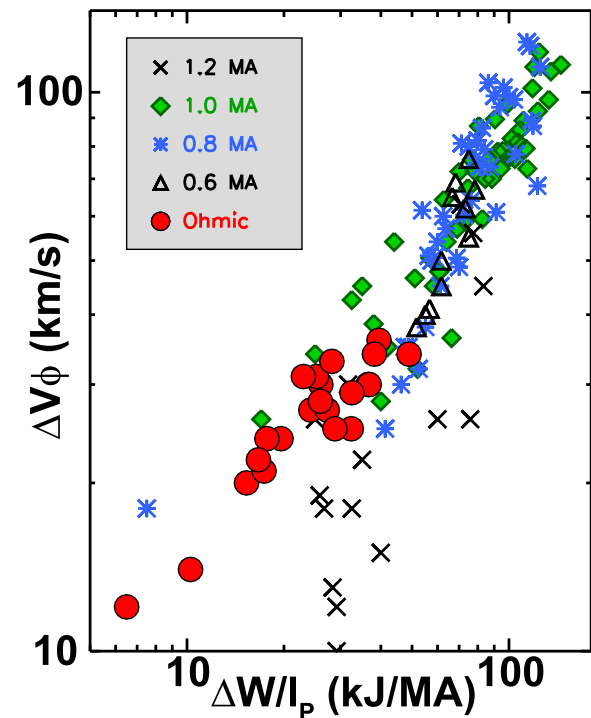

FIG. 40. Intrinsic rotation scales with stored energy divided by the plasma current and is independent of the heating method. Reprinted with permission from Rice *et al.*, Nuclear Fusion **41**, 277 (2001). Copyright 2001 IOP.[251]

the core.[211,212] Core rotation in the H-mode is strongly coupled to the pedestal temperature gradient for both the H-modes and I-modes, as seen in Fig. 41. This dependence is consistent with the model that this rotation is driven by residual stress, that is, the part of momentum flux which is not proportional to the flow velocity or its gradient.[213] The
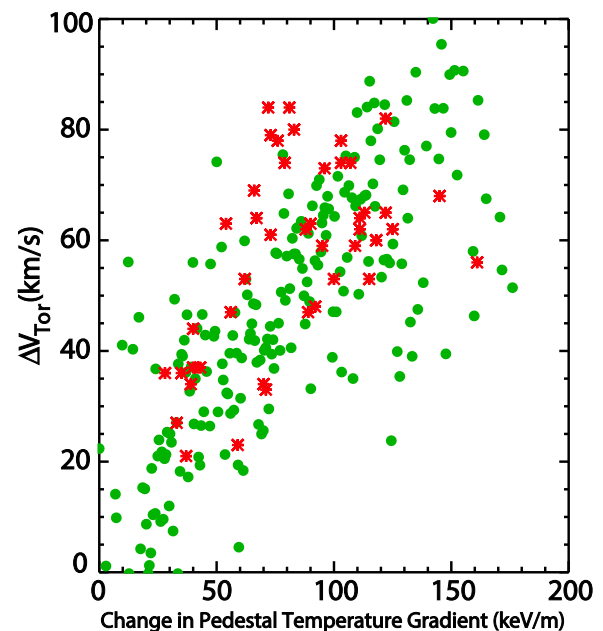

FIG. 41. Intrinsic toroidal rotation is proportional to the pedestal temperature gradient for both H-modes (green) and I-modes (red), consistent with the model that this rotation is driven by residual stress. Rice *et al.*, Phys. Rev. Lett. **106**, 265001 (2011). Copyright 2011 American Physical Society.[213]
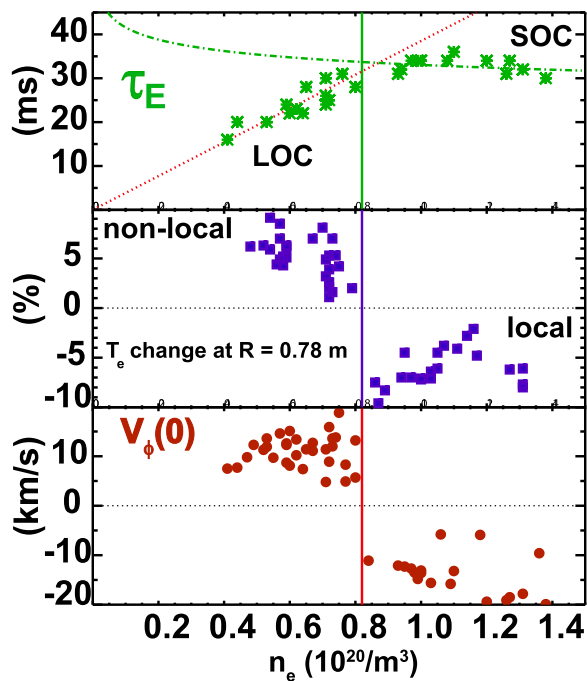
FIG. 42. Reversal of intrinsic rotation occurs dramatically at a q-dependent, critical density. The transition from LOC-SOC confinement and from non-local to local transient transport occur at the same density. Reprinted with permission from Rice *et al.*, Nuclear Fusion **53**, 033004 (2013). Copyright 2013 IOP.[225]

$E \times B$ shearing rate of intrinsic rotation is apparently large enough to effect transport through well-known turbulence stabilization mechanisms[214,215] and is thought to play a role in the formation of internal transport barriers (ITB) in C-Mod[216,217] as described in Sec. V D.

In Ohmic plasmas, the intrinsic rotation has a complicated dependence on collisionality, plasma current, and geometry.[218] A substantial counter-current rotation, up to -60 km/s, has been observed in some discharges with unfavorable ∇B drift. As noted in Sec. IV, this observation is connected to the H-mode power threshold.[148] Core rotation reversals, abrupt changes of the toroidal rotation direction, have been observed to occur at a q-dependent, critical value of the collisionality.[219] The reversals, seen in Fig. 42, can be induced with slight changes in the electron density, plasma current, or toroidal magnetic field, and are often accompanied by abrupt changes in turbulence characteristics[220,221] and also, unexpectedly, are associated with the transition from the linear Ohmic confinement (LOC) to the saturated Ohmic confinement (SOC) regimes.[222,223] This confinement transition is generally attributed to a transition from an electron-transport to ion-dominated turbulent transport.[224] The SOC seems in most respects to be identical to the ITG (ion thermal gradient) dominated L-mode while in the LOC, an electron transport channel opens up as the density is lowered and causes energy confinement to drop precipitously.

Other seemingly unrelated changes occur at the same critical collisionality. The non-local heat transport, core toroidal rotation reversals, energy confinement saturation, and up/down impurity density asymmetry are correlated with each other experimentally. That is, at low densities in the linear Ohmic confinement regime, with collisionality $\nu_* \leq 0.35$ (evaluated inside of the $q = 3/2$ surface), heat transport exhibits non-local behavior, core toroidal rotation is directed co-current, edge impurity density profiles are up/down symmetric, and a turbulent feature in line-integrated core density fluctuations with k_θ up to $15\,\mathrm{cm}^{-1}$ ($k_\theta \rho_s \sim 1$) is present. At high density/collisionality with saturated ohmic confinement, the electron thermal transport is diffusive, the core rotation is in the counter-current direction, the edge impurity density profiles are up/down asymmetric, and the high k_θ turbulent feature is absent. The rotation reversal stagnation point (just inside of the $q = 3/2$ surface) coincides with the non-local electron temperature profile inversion radius.[225,226] Rotation "reversals" have also been observed in discharges with the LH current drive (LHCD). For target plasmas with high plasma current, the intrinsic rotation experiences a change in the counter-current direction,[227,228] while for low plasma current targets, the rotation increment is in the co-current direction.[229,230] This reversal of the change in rotation with LHCD has been traced to the current density, through the q profile. At low collisionality, ICRF can also cause core rotation to decrease markedly and even reverse direction.[231]

C. Particle and impurity transport

Particle transport studies on C-Mod began with modulated gas puff experiments.[232] These experiments followed the response of the electron density profiles to periodic gas puffs using a singular-value decomposition analysis of interferometer chords. From the response, the profiles of transport coefficients, D (particle diffusivity) and V (convection velocity), were obtained. For the typical OH and L-mode plasmas, these two quantities increased monotonically with minor radius, reaching values on the order of 0.2 m^2/s and 1.5 m/s, respectively, at mid-radius. Particle transport was typically slower than energy transport with D/$\chi_i \sim 0.2$–1. For Ohmic LOC plasmas, both D and V decreased with density from 0.3 m^2/s and 3 m/s at $n_e = 7 \times 10^{19}$/m^2 to 0.07 m^2/s and 0.3 m/s at $n_e = 1.3 \times 10^{20}$/m^2 corresponding to stronger peaking at low density.

Turning to the H-mode, results from AUG and JET[40] showed moderate peaking at low collisionality, but could not distinguish between dependence on collisionality and n/n$_G$. (In these studies, a slightly modified form of collisionality, ν_{EFF}, is used.) This was critical for ITER since it uniquely would run simultaneously at a very low collisionality and high n/n$_G$. Depending on which of these normalizations for density was correct, this could imply either peaked or flat density profiles and thus rather different fusion yields and stability properties. Experiments were carried out on C-Mod to break this covariance. Moreover, by operating with ICRF only, it could verify the role of Neutral Beam Injection (NBI) fueling found in the earlier work. These experiments also featured strong electron heating, $T_i = T_e$, and a very weak neutral penetration—all ITER-like characteristics. In various parameter scans, the density peaking factors $n_e(0)/\langle n_e \rangle$ were clearly higher at low collisionality.[182] Figure 43 compares the C-Mod data with results from AUG and JET. It
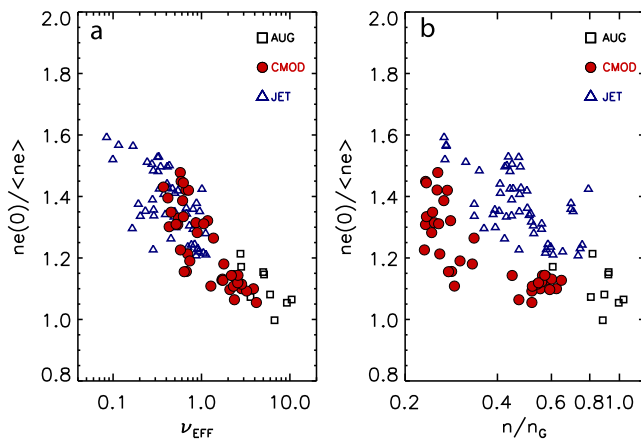
FIG. 43. Density peaking ratios in C-Mod is overlaid on data from AUG and JET showing that the appropriate scaling is collisionality (a) rather than n/n$_G$ (b) thus implying a moderate level of peaking for ITER baseline discharges. Reprinted with permission from Greenwald *et al.*, Nuclear Fusion **47**, L26 (2007). Copyright 2007 IOP.[182]

is clear that the overlay is better when the peaking is plotted vs ν_{EFF} than with n/n$_G$. The C-Mod results, without a core particle source, demonstrate that the main effect is via transport rather than fueling locations and strongly support the notion that ITER will operate with mildly peaked density profiles; n$_e$(0)/$\langle$n$_e\rangle$ may be up to 1.5. Gyrokinetic modeling was carried out for these discharges, by adjusting density profiles to match a zero particle flux condition, which is required for equilibrium.[233] The dependence on collisionality was recovered in these simulations, with shorter wavelength fluctuations (k$_\theta\rho_s > 0.5$) responsible for much of the difference in particle transport. The key to the pinch seems to be a reduction in the ITG drive, which may not be applicable in ITER. Overall, this work is consistent with the recent models of particle transport that depend on the interplay of ITG and Trapped Electron Mode (TEM) drift wave turbulence.[234]

Early studies of impurity particle transport used a ruby LBO system to inject trace amounts of non-intrinsic, non-recycling impurities, observing various impurity charge states with a wide range of spectroscopic diagnostics.[207,235,236] The LBO system effectively provides a delta-function impurity source in space and time. The subsequent evolution of spectral line brightness is then analyzed to obtain impurity transport properties. Impurity confinement times, τ_Z, in the L-mode were on the same order as the energy confinement time, that is, 0.020–0.030 s. In EDA H-modes, τ_Z is on the order of 0.1–0.2 s (see Fig. 30) somewhat longer than τ_E. In ELM-free H-modes, impurities tend to accumulate, with a confinement time long compared to the discharge length. Using the MIST impurity transport code,[237] impurity diffusion, D$_Z$, and convection, V$_Z$ coefficients consistent with the evolution of spectral brightness were obtained. In the core of both the L-mode and EDA H-modes, the transport coefficients are well above the levels predicted by neoclassical theory. However, in the vicinity of the H-mode transport barrier, D$_Z$ and V$_Z$ are significantly smaller, approaching neoclassical levels. Studies of soft x-ray emission from the pedestals of H-modes found a strong inward convection of impurities in the pedestal.[207,238,239] This pinch velocity was

larger for ELM-free H-modes and led to extremely sharp profiles of impurity density in the pedestal, consistent with neoclassical predictions. These early studies also investigated poloidal asymmetries in impurity transport. More recently, new insights on the poloidal variation of plasma parameters in the pedestal region of C-Mod have been obtained with Charge eXchange Recombination Spectroscopy (CXRS) measurements from both the HFS and LFS midplane. This reveals large ($>6\times$) in-out impurity density asymmetries in the H-mode and nearly symmetric impurity density profiles between the HFS and LFS pedestals in the I-mode.[240] Furthermore, the HFS and LFS measurements in the I- and H-mode show that potential and impurity temperature cannot both be flux functions in the pedestal.[180] These results are currently being investigated with numerical models and in particular support the idea that two-dimensional transport effects need to be retained in impurity modeling of the pedestal region.

A newer LBO system,[181] employing a multi-pulse YAG laser, was paired with the XICS diagnostic to measure, for the first time, the full profile evolution of a particular impurity charge state, in this case Ca^{+17}, following injection. Transport coefficients were derived by using the STRAHL code,[241] which simulates impurity transport and atomic physics, fitted with a synthetic diagnostic to replicate the XICS and VUV (vacuum ultraviolet) measurements.[242,243] These calculations were performed inside of an iteration loop that varied the D$_Z$ and V$_Z$ profiles and minimized the difference between the synthetic measurements and those obtained on the experiment. Uncertainties in the transport coefficients were calculated from the sensitivity of the calculation to input parameters (mainly, T$_e$ and n$_e$) and the spectroscopic measurement uncertainties. This approach was a
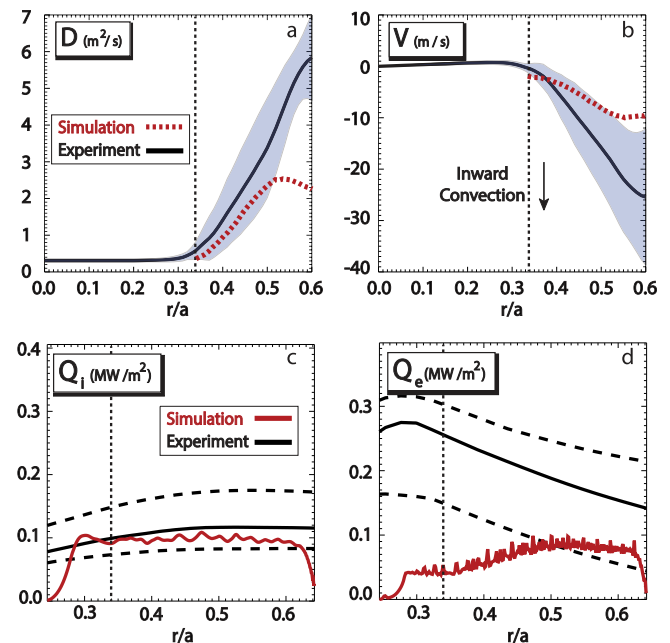

FIG. 44. Profiles of impurity transport coefficients, D$_Z$ (a) V$_Z$ (b), are obtained from impurity injection experiments. These are compared to gyrokinetic simulations, which can simultaneously match the ion energy (c) and impurity particle transport within experimental uncertainties. Electron energy transport is under-predicted in these simulations (d). Reproduced with permission from Phys. Plasmas **19**, 056110 (2012). Copyright 2012 AIP Publishing LLC.[268]

significant improvement on the "guess and test" method typically applied to this problem, and the realistic error estimates allowed for meaningful comparisons with theoretical models for the first time. With the temperature dependence of the charge state density and emission under observation, good estimates of transport were obtained for r/a < 0.6. Inside of r/a of 0.3, little turbulent transport was calculated, but instead impurity transport seemed to be governed by the MHD activity of the sawtooth instability. In the L-modes, in the region dominated by turbulence, D_Z profiles were well above neoclassical levels and far from constant, increasing sharply from the inversion radius and reaching values on the order of 5–6 m^2/s by r/a = 0.6 (see Fig. 44). Similar profile shapes were calculated for V_Z.[244] Values of the peaking factor, RV_Z/D_Z were on the order of 3, similar to n_e profile for the L-modes. These data were then compared in detail to nonlinear multi-channel gyrokinetic simulations, the results of which are discussed below in Sec. V E 2.

D. Studies of internal transport barriers

ITBs are important tools to raise overall performance and in particular to achieve the high values of β_P necessary for high bootstrap current in steady-state regimes. Most research in this area has used strong NBI that drives rotation and high levels of E × B shear. The core particle source from the beams can also contribute to peaking density, which reduces ITG drive as does the higher ratio of T_i/T_e that is typically found in the beam heated plasmas. The traditional recipe for ITB formation often includes modification of the current profile and thus the magnetic shear by strong heating during the current ramp-up.[245,246] On C-Mod, as in reactors, strong NBI heating is not available, and current relaxation is relatively fast compared to the discharge time. This prompts a search for actuators that will extrapolate into the reactor regime.[247]

In C-Mod, the ITBs have been produced in several ways:[248]

(1) In OH and ICRF heated plasmas with deuterium or lithium pellet injection, the core fueling creates peaked density profiles and suppresses transport, likely by stabilizing ITG turbulence, which is sensitive to the gradient scale length ratio $\eta \equiv L_n/L_T$.[15,249] The decrease in turbulent transport helps maintain the peaked density profile and sustain the regime.

(2) At many H-L transitions, a transient enhancement in central ion temperature and neutron production is seen. At the transition, the loss of H-mode particle confinement causes the edge density to drop quickly, but the core density remains at H-mode levels.[250] A possible explanation is that the transient increase in density gradient that follows from the drop in edge density, suppresses ITG turbulence via the same mechanism at work in pellet fueled discharges. This regime is transient and destroyed after a few sawteeth periods.

(3) Internal transport barriers also arise spontaneously in Ohmic H-modes.[250,251] If the mode can be maintained, the density profile slowly peaks, the sawteeth period
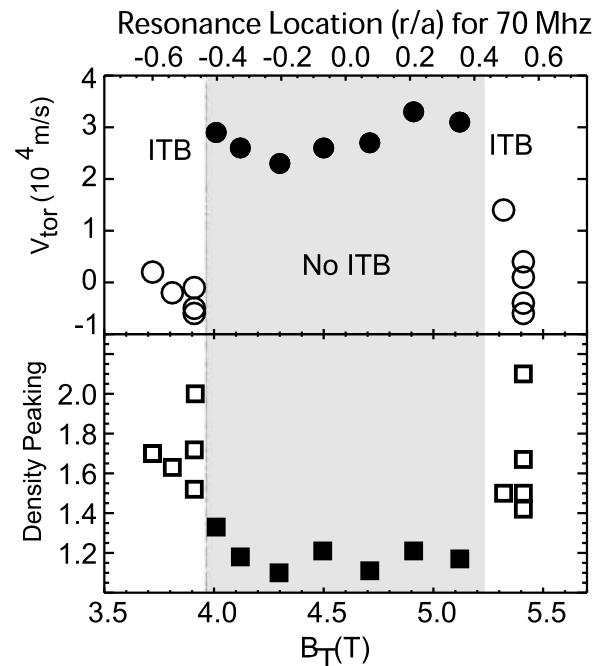

FIG. 45. ITB formation, as indicated by changes in the density profile and intrinsic rotation, depends critically on the ICRF resonance location as seen in this scan of B_T. Reprinted with permission from Fiore *et al.*, Fusion Sci. Tech. **51**, 303 (2007). Copyright 2007 American Nuclear Society.[248]

lengthens, and the sawteeth often cease entirely. (A modification in the q profile is also seen in pellet fueled discharges and attributed to peaking of light impurities.[252]) This regime can last up to 10 energy confinement times, often until current ramp-down. The mechanism is not understood.

(4) The principal tool for creating ITBs in C-Mod is off-axis ICRF heating.[202,250,251,253–255] These barriers form in sawtoothing H-mode discharges (that is, with monotonic q profiles and $q_{min} < 1$) without beam-driven rotation, without a core particle source and with $T_i = T_e$. This regime can be made stationary by application of modest on-axis heating. The remainder of this section will describe this regime.

In this last and most common ITB scenario, the ICRF resonance must be moved well off the magnetic axis, accomplished by changing the magnetic field or the ICRF frequency or both. Figure 45 shows the critical dependence of barrier formation on resonance location via a magnetic field scan for ICRF frequency fixed at 70 MHz. The most obvious sign of ITB formation is strong density peaking, which develops slowly—on a time scale consistent with the Ware pinch.[256] Starting with flat, H-mode like densities, in the range of 2.5–4 × 10^{20} m^{-3}, the central density will peak to values above 6 × 10^{20} m^{-3}. The profiles outside of the barrier foot remain at their H-mode level and shape. The temperature peaking inside the barrier is modest, but the overall pressure peaking is pronounced with analysis showing strongly suppressed thermal diffusivity inside the barrier foot. Thermal diffusivity can drop to ion-neoclassical levels inside a fully developed barrier.[255] The barrier foot location
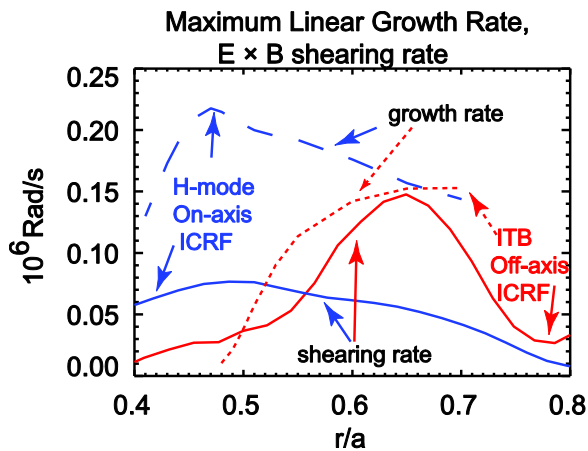
FIG. 46. The E × B shearing rate from intrinsic rotation can reach the ITG growth rate for discharges with off-axis ICRF that transition to an ITB. In similar H-mode discharges, with on-axis heating, the E × B rate is far below the growth rate. Reproduced with permission from Phys. Plasmas **19**, 056113 (2012). Copyright 2012 AIP Publishing LLC.[217]

is itself a function of the safety factor, with a location at r/a = 0.5 at $q_{95} = 3$ moving in to r/a = 0.25 at $q_{95} = 7$.

These C-Mod experiments provided the first evidence that intrinsic equilibrium toroidal rotation can generate sufficient E × B shearing to influence the formation of an internal transport barrier.[216,217,257] Creation of the ITB seems to require two essential elements. First, the off-axis heating reduces the temperature profile gradient, and thus the drive for ITG instabilities.[256,258] However, by itself, this mechanism is not strong enough to suppress the instability and account for barrier formation. The second ingredient, E × B stabilization, arises because of changes in the rotation profile that occur when the RF heating resonance is positioned off-axis. The rotation decreases in the center of the plasma while remaining unchanged in the outer part of the discharge, forming a well in the inner half-radius.[216,217,251] The result is a radial toroidal rotation profile with strong E × B shear ($>1.5 \times 10^5$ rad/s) in the region where the ITB foot is observed. Linear and nonlinear gyrokinetic analyses indicate that this spontaneous shearing rate is comparable to the linear ion temperature gradient (ITG) growth rate at this location and that the shearing rate is sufficient to reduce the turbulent particle and energy transport. Figure 46 shows the linear growth rate and E × B shearing rate at the barrier foot location and demonstrates the clear difference in these quantities for discharges with off-axis compared to central heating.

A dramatic illustration of barrier physics is the propagation of heat-pulses from sawteeth. The propagation is fast in core, then slow through barrier, then fast again outside the barrier.[202] This observation suggests that the turbulence drive at the barrier itself is well below the nonlinear critical gradient, i.e., well below marginality with turbulent transport entirely suppressed. Away from the barrier foot, both inside the barrier region and outside, the plasma is apparently above the marginal stability point ($\chi_{incremental} \gg \chi_{power\,balance}$). Overall, the picture is that in ITB discharges, turbulent transport is strongly reduced in the plasma core, entirely suppressed in the narrow barrier region and unchanged outside the barrier region.

The reduction in turbulent transport in ITB discharges can lead to density and impurity accumulation, leading to excess radiation, a sharp reduction in conducted power, and loss of the barrier. However, by adding a small level of on-axis heating, the peaking and impurity accumulation can be controlled.[253,255,256,259,260] The mechanism seems to be through the stimulation of TEM instabilities driven by the steep density gradient.[256] The growth rate of transport due to density gradient driven turbulence in this regime increases strongly with T_e, which responds to the heating. The simulation work behind this interpretation is discussed in Sec. V E 2.

E. Multi-channel transport validation studies

Over the time period covered in this review of C-Mod research, there has been a dramatic change in the role of computer simulations in turbulence studies. New theory, better computational algorithms, and faster computers have allowed the development of models sufficiently rich in physics to be reasonably compared to experimental measurements. At the same time, improvements in profile and fluctuation diagnostics have widened the scope of those comparisons. Broadly based in the national and international fusion programs, the long-term aim of this work is to develop computationally tractable models that can produce predictions of plasma behavior sufficiently reliable to be used for design of future machines. It is worth noting that transport prediction for the ITER design was based almost entirely on empirical scaling. Before we can make the step from empirical to physics-based predictive models, they will need to be rigorously and systematically tested against experimental observation. Fusion plasma research has begun adopting code verification, validation, and uncertainty quantification methods that were developed originally for computational fluid dynamics.[261–263] This should be understood as an extension of the scientific method into a research domain where advanced simulations are required to compute the implications of theory. The work has tended to focus on turbulent transport because (1) nonlinear behavior is critical to the predictions but requires difficult computations and (2) a good physical model is available. Anomalous transport in the plasma core is thought to be due to electrostatic drift-wave turbulence and well described by gyrokinetic theory, obeying the ordering required for the validity of that theory.

1. Simulations of ion and electron energy transport

The first nonlinear simulations of C-Mod discharges were motivated by discrepancies in the predictions of two widely used quasi-linear models. Though well-tested on data from other devices, the IFS-PPPL[199] and Multi-mode[264] models systematically and significantly under-predicted the core temperature gradients that were observed on C-Mod. This result suggested that the codes were not correctly calculating the nonlinear upshift[265] in the critical temperature gradient. Nonlinear simulations using the GS2 code[200,266] studied the parametric dependence of the upshift and found that proper treatment of zonal flow growth and damping required a calculation with kinetic (rather than adiabatic) electron dynamics and realistic collisionality. With these
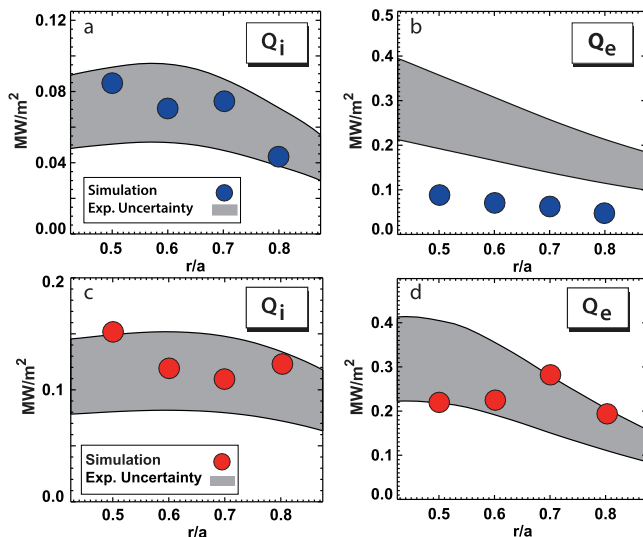
FIG. 47. Experimental ion and electron heat fluxes are shown for low-power (blue— (a), (b)) and high-power (red—(c), (d)) L-modes. The ion transport matches ion-scale gyrokinetic simulations at all radii, not showing the "shortfall" reported on DIII-D. At high powers, TEM instabilities in the simulation are excited and can explain electron heat transport. A discrepancy remains in the low-power case. Reproduced with permission from Phys. Plasmas **20**, 032510 (2013). Copyright 2013 AIP Publishing LLC.[269]
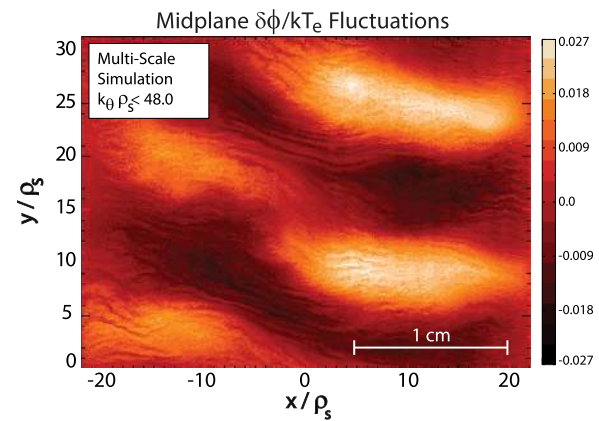

FIG. 48. Multi-scale gyrokinetic simulations, which include both electron and ion-scale dynamics show that fine scale ETG streamers can coexist with larger ITG structures and produce electron heat flux consistent with experiments.

features, the model was found to be consistent with experimental fluxes and gradients, within uncertainties.

Further simulations of ion energy transport[267–269] using the GYRO code[270] found agreement with experiments over a wider range of discharges, even under conditions similar to those where a so-called "transport shortfall" has been reported in DIII-D L-mode plasmas. In those cases, the ion and electron heat fluxes and turbulence levels in DIII-D were significantly under-predicted in the outer part of the plasma core by nonlinear gyrokinetic calculations using the GEM and GYRO codes.[271,272] In contrast, the simulations of C-Mod experiments predicted ion energy transport consistent with experimental data at the corresponding radial locations. Further, in a power scan, the electron energy transport was correctly predicted at higher powers, leaving a discrepancy only at lower powers and only in the electron channel.[269] A comparison of the predicted and measured heat fluxes for these discharges is shown in Fig. 47.

More generally, understanding anomalous electron thermal transport has proven to be a daunting and unmet challenge.[273] Recent multi-scale simulations suggest that ETG (Electron Thermal Gradient) turbulence plays an important role in electron thermal transport in C-Mod.[274] These simulations, using the GYRO code included both electron and ion gyrokinetic dynamics, using the actual ion-electron mass ratio and realistic plasma profiles—that is, they were near marginal stability.[275] The interplay between fluctuations at different scales was crucial in these simulations, with short wavelength fluctuations downshifted from the peak of their linear growth rate. An important feature of ETG turbulence is radially extended structures, called streamers, which have been seen in previous simulations of electron-scale turbulence.[193] Without the streamers, the radial scale of fluctuations would be far too small to drive transport at the levels

seen in experiments. It had been believed that strong, long wavelength turbulence would destroy the streamers reducing the predicted transport rates.[273] However, crucially in the multi-scale simulations reported here, the streamers can coexist with ion-scale eddies (as seen in Fig. 48, which plots the potential fluctuations from the simulation) and the levels of both the ion and electron energy transport predicted are close to the measured values.

Another approach has been to address the electron transport in the least complicated case possible, with a series of experiments and modeling activities focused on low-density Ohmic plasmas. In this regime, all input power is into electrons through the resistive dissipation of plasma current and coupling to ions is weak. Energy confinement, in this Alcator or LOC regime, is proportional to plasma density—thus, we must conclude that electron thermal transport increases substantially at low densities. Studies of these discharges included GYRO simulations and a synthetic diagnostic for the PCI diagnostic, which was capable of measuring density fluctuations with wave numbers up to $55\,cm^{-1}$.[276] Overall, the intensity of density fluctuations increases with density and a higher frequency, higher k feature (k_θ up to $15\,cm^{-1}$, $k_\theta\rho_s\sim1$) is present in the LOC regime but not the SOC.[223,225,277] In the SOC regime, the simulated ion and electron thermal diffusivities agree with experiments after varying the ion temperature gradient within experimental uncertainty. The absolute fluctuation intensity agrees with the simulation within experimental error ($\pm60\%$). However, in LOC, the model substantially over-predicts the ion transport and under-predicts the electron transport. This work has since been extended to include the role of ion dilution on the ITG drive[278] which reduces the ion density and the computed ion energy transport. This effect had previously been reported in low-density discharges.[279,280] This approach does not explain the discrepancy in the electron channel.

In the first measurements of long wavelength ($k_y\rho_s<0.3$) electron temperature fluctuations in Alcator C-Mod made with a new correlation electron cyclotron emission diagnostic[281] electron temperature fluctuations decrease
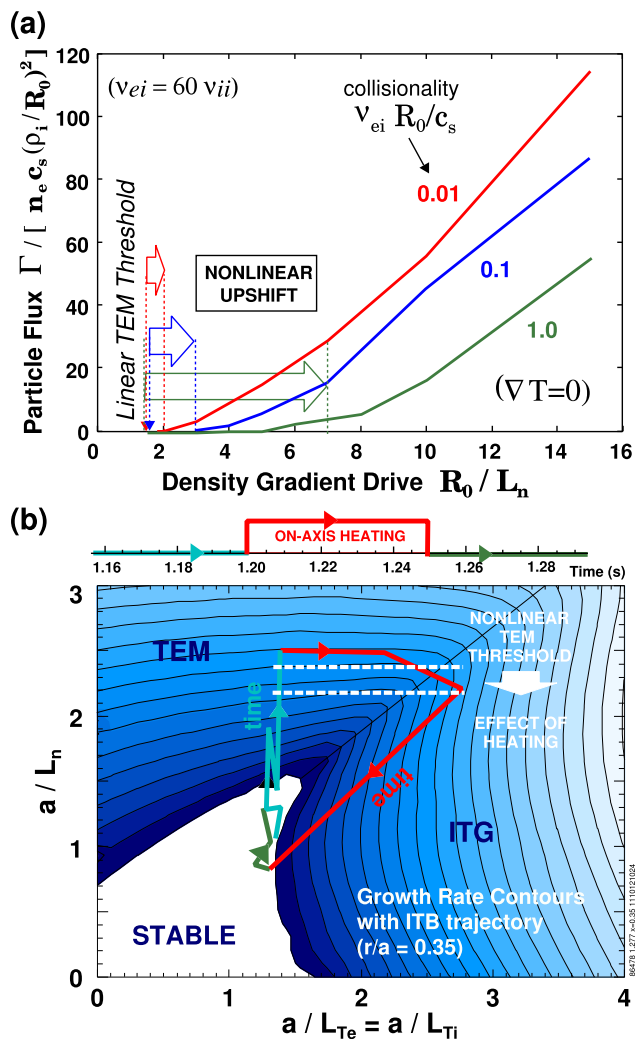
(a)

(b)

FIG. 49. A nonlinear upshift in density-gradient driven TEM was discovered in simulations of C-Mod ITB discharges. The upshift increases at higher collisionality providing a mechanism for transport control within the barrier.
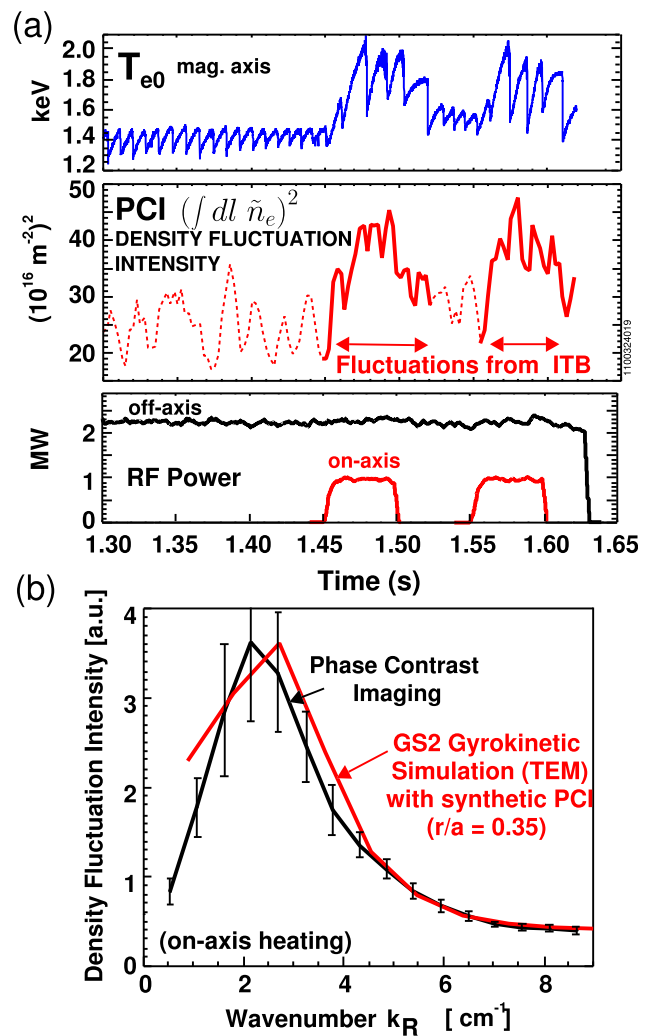
(a)

(b)

FIG. 50. Modulated on-axis heating in ITB discharges allows measured fluctuations to be localized within the barrier and supports the theory of barrier control via density gradient driven TEMs.

significantly ($\sim$40%) crossing from LOC to SOC, consistent with a change from TEM turbulence domination to ion temperature gradient (ITG) turbulence as the density and collisionality is increased.[221] Linear stability analysis shows that TEMs are dominant for long wavelength turbulence in the LOC regime and the ITG modes are dominant in the SOC regime at the radial location ($\rho \sim 0.8$) where the changes in electron temperature fluctuations are measured. In contrast, deeper in the core ($\rho < 0.8$), linear stability analysis indicates that ITG modes remain dominant across the LOC/SOC transition. This radial variation suggests that the robust global changes in confinement of energy and momentum occurring across the LOC/SOC transition are correlated to local changes in the dominant turbulent mode near the edge, which coincides with very minor changes in collisionality locally in that edge region.

2. Simulations of particle transport

Gyrokinetic simulations were used in studies of particle transport in ITB discharges. With off-axis heating only, core turbulence and transport are greatly reduced and the Ware

pinch is sufficient to account for the rate of density peaking. The density peaks sufficiently destabilize TEMs (before radiation leads to a back-transition).[256,260] A synthetic PCI diagnostic was developed to compare with GS2 simulations, resulting in the first direct comparison between measured fluctuation spectra and gyrokinetic simulations and finding a good agreement with the spectrum and the increase in amplitude of measured fluctuations.[260] The particle and energy fluxes also match transport analysis within uncertainties. Later simulations found, for the first time, a strong nonlinear upshift (illustrated in Fig. 49(a)) in the critical gradient for the density gradient driven TEMs, analogous to the effect of the Dimits shift on the temperature gradient and similarly associated with turbulent energy transfer into zonal flows.[282] The predicted upshift is much weaker at low collisionalities and thus is sensitive to temperature and can be modified by heating. In fact, as noted above, modest levels of on-axis heating were sufficient to control the peaking of the ITB density profiles and produce a steady state. Experimentally, the density gradient is found to be limited by the predicted nonlinear gradient, well above the linear calculation, and can be reduced with an increase in heating as seen in Fig. 49(b).
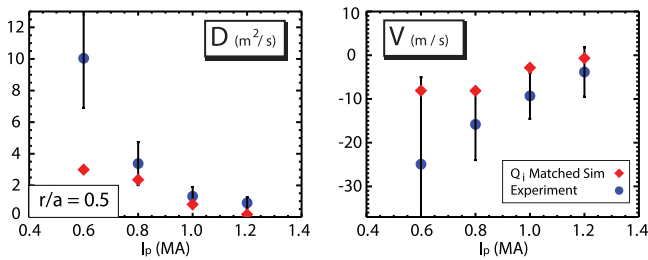
FIG. 51. Impurity transport coefficients, Dz, Vz, from an Ip are compared to gyrokinetic simulations which match the values and trends found in the experiments. Reproduced with permission from Phys. Plasmas **19**, 056110 (2012). Copyright 2012 AIP Publishing LLC.[268]

Figure 50 shows the results of modulated heating experiments that helped localize the induced turbulence to inside the transport barrier and to demonstrate the response of the turbulence to localized heating consistent with the theory.

Simultaneous comparison of impurity particle transport and energy transport were carried out between GYRO simulations and LBO experiments.[268] In these L-mode experiments, it was possible, for the first time, to match the ion energy transport and the profiles of both the impurity diffusion, D_Z, and inward convection, V_Z, as shown in Fig. 44. An extensive set of sensitivity studies were carried out for both the linear and nonlinear calculations in order to propagate the uncertainties from experimental profiles, which are inputs for the code, into the nonlinear turbulence calculation.[243] These studies also looked at the roughly linear dependence of impurity confinement time on plasma current, finding a corresponding decrease in both D_Z, and V_Z. The simulations were able to match the trend and the values of these transport coefficients as shown in Fig. 51. The effect is apparently from the change in magnetic shear that accompanies the change in edge safety factor. The discharges are dominated by ITG turbulence but TEMs are beginning to go unstable at lower values of I_P. In these simulations, it was not possible to simultaneously match the electron energy transport, likely due to the lack of high-k dynamics in the simulations and that is currently being addressed in multiscale work as discussed in Sec. V E 1.

3. Momentum transport

Models for momentum transport, in the low flow regime, are only now emerging but it has been possible to test some general ideas about the origins of intrinsic rotation. These ideas focus on the role of "residual stress," Π^r, that is, the portion of the angular momentum flux that is not proportional to the velocity or to its gradient.[283,284] The divergence of the residual stress constitutes the intrinsic torque. In the enhanced confinement regimes, Π^r is a function of the temperature gradient. Π^r depends upon the underlying turbulence, and can change sign if the turbulence mode propagation changes direction. During some rotation reversals, induced through collisionality changes, the dominant drift-wave turbulence regime is close to the boundary between the two dominant long-wavelength drift waves the ITG-TEM. Π^r is also a function of the q profile, which is in

qualitative agreement with the rotation changes observed in the LHCD plasmas.

More recent experiments studying rotation reversal in the ICRF heated plasmas suggest that the situation is more complex.[231,285] In this experiment, designed for validating gyrokinetic models of the energy and particle transport, a base-case steady, sawtoothing L-mode plasma with 1.2 MW of on-axis RF heating was established. When the density was raised by 20%, it was found that the measured rotation profiles changed from peaked to hollow in shape while the electron density and impurity profiles remain peaked. Ion and electron heat fluxes in the two plasmas were the same. Direct quantitative comparisons with GYRO were carried out, and a good agreement with experimental ion heat flux, impurity particle transport, and trends in the fluctuation level ratio, $\tilde{n}_e/n_e$, $\tilde{T}_e/T_e$, was found though the electron heat flux was under-predicted.[269] However, the observed changes in momentum transport (rotation profiles changing from peaked to hollow) did not correlate with changes in particle transport, and also did not correlate with changes in linear mode dominance, i.e., ITG vs TEM. These new results suggest that the drive for momentum transport differs from drives for heat and particle transport, possibly entering the gyrokinetic model formulation at a higher order.[286]

VI. RESEARCH AT THE ION CYCLOTRON RANGE OF FREQUENCIES (ICRF)

From the start of C-Mod operation, ICRF was the principal auxiliary heating tool and underlies the entire research program. The need for routine operation of these systems at high power density (routinely up to 10 MW/m^2) in efficient heating scenarios motivated the development of robust and reliable engineering solutions and drove research into related physics and technology.[287,288] Using a set of innovative diagnostics, studies of wave coupling, propagation, absorption and mode conversion physics contributed to validation of emerging full-wave RF models for the first time. Engineering challenges had to be faced and solved by employing advanced design and analysis codes backed up by two decades of field testing. And while a tremendous amount has been learned about RF physics in the process, the importance of "everyday" use as a driver for technology development and a metric for performance cannot be overstated. The similarity of the C-Mod plasma density, magnetic field, and RF frequencies compared to ITER, as discussed in Sec. I, argues for the strong and immediate relevance of the results produced.

Using RF sources originally procured for the Fusion Materials Irradiation Test Facility, the C-Mod facility has available 8 MW of source power; 4 MW fixed at 80 MHz, and 4 MW tunable from 40 to 80 MHz. Power coupled into the plasma has been as high as 6 MW. The transmission network is carefully engineered to maximize the transmitted power, voltage handling, and impedance matching to the ICRF antennas.[289,290] A set of fast ferrite tuners has been deployed to improve the tolerance of the matching to changes in the plasma loading,[291,292] particularly in response to L-H transitions and ELMs. Five different antennas have

been built and tested in the machine, beginning with a simple monopole design and advancing through a pair of 2-strap dipole antennas, to a 4-strap, toroidally-aligned (TA) design, and finally to a 4-strap field-aligned version.[293–295] The design of the in-vessel RF feeds has also evolved based on modeling and testing aimed at reducing power limits imposed by high-voltage breakdown. Several types of protection circuitry have been implemented to prevent damage to the antennas, feeds, transmission line, and RF tubes. Three of these antennas can be seen in Fig. 3. The most common ICRF scenario employed has been hydrogen minority in deuterium majority plasmas, D(H), at 5.4 T, which puts the resonance on axis and provides highly efficient heating typically with 80%–90% of the coupled power absorbed in the core plasma.[293] Also tested were He^3 minority heating, $D(He^3)$ at 7.9 T, a variety of mode conversion scenarios and 2nd harmonic heating of H minority at 2.6 T.[294,296–301]

A. ICRF minority and mode conversion heating and experimental validation of full-wave codes

In ICRF heating, power is transmitted from the antenna through the plasma to an absorbing region as a compressional-Alfven wave (also called the fast magnetosonic wave). Absorption can be via cyclotron damping on minority ions or through electron Landau damping of the incoming fast wave or short-wavelength, mode converted waves. In a typical D(H) minority heating case, modeling suggests that 70% of absorbed power is coupled to a fast minority ion tail, 20% to majority ions, via second harmonic deuterium cyclotron damping, and 10% of power directly to electrons via Landau damping. Heating efficiency is optimum with a few percent minority concentration. Under these conditions, a strong minority ion tail develops. Since most of the minority ion tail slows down on electrons, overall heating power to electrons is about twice the power to ions. At higher minority fractions, the fast wave will mode-convert near the ion-ion hybrid resonance layer. With either regime, C-Mod is a dominantly electron heated device, though over much of its operating range, the ions and electrons are strongly coupled.

While the basic physics mechanism for ICRF heating is well established,[302,303] calculations that can model the full-wave propagation and damping, with proper treatment of kinetic wave-particle interactions and realistic geometry have become available only relatively recently. New algorithms written for efficient parallel computation were required, especially to model the shorter wavelength mode-conversion phenomena.[304,305] Confidence in these models must be earned through comparison with experiments, carefully testing the predictions of each of their constituent elements. The computation of wave propagation was tested for the first time in minority and mode-conversion regimes by direct measurements of plasma density perturbed by the wave fields in the plasma using the PCI diagnostic and comparing to the output of the TORIC[306] and AORSA[307] codes fitted with a matching synthetic diagnostic. In general, these experiments found agreement between the predictions and experiments, and featured the experimental
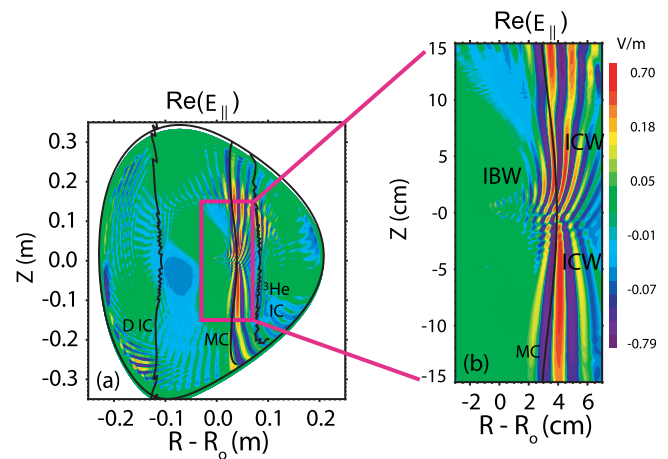

FIG. 52. TORIC simulations of ICRF propagation show the incoming fast wave, the anticipated, mode-converted, forward-propagating IBW and the re-discovered, backward propagating ICW. Lin *et al.*, Plasma Physics and Controlled Fusion **47**, 1207 (2005). Copyright 2005 International Atomic Energy Agency.[309]

discovery of an RF wave that had been predicted theoretically many years earlier[308] but never reported in experiments or codes. This ion cyclotron wave (ICW) originates in the mode conversion process, propagates back toward the low-field situated antenna, and has a wavelength intermediate between the launched fast wave and the more familiar IBW (Ion Bernstein Wave). All three types of ICRF waves, the fast wave, the IBW, and the ICW can be seen in Fig. 52.[309] Comparisons of the predicted and measured wave intensity, measured with PCI, are shown in Fig. 53(a).

A second set of predictions tested on C-Mod involves the fast ion distribution created in minority heating. Using a novel, multi-chord, compact neutral particle analyzer (CNPA)[310] to look at neutrals created by passive and active charge exchange reactions, proton energy spectra were obtained. These spectra were compared to simulations using the full-wave codes TORIC and AORSA coupled to the Fokker-Planck solvers FPPRF[311] and CQL3D[312] fitted with synthetic diagnostics to match the CNPA viewing geometry and sensitivity.[313] The measurements showed that the super-thermal ions were peaked off-axis due to incomplete wave focusing and preferential heating of trapped ions. This observation was consistent with measurements of local electron heating from observations of sawtooth reheat rates. The codes could reproduce the experimental features in steady-state with reasonable agreement, as seen in Fig. 53(b), and also reproduced the observed dependence of the fast proton spectra with I_P and P_{ICRF}.[314] However, the codes failed to predict the transient evolution of the spectra, finding a significantly slower build-up and decay when the RF was pulsed. This disagreement might be related to the finite banana width and gyro-orbit size of the ion tail or to non-diffusive effects of the RF on the distribution function.[315] Results from the ORBIT-RF[316] and DC[317] codes suggest that the wave-particle interactions modify the distribution function, causing it to evolve faster than expected from collisional processes alone. A computational approach was developed that uses
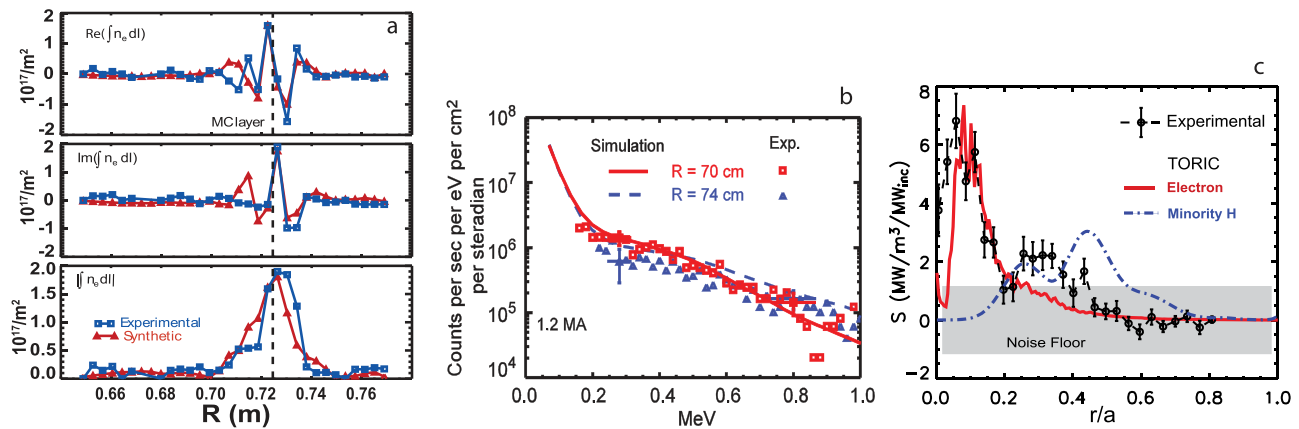
FIG. 53. (a) Mode-converted RF waves measured with phase-contrast imaging are compared to full-wave simulations. Lin *et al.*, Plasma Physics and Controlled Fusion **47**, 1207 (2005). Copyright 2005 International Atomic Energy Agency.[309] (b) The energy spectra of non-thermal ions are compared to AORSA simulations of minority heating. These simulations show agreement in the equilibrium distribution function as well as its dependence on plasma current and input power. Reproduced with permission from in *Proceedings of the 19th Topical Conference on Radio Frequency Power in Plasmas* (2011), Vol. 1406. Copyright 2011 AIP Publishing LLC.[341] (c) Experimental measurements of local heat deposition are compared to TORIC simulations of mode conversion heating. Lin *et al.*, Plasma Physics and Controlled Fusion **45**, 1013 (2003). Copyright 2003 International Atomic Energy Agency.[299]

the ICRF wave fields from the AORSA solver in DC. The DC code directly integrates the Lorentz force equation for ions using the full-wave fields and reconstructs an RF operator from a statistical ensemble of RF particle kicks in the wave field in order to capture non-diffusive effects. This RF operator is then used in CQL3D to evolve the non-thermal particle distribution. Preliminary application of this technique has greatly improved the agreement between the measured and simulated formation times of the energetic tail in C-Mod minority heating experiments.[315]

In the mode conversion regime, direct, localized heating of the electrons near the mode conversion layer is expected. This prediction was tested using modulated RF power and a break in slope analysis of the electron temperature profiles.[298,299,301,318] The simulations required proper treatment of electron Landau damping for short wavelength modes.[319] The predicted and measured profiles of mode conversion electron heating in a D(H) plasma can be seen in Fig. 53(c).[299] The predicted position and localization ($\Delta(r/a) \sim 0.2$) of the heating layer in D(He^3) plasmas was confirmed in the simulations as well as the dependence of heating efficiency on the He^3 content for fractions, n_{He3}/n_e, below 0.20. At higher fractions, the code initially under-predicted the measured heating, likely due to a lack of resolution in the poloidal mode expansion of the RF fields. This disagreement was addressed in later versions of TORIC with improved numerical algorithms and parallel execution that allowed much higher poloidal resolution.[304]

B. ICRF flow drive

Plasma rotation has been shown to be beneficial in stabilizing MHD modes[320] and improving confinement in experiments[215] with a strong external torque applied by the neutral beam heating systems. However, reactor scale devices like ITER or Demo will need to run with a low or zero applied torque, and it is not clear yet whether intrinsic rotation will be large enough to realize all of the desired effects. The

prospect of modifying plasma transport directly through $E \times B$ stabilization has motivated studies of plasma flow driven by RF waves.[321] ICRF codes have predicted that such flows could be driven by IBW; however, uncertainties in the physics of the plasma response to RF and in plasma momentum transport have led to corresponding uncertainty in the predictions.[322,323] On C-Mod, flow drive has been demonstrated for the first time in the mode conversion regime. In these experiments, plasma rotation was measured at levels well above those expected from the response of intrinsic rotation to the added heating.[324] Simulations with the TORIC code showed that the mechanism is through IC wave interaction with He^3 ions, while the shorter wavelength IBW only caused electron heating.[325] Figure 54 shows a comparison of two discharges with the same RF power, one with D(H) minority heating and the second in the D(He^3) mode
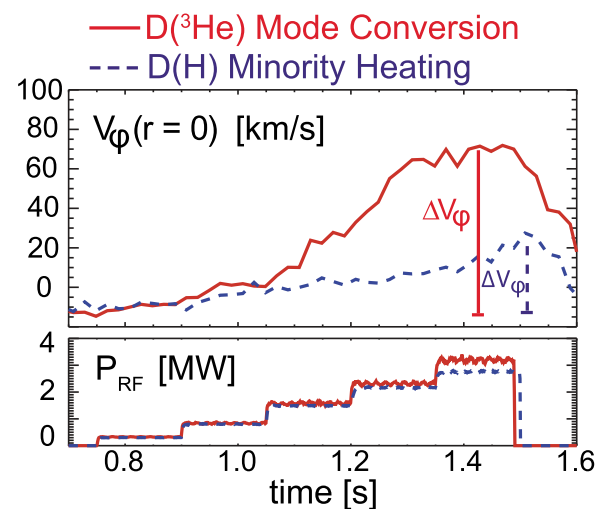

FIG. 54. ICRF flow drive is demonstrated in this comparison of minority heating (blue) with only intrinsic rotation (which is proportional to plasma energy) and mode-conversion heating (red). With equal power in each regime, significantly higher flow is produced in the mode conversion case. Reproduced with permission from Phys. Plasmas **16**, 056102 (2009). Copyright 2009 AIP Publishing LLC.[316]

conversion regime. Although the stored energy increase is somewhat larger for the minority heating case, the toroidal rotation is much greater for mode conversion. Driven rotation can exceed 100 km/s, which is on the order of 20% the sound speed. The $E \times B$ shearing rate of these flows approached the linear growth rate for ITG drift waves, the level at which strong effects on plasma transport are expected. So far, the limitation on driven rotation is connected with the stimulation of neoclassical tearing modes (NTM) due to low collisionality at the very high electron temperatures produced. A series of parameter scans allowed the derivation of an empirical scaling law for the driven rotation $\Delta V(km/s) \approx 10 P_{\mathrm{RF}}(\mathrm{MW})^{1.1} T_{e0}(keV)^{1.3} I_P(MA)^{0.4} n_{e0}$ $(10^{20}\,\mathrm{m}^{-3})^{-0.9}$.[326] Notable is the linear dependence on power per particle.

C. ICRF impurity generation and the field aligned antenna

The importance of controlling impurity sources in plasmas with strong ICRF heating has long been recognized.[327] This issue becomes particularly important when the antenna and other PFCs are made from reactor-compatible materials,- namely, high-Z metals. Early experiments on C-Mod confirmed these concerns, with performance degraded by impurity radiation in the H-mode discharges with untreated molybdenum PFCs.[17,328,329] Contributing to this effect is the improved impurity confinement in the H-mode and the sensitivity of the H-mode confinement to power conducted across the separatrix. High-Z impurities, which have their peak radiation at temperatures that prevail well into the plasma core, must be minimized for full performance. For example, tolerance to tungsten in a reactor would be no more than 10 parts per million. The molybdenum source rate was found to be proportional to RF power and originated mainly from the antenna protection tiles, with sources from the wall and divertor significantly less important.[43,330] As a palliative measure, the walls of the vacuum vessel were boronized,[331] that is, covered by a thin layer of boron by discharge cleaning
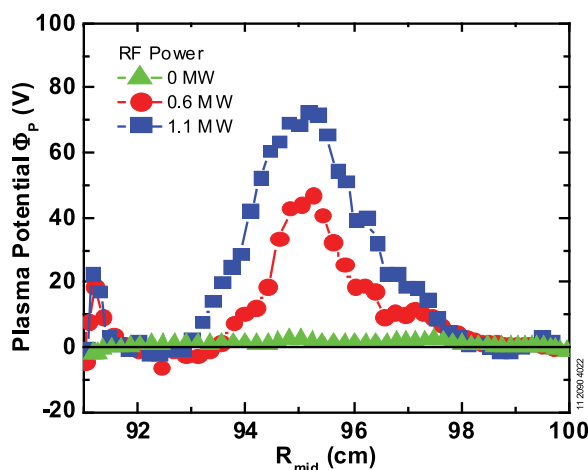

FIG. 55. Significant RF sheath potentials are measured with an amplitude proportional to input power. The acceleration of ions through this sheath and onto the first wall is believed to contribute to the increased impurity content of ICRF heating plasmas.

with deuterated diborane gas.[19] The boron layers on the order of 100 nm were sufficient to restore the H-mode confinement for several days of operation This approach is satisfactory for a short pulsed experiment, but is not extrapolatable to a steady-state reactor. To make further progress, it was necessary to understand the mechanism by which impurities were generated and transported into the plasma and to develop techniques to mitigate this problem.

Research into the impurity source has centered on the role of the RF sheath, an increase in the plasma potential on field lines that contact material surfaces and pass near the antenna or other locations with large wave energy density. The sheath is produced by rectification of the RF waves due to the difference between electron and ion mobility.[332,333] The resulting potential accelerates ions, increasing their sputtering yield when they impact a material surface. An indirect evidence for an RF specific mechanism is from boron film erosion rates, estimated to be in the range of 15–20 nm/s, consistent with the eroding species having an energy far above the thermal background.[330] Direct experimental evidence for the sheath mechanism was obtained with Langmuir probes, operated in a variety of modes, which measured plasma potentials of over 100 V, high enough to cause significant sputtering of molybdenum by D^+ ions.[334] The measured potentials increased with RF power and were lower when the walls were well boronized. These potentials, seen in Fig. 55, have a threshold dependent on the density in front of the antenna, consistent with theoretical predictions.[335] Rectified potentials were observed[336] and modeled[337] on surfaces not magnetically connected to the antenna. These RF-induced potentials were also inferred from the modification of the fluctuation phase velocity as measured with gas-puff imaging.[126,338] Interpreting the change in phase velocity profile as a change in the $E \times B$ flow yields an estimate for E_r in excess of 10 kV/m, consistent with the sheath potential measurement. In addition, the GPI measurements suggest that the modified potential structure could be influencing particle transport through the generation of large convective cells.

In order to reduce the magnitude of the RF sheath and control the level of impurities, an innovative antenna concept—the FA antenna—was developed.[339,340] The idea is to minimize the component of the RF electric field that is parallel to the tokamak magnetic field. Modeling showed that by symmetrizing the antenna and surrounding structures, $E_{\parallel}$ would be reduced, circumventing the RF sheath mechanism. The resulting antenna geometry is shown schematically in Fig. 56, with the antenna box, straps, and Faraday screens all aligned with the total magnetic field. This is a much more challenging engineering task than simply aligning the Faraday screens, as it requires design and fabrication of a helical structure that fits snugly against the wall of the axisymmetric toroidal vacuum vessel. Initial results have been promising, with the molybdenum source from the antenna lower by an order of magnitude, as seen in Fig. 57, along with an overall reduction in radiated power.[340] The electrical properties of the antenna are excellent. Power densities up to 9 MW/m² have been achieved; greater load tolerance and a very low RF power deposited in the antenna itself (0.4%),
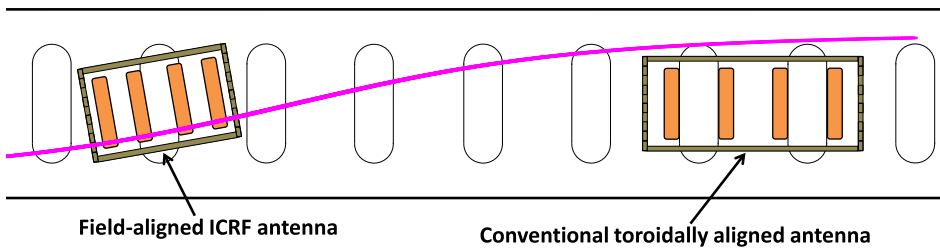
FIG. 56. The geometry of the traditional TA ICRF antenna is compared to the new FA design. A sample field line, which passes directly in front of the FA antenna is shown in purple.

which is below the requirement for the ITER antenna (0.625%). While successful in its ultimate aim—addressing the impurity issue—the results differed from expectations in important details. The observed changes in the induced potential and its dependence on antenna phasing do not match theory or models. In fact, the measured RF sheath induced by the FA antenna is similar to what is produced by the conventional TA antenna. Recent work has begun to explain the discrepancy. For example, the original model had suggested that monopole phasing would lead to an improvement with respect to impurity sources compared to a dipole, but the measured impurity response was worse. Measurements made of waves in plasma with PCI found poor wave coupling and penetration for monopole phasing— a difference apparently due to modification of the RF spectrum by structures surrounding the antenna straps. The overall conclusion is that the FA approach has a great promise for solving the impurity problem associated with ICRF, but much work remains to be done.

VII. LHCD

A future tokamak reactor will need efficient off-axis, non-inductive current drive to allow steady-state operation, even with substantial bootstrap current. Further, the driver technology must be viable in steady state and in the reactor's nuclear environment. LHCD is among the very few options available and has been well demonstrated at low to moderate densities.[342] Recent C-Mod experiments have extended these studies to reactor-relevant fields, density, RF, and magnetic geometry[343] and allowed tests of emerging LHCD models.[344] The principal question being addressed is whether

results from low density can be extended to the higher densities required for reactor level performance, particularly to the values of β_P required to provide sufficient bootstrap current for a steady-state scenario. Experiments to date have launched up to 1 MW of RF power at 4.6 GHz through a phased-array launcher. The launcher has 16 toroidal by 4 poloidal elements employing a novel design based on a four-way splitter, with one waveguide feed for each vertical column of antenna array. The design was developed with the aid of an advanced finite element code to model the RF fields and to account for the electromagnetic, thermal, and structural interactions.[345–347] The column-to-column phase delay can be adjusted electronically to launch waves with the high directivity required for current drive experiments. Experiments were typically run with the parallel refractive index, $n_\parallel$ in the range from 1.6 to 2.2, which should interact strongly with and accelerate electrons from a distribution whose initial temperature is on the order of 5 keV. Studies of LH coupling elucidated the role of the ponderomotive effect and E × B drifts through experiments and modeling. The LH waves can reduce the plasma density in front of the launcher by this mechanism.[346–348] ICRF waves from nearby antennas can have a similar effect, lowering the density and increasing reflections.[349]

A. High LH current drive efficiency observed at moderate densities

At moderate densities, up to $0.6 \times 10^{20}/\text{m}^3$, the LH system on C-Mod can drive 100% of the plasma current (0.5 MA) for multiple L/R times,[347,350,351] as seen in Fig. 58(a). With the plasma density, magnetic field, and RF frequency in these experiments, approximately what is projected for ITER "steady-state" scenarios, C-Mod provides a directly relevant test-bed for studies of current profile control, stability, and transport. Global current drive efficiency, $\eta = n_{20}RI_{LH}/P_{LH}$, is on the order of 0.25 (A/m²W), consistent with previous experiments, theoretical expectations, and the values assumed for ITER steady-state scenarios. The population of nonthermal electrons predicted by LH theory was measured with a multi-chord hard x-ray diagnostic and found to build up and decay at a rate consistent with coupled ray-tracing/Fokker-Planck models in response to pulses of LH power.[352,353] The same measurements showed that perpendicular transport of the fast electrons during the slowing down time was small compared to the device size, indicating that fast electrons stay near the flux surfaces on which they are generated. Measurements with a Motional Stark Effect (MSE) diagnostic, used to constrain a magnetic equilibrium reconstruction, have shown that the current can be driven well off-axis.[354–356] The current profile can be modified
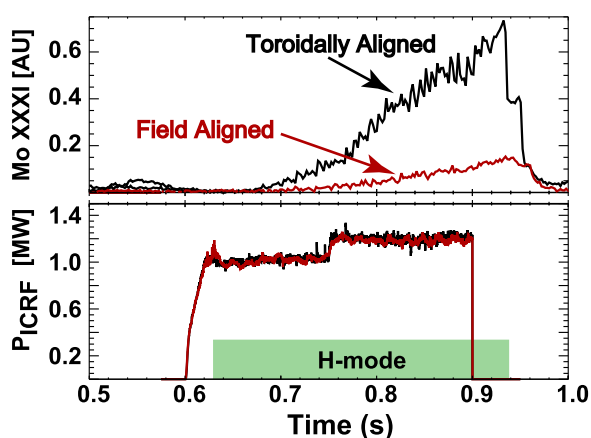

FIG. 57. The molybdenum source rate during ICRF heating drops by almost an order of magnitude in FA design. Reproduced with permission from Phys. Plasmas **20**, 056117 (2013). Copyright 2013 AIP Publishing LLC.[295]
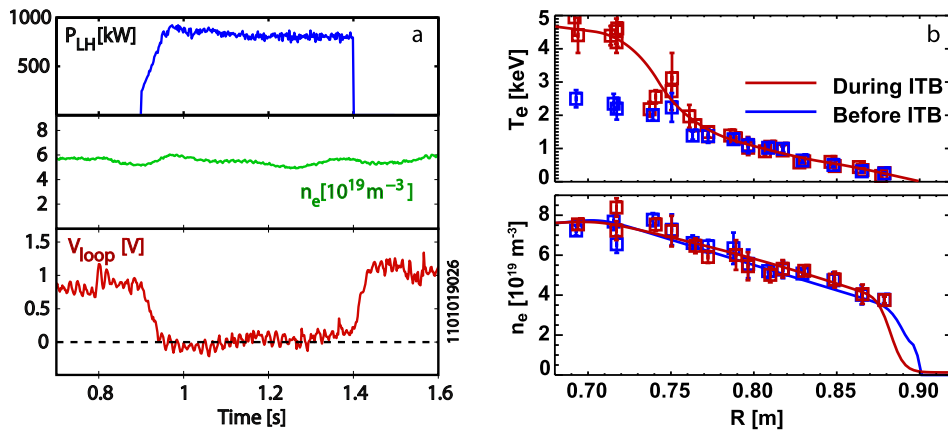
FIG. 58. (a) Efficient LHCD can produce fully non-inductive discharges at densities above 0.5×10^{20}. Reproduced with permission from Phys. Plasmas **19**, 062505 (2012). Copyright 2012 AIP Publishing LLC.[359] (b) Off axis-current drive can modify the magnetic shear and allow an electron ITB to form. Shiraiwa *et al.*, Nuclear Fusion **53**, 113028 (2013). Copyright 2013 International Atomic Energy Agency.[357]

sufficiently to create a sawtooth-free reversed shear regime.[357] In these plasmas, the change in q profile is accompanied by development of an electron energy transport barrier, leading to a sharp rise in the core temperature, as seen in Fig. 58(b). The barrier formation is likely attributable to the stabilization of drift wave turbulence in response to the change in magnetic shear. This regime is often curtailed by development of n = 2, m = 1 MHD activity.

B. Decrease of LHCD efficiency at high density

At high densities, $\bar{n}_e > 10^{20}/m^3$, but below the limit for wave accessibility, LHCD efficiency drops faster than expected.[358,359] Figure 59 compares experimental measurements of the hard x-rays produced by fast electrons and the prediction of a ray tracing calculation that neglects propagation and absorption processes in the plasma edge. The changes in the measured ionization rates and profiles in the SOL suggest that wave-plasma interactions in the edge are significant. These effects have been studied with ray tracing (GENRAY[360]) and full-wave (LHEAF,[345,361] TORLH[362]) RF simulations coupled to the Fokker-Planck models CQL3D and VERD.[346] LHEAF is a new code, developed by the C-Mod group, which uses finite element methods to compute wave coupling and propagation. The model computes

the RF fields as they propagate in the launcher, through the plasma edge and into the plasma, allowing better modeling of the interactions in the edge plasma. Several mechanisms have been identified so far—all connected to low single-pass absorption—including spectral broadening due to full-wave effects and plasma density fluctuations, nonlinear interactions such as parametric decay instabilities (PDIs), collisional damping, and loss of fast electrons in the plasma SOL.[358] Visible spectroscopy and imaging reveal local limiter heating and enhanced erosion in areas with magnetic field-line mapping to the LH antenna horns. Although direct scattering by edge fluctuations was found to modify the LH wave spectrum, it was not found to limit wave penetration.[363] Figure 60 is the predicted wave amplitude from a full-wave calculation for a high-density plasma, showing that a large fraction of the wave energy propagates in the plasma edge and SOL at high densities. The high wave
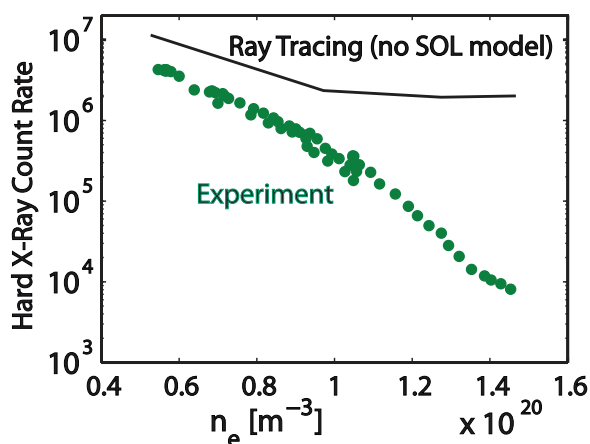

FIG. 59. At high densities, but below wave accessibility limits, driven current—indicated here by the decrease in hard x-rays—drops well below the expectations of a simple ray tracing model. Reproduced with permission from Phys. Plasmas **19**, 062505 (2012). Copyright 2012 AIP Publishing LLC.[359]
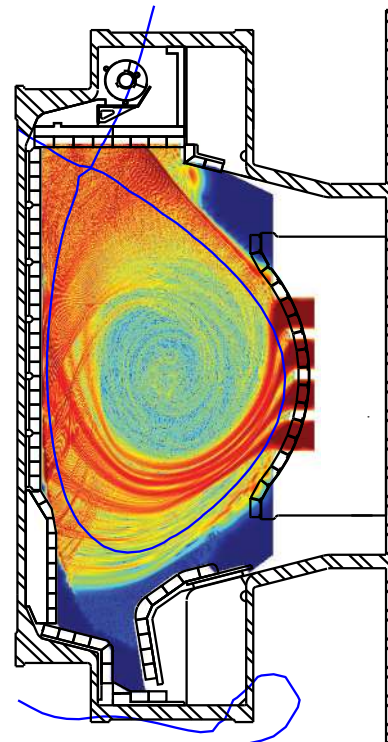

FIG. 60. A full-wave LH simulation at high density, showing waves propagating in the edge plasma.
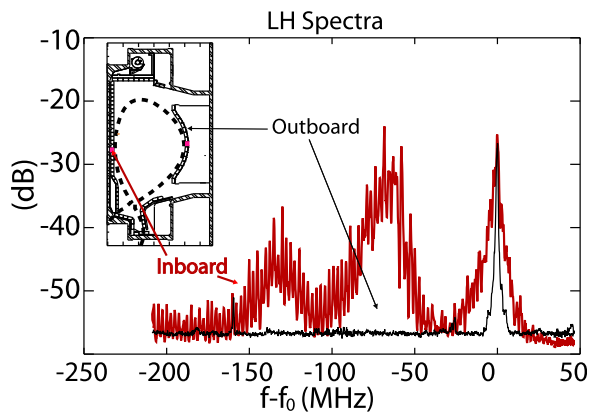
FIG. 61. Strong parametric decay is observed in measurements on the inboard (high-field) side of the machine but not on the outboard (low-field) side. This mechanism may contribute to a drop in LHCD efficiency at high density. Shiraiwa *et al.*, Nuclear Fusion **53**, 113028 (2013). Copyright 2013 International Atomic Energy Agency.[357]

amplitude, particularly in high-field SOL region of the plasma, can drive PDI, resulting in a loss of current drive by dramatically upshifting the $n_{\parallel}$ of the daughter waves. Fig. 61 shows evidence of PDI in measurements of the RF frequency spectra taken at the high-field side midplane with broadening of the drive frequency and strong sidebands separated from the pump wave by multiples of the local ion gyro-frequency.[364–366] Modeling suggests that weak absorption enhances the wave amplitude in the regions where local conditions allow the PDI to grow—consistent with a model by Takase,[367] though the quantitative role of PDI in reducing LHCD efficiency at a high density is not certain. Based on the modeling, running with higher single-pass damping (as in ITER) could mitigate all of the identified mechanisms and lead to a higher current drive efficiency. Experiments at higher plasma temperature, which increases the damping and reduces edge effects, do in fact demonstrate the LHCD recovery of LH driven electrons at densities near the accessibility limit (see Fig. 62). Based on these results, a new LH launcher is being designed and modeled. This launcher will be located off the midplane where improved single pass absorption can be achieved.[357,368] The design reduces

reflected power via a toroidal bi-junction while retaining the control of the $n_{\parallel}$ spectrum. Velocity space synergy with the midplane launcher is predicted to maximize the driven current at ITER relevant densities.

VIII. DISRUPTION STUDIES

At reactor scale, disruptions pose a serious challenge for tokamaks in general and to ITER in particular. The mechanical and thermal stresses along with the generation of large populations of relativistic electrons via avalanche amplification become unacceptable for large devices.[369] Performance trade-offs, which can place the design operating point near operational limits for current, pressure, or density, come with increased risk of disruption. Several of these issues can be non-trivial for C-Mod as well—its high field and very high plasma current density can lead to large forces, up to 600 kN (120 000 lbs) when the sudden loss of plasma current drives eddy and halo currents in its thick-walled, low resistance vacuum vessel.[19] Disruption forces and heat loads must also be taken into account when designing RF launching structures and in-vessel diagnostics, which are plentiful in C-Mod, as seen in Fig. 3.

The recognition of halo currents and their implications arose during the period of C-Mod construction following an event on JET that damaged vacuum components.[370] To address this critical issue, instrumentation was added to the C-Mod plasma facing components allowing spatially and temporally resolved measurements of the currents.[371] Subsequent observations found large halo currents associated with fast vertical displacement events, a common occurrence after the thermal quench. The halo currents were much stronger in the bottom (top) of the vacuum vessel when the displacement is down (up) and the temporal evolution of the halo current roughly followed dI_P/dt, lasting about 1–2 ms in C-Mod. The magnitude of the halo currents, I_H, was significant, generally in the range of 10%–20% of the plasma current, I_P, although there were significant outliers where I_H/I_P
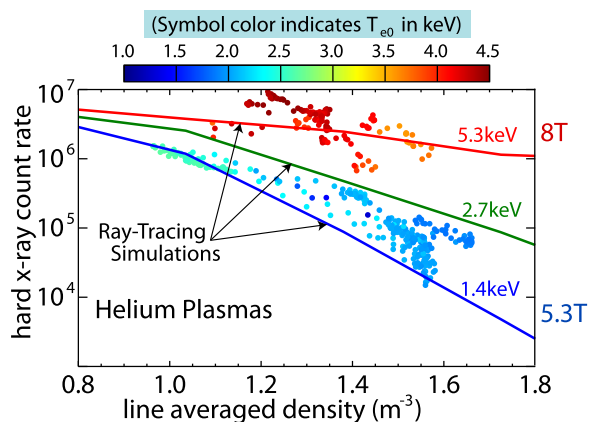

FIG. 62. Improved performance at high densities with higher temperatures. Shiraiwa *et al.*, Nuclear Fusion **53**, 113028 (2013). Copyright 2013 International Atomic Energy Agency.[357]
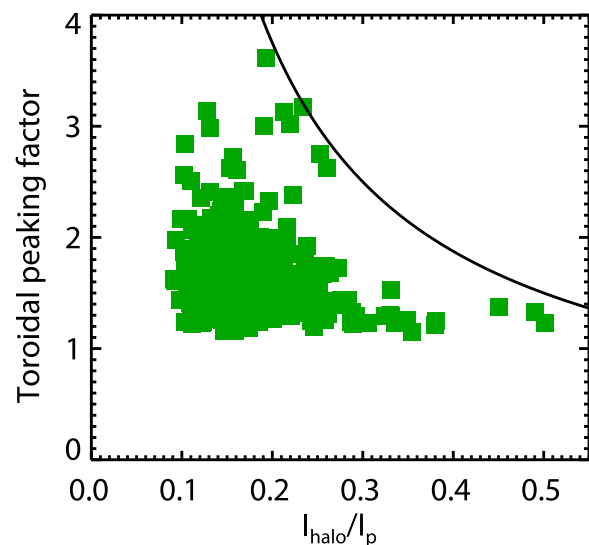

FIG. 63. Toroidal peaking of halo currents is lower for discharges with the highest conversion of plasma current to halo current, but the stresses on machine components can be dangerous over much of this range.
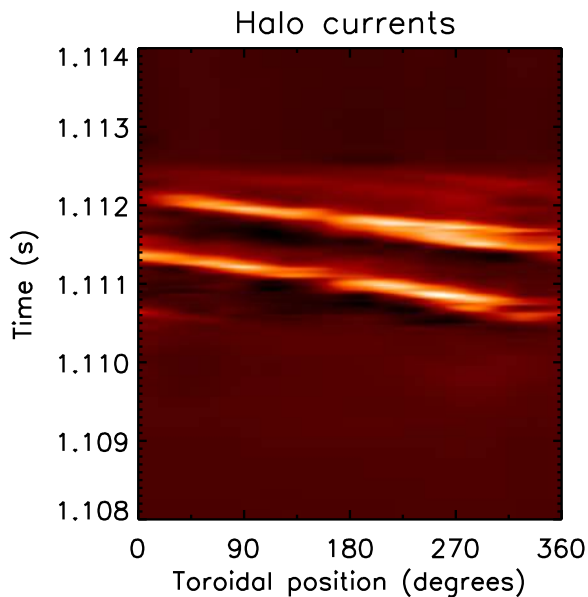
FIG. 64. C-Mod demonstrated that the toroidal structure of halo currents rotated rapidly, likely in response to the motion of the disrupting plasma. In this plot, the magnitude of halo currents in space and time is indicated by image brightness.

could reach as high as 0.5.[372] The halo current followed a scaling where $I_H/I_P = 0.63/q_{95}$ with a significant amount of scatter. The measured currents had a dominant toroidal structure, mainly corresponding to n = 1, but toroidal peaking factors above 3 were measured on some disruptions. This asymmetric current distribution poses a greater structural challenge than a symmetric one, but fortunately disruptions with higher I_H/I_P tended to be more symmetric. Still, as shown in Fig. 63, there were cases with toroidal peaking of 3 and $I_H/I_P > 0.2$. The measured poloidal thickness of the halo current distribution was relatively small—less than 3 cm in C-Mod. These data were contributed to an international database used to predict the impact of disruptions on ITER.[373]

The diagnostics on C-Mod were able to measure both the halo current ingress and egress positions—both showed the same toroidal asymmetry and had the same toroidal phase. That is, the currents flowing in the vessel were purely poloidal, perhaps not surprising since this is the path of lowest electrical resistance. In the plasma, it is assumed that the current flow is force-free, that is, it follows the helical magnetic field lines. Taken together, these two observations suggest that a spatial resonance condition on the plasma safety factor may be important in the dynamics of the current quench. The data from C-Mod demonstrated that the toroidal distribution of currents is not static, but can be seen to rotate at several kHz as seen in Fig. 64. During the rotation, the halo current could decay in less than 1 revolution or after as many as 10. The rotation rate is not fixed, even within any particular shot, and may slow and lock at a particular toroidal phase. The non-axisymmetric structure of the disrupting plasma and its rotation have important consequences for the symmetry of radiation and the ensuing heat load on the first wall, as discussed in Sec. VIII B.

Relativistic, runaway electrons can be produced by the high toroidal electric field that is generated by the thermal and current collapse during disruptions. The number of accelerated electrons grows exponentially via an avalanche amplification process. Generally, this problem gets more severe for machines at larger field, current, and size, since the magnitude of the drive is the total magnetic flux. In principle, a significant fraction of the plasma current could be converted to relativistic electrons and if these contacted the wall, the damage would be catastrophic. Under ordinary circumstances, significant runaway populations are not seen in disruptions on C-Mod. To study this phenomenon, LHCD was used to create a seed population of epithermal electrons that would require fewer exponential growth times to reach the runaway threshold. Under these conditions, runaways were observed during the thermal quench, but did not survive into the current quench. MHD simulations were consistent with a model where these electrons were lost through the break-up in the field structure by the large instabilities that accompany the disruption.[374] While initially promising, experiments on larger devices suggest that the confinement of fast electrons improves with device size and thus provides no relief of this problem for ITER. A more promising result was the observation that the critical electric field required to generate significant runaway populations was 5–10 times higher than previously predicted.[375,376] This observation relaxes the requirements for massive gas puffing that has been offered as a tool to curtail the avalanche process through collisional damping.

A. Disruption mitigation

If disruptions cannot be avoided entirely (and no machine has demonstrated operation at zero disruptivity), it will be necessary to mitigate the worst of their effects. These techniques have two goals. First, they should convert a substantial fraction of plasma kinetic and magnetic energy into radiation, which would then be deposited more uniformly on the first wall. Second, they should speed up the disruption process so that the current quenches before the vertical displacement proceeds too far and leads to unacceptably large halo currents. To accomplish these goals, a sufficient quantity of a radiative species must be deposited in the plasma in a time that is less than the disruption time scales. On C-Mod, a variety of methods was tested. Massive injection of high-speed cryogenic deuterium pellets delivered up to 2×10^{21} atoms, but did not increase the radiated power enough to change the disruption dynamics. Plastic pellets, with a 2.5 mg silver core, did reduce the quench time and the magnitude of halo currents. The most successful method tried was massive gas injection (MGI) in which a large inventory of noble gas was introduced by triggering a fast valve[377] connected to a high-pressure plenum.[378] For C-Mod, experiments were carried out with helium, neon, argon, and krypton, typically at a plenum pressure of 7 MPa (70 atm). The plumbing between the valve and nozzle was designed to maximize gas throughput, and the nozzle was placed as close to the plasma as possible. With this setup, up to 10^{23} atoms could be injected, equivalent to 300 times the inventory of plasma electrons.[379] In most experiments, the MGI was used to trigger the disruption as well as test the mitigation. This
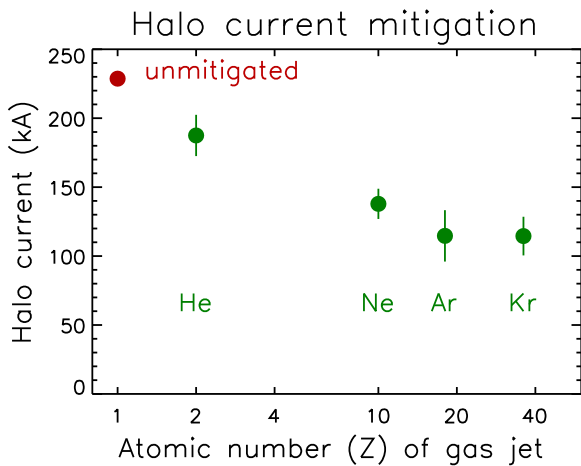
FIG. 65. The magnitude of halo currents could be reduced by injection of large quantities of noble gases. For purer gases, the effectiveness generally increased with atomic number, but the best results were obtained with a mix of helium (90%) and argon (10%). Reprinted with permission from Granetz *et al.*, Nuclear Fusion **46**, 1001 (2006). Copyright 2006 IOP.[379]

FIG. 67. Nonlinear MHD modeling with the combined NIMRAD code shows the evolution of the field structure throughout a mitigated disruption. The first panel shows the unperturbed flux surfaces that exist before edge cooling begins to destabilize the plasma. The second panel shows large magnetic islands and stochastic regions driven by the growth in MHD modes as the current channel shrinks. The last panel shows complete stochasticization of the field structure just 150 μs later. Time is measured from the triggering of the MGI system. Reproduced with permission from Phys. Plasmas **15**, 056109 (2008). Copyright 2008 AIP Publishing LLC.[178]

leaves for future research the techniques for real-time disruption prediction.

An open question, before the C-Mod work, was whether the impurities introduced by MGI could penetrate effectively into a plasma whose pressure exceeded the ram pressure of the gas jet. The C-Mod plasma pressure was about an order of magnitude higher than in tests of MGI on other devices, that is, comparable to what is expected on ITER. In the experiments, impurity penetration turned out not to be a limit on mitigation effectiveness, allowing more confident extrapolation to reactor-scale devices.[379,380] By imaging helium and neon radiation, it was found that the impurities do not get into the plasma as neutrals, suggesting instead that transport is aided by the large MHD fluctuations that are generated. Helium was found to penetrate rapidly all the way into the plasma core leading to very high

electron densities in the plasma core ($>2 \times 20^{21}/m^3$), but higher mass gases did not. Measurements with Thomson scattering showed that MGI rapidly cools the plasma edge in all cases. For pure gases, the trade-off was between speed, favoring lighter gases, and radiation, favoring the heavier gases. Both could be effective in speeding up the current quench and reducing halo currents. Figure 65 shows the reduction in halo currents as a function of the atomic number of the injected species. Energy lost to radiation increased from about 20% in an unmitigated disruption up to 90% with the highest level of radiation corresponding to injection of heavier gases. Further experiments found an optimum mixture, with roughly 10% argon in a helium carrier. Because the gas jet is highly collisional, it moves at the helium sound speed, bringing the argon with it. With this mix, I_H/I_P dropped a factor of three compared to an unmitigated disruption and the rate of current quench also exceeded the cases with pure gases.[381] Figure 66 shows a comparison between a mitigated and unmitigated disruption, where the reduction in vertical motion and the magnitude of halo currents is clear.

The first modeling of disruption mitigation was carried with the NIMROD code, a 3D, nonlinear, extended MHD model, coupled to an atomic physics/radiation package KPRAD.[382–384] The combination of codes is referred to as NIMRAD. Pure helium and pure neon injection experiments were modeled in the high plasma pressure, reactor-relevant regime. The simulations showed rapid edge cooling via radiation, with the evolution of the temperature profile roughly matching experimental measurements. The cold region, which is too resistive to support much current, expands inward over time and when it reaches about 0.85 normalized flux, about 3 cm in C-Mod, a large number of MHD modes is destabilized. The modes have very high growth rates, and the nonlinear evolution quickly leads to mode overlap and the appearance of stochastic regions. These regions rapidly cover the entire cross section, as shown in Fig. 67. Heat can then flow along the open field lines to regions of high electron and high impurity density where it is efficiently
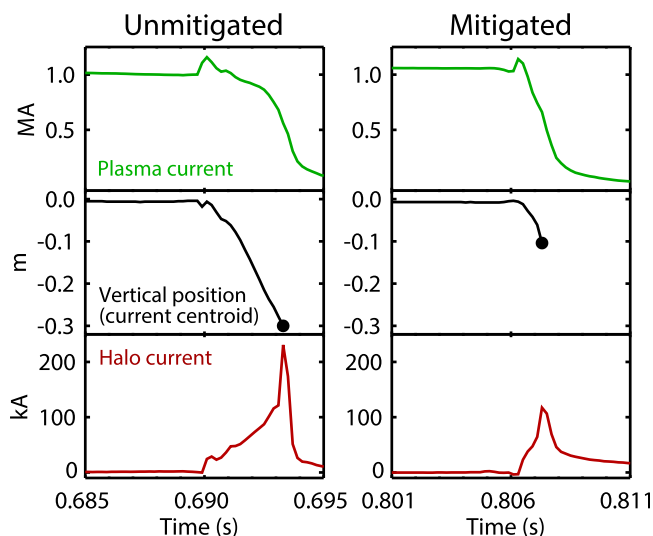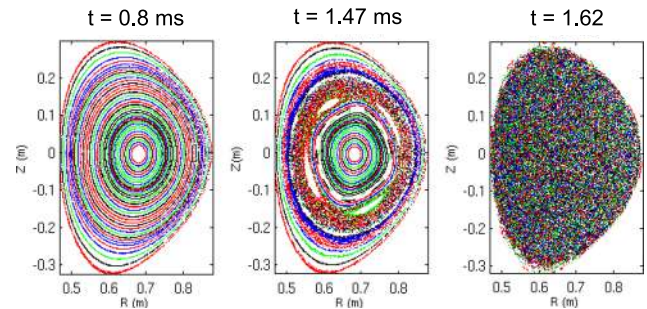

FIG. 66. This data demonstrate the mechanism of halo current mitigation. The massive gas injection leads to a faster current quench and thus to less vertical motion before the quench is complete. Reprinted with permission from Granetz *et al.*, Nuclear Fusion **46**, 1001 (2006). Copyright 2006 IOP.[379]
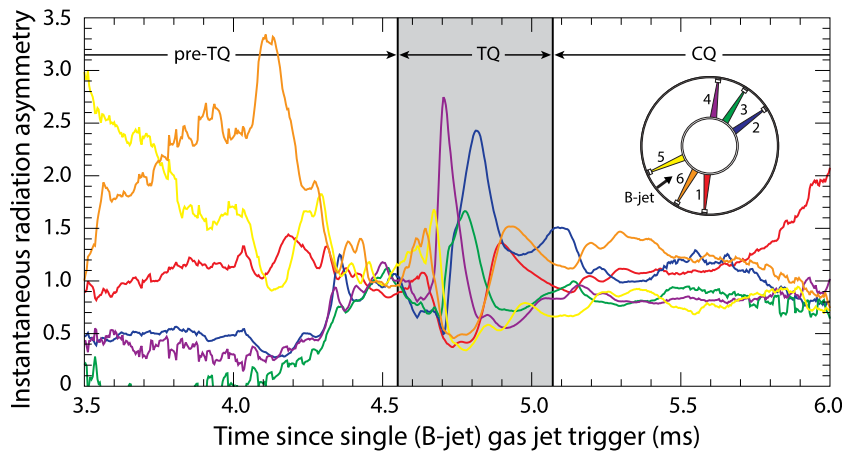
FIG. 68. The time evolution of radiation patterns after a mitigated disruption. Each trace corresponds to the ratio of one measured toroidal location to the sum of all measurements. The pattern is clearly highly asymmetric and time dependent.
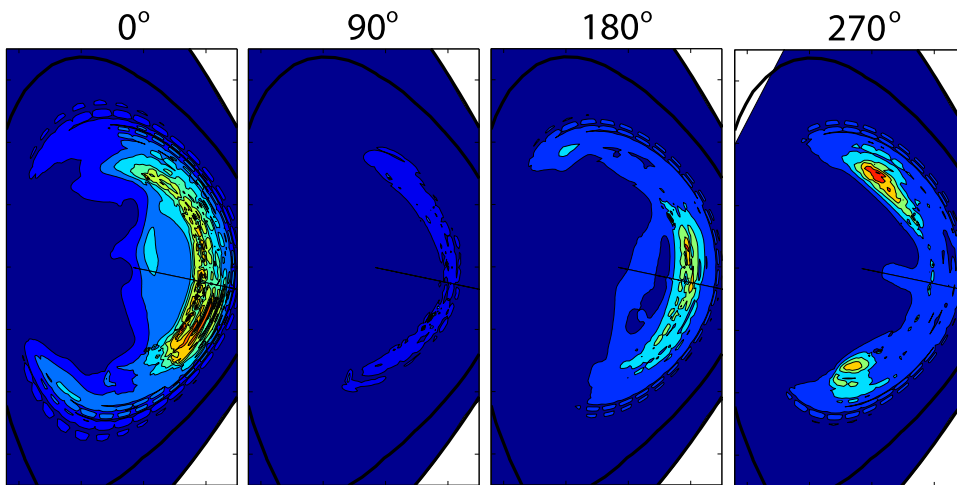

FIG. 69. Radiation patterns from 4 different toroidal locations from NIMRAD modeling of a mitigated disruption are shown. This strong 3D spatial structure is generally consistent with measurements, but the model cannot predict rotation from first principles.

converted to radiation. It is much more difficult to model the density evolution since it involves a balance between ionization and recombination and the role of MHD turbulence in mixing particles and impurities is not entirely clear. But the overall picture is consistent with experiments—impurities do not have to penetrate deeply to drive a rapid thermal quench. The stochastic fields predicted are sufficient to account for

the loss of fast electrons observed in C-Mod, but this effect is seen to become less important on larger devices, consistent with the experimental trends. As noted, ITER probably cannot count on this mechanism to avoid large runaway populations from disruptions.

Overall, these results are encouraging, MGI leads to lower thermal and mechanical loads and is compatible with high-Z metal walls and high plasma pressure. Deep penetration by neutrals is not required, easing the requirements for gas pressure/velocity. The models are helping to explain the underlying mechanisms, increasing confidence in the extrapolation to ITER.

B. Disruption mitigation—Radiation symmetry

The ITER design places very strict requirements on the symmetry of radiation from a mitigated disruption. Because of the lower surface to volume ratio, compared to current machines, and the low melting point of beryllium, which covers most of the ITER wall, a maximum peaking factor higher than 2 could cause localized beryllium melting. This concern is heightened by early results on C-Mod[385] that showed significant toroidal structure in the radiation. With a single injection point, using an optimized mixture of argon and helium, toroidal peaking factors, defined as the ratio of maximum to minimum radiation intensity, were found to be in the range of 1.2–2.3. The asymmetry depends sensitively
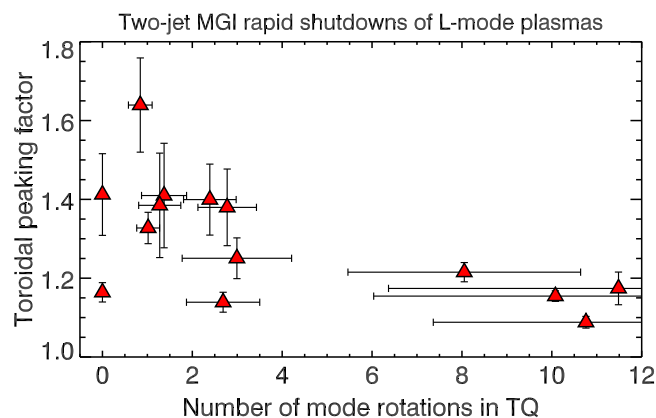

FIG. 70. C-Mod data shows that time-averaged radiation symmetry can be achieved in a disruption if the MHD modes rotate many times during the quench. For discharges where the rotation is slower compared to the disruption speed, the asymmetry becomes prominent. The prediction of radiation asymmetry in ITER mitigated disruption thus becomes dependent on predictions of plasma rotation during the disruption.

on magnetic geometry, with higher asymmetry in low-elongation plasmas and in higher q$_{95}$ diverted plasmas. Since the U.S. is responsible for the ITER disruption mitigation system, an accelerated program to understand the origins and remediation of the asymmetry was begun. A second MGI valve was added to C-Mod along with a set of diagnostics that could better characterize the radiation distribution. The hope was that injecting gas at additional locations would smooth out the distribution. It was found that multiple gas jets could help symmetrize radiation during the pre-thermal quench. But in the thermal quench itself, the MHD effects were seen to dominate, and multiple injection points were not necessarily helpful. The measured radiation evolution was complex, as seen in Fig. 68, corresponding to rotating 3D structures.[386] The radiation power loading was apparently always instantaneously peaked, but fast rotation could average out the effects on the wall. For slowly rotating disruptions, peaking can reach unacceptable levels. These results are likely coupled to the earlier observation of halo current asymmetry and rotation. Modeling with NIMRAD confirms that the radiation patterns have complex poloidal and toroidal structures, even with completely uniform distribution of gas (see Fig. 69). The models suggest that poloidal peaking may also be a concern, but we currently have no measurements to test this result. The code does not model plasma rotation self-consistently, so the implications for ITER are uncertain. What will matter is the number of rotation periods during the quench, as shown in Fig. 70, but this is currently beyond our ability to predict.

IX. SUMMARY OF SIGNATURE C-MOD ACHIEVEMENTS

- C-Mod is the highest field, diverted tokamak in the world with operation at 8 T and 2 MA.[19]
- Demonstrated tokamak initiation and control with a solid conducting vessel and structure.[13]
- Set world-record P/S power densities of ∼1 MW/m^2, producing reactor-level SOL parallel heat flux densities approaching 1 GW/m^2.[387]
- Demonstrated the feasibility of a very high-power tokamak operation with a high-Z divertor and plasma facing components, including measurement of erosion and fuel retention rates.[31,45,46,48]
- Invented and established the vertical plate divertor as most favorable for power and particle handling and explored divertor regimes at reactor-like plasma parameters including the neutral-neutral collisionality, neutral opacity, and photon opacity.[30,31,62,63]
- Discovered "main-chamber recycling" phenomenon in C-Mod's diverted plasmas and revealing intermittent, non-diffusive transport in the scrape-off layer as the underlying cause.[96]
- Demonstrated controlled divertor detachment using seeded impurities at high power density and demonstrated good H-mode confinement, H$_{98}$ ∼ 1, with Demo-like fractions (90%) of radiated power.[82–84]

- Uncovered evidence for the marginal stability paradigm for SOL turbulent transport with a critical β_P gradient decreasing at higher collisionality.[87,88]
- Identified edge plasma transport and its scaling with collisionality as a key physics ingredient in the empirical tokamak density limit.[87,104]
- Demonstrated that spatial asymmetries in turbulence and transport drive near-sonic parallel plasma flows in the plasma edge, imposing a toroidal rotation boundary condition for the confined plasma—suggesting a mechanism for the ∇B drift asymmetry in the L-H threshold.[113,148]
- Carried out the first experiments that characterized the L-H threshold as a critical local temperature or temperature gradient.[137,138]
- Demonstrated the two stationary ELM-free regimes, the EDA H-mode and I-Mode, where particle and impurity confinement were controlled by continuous, short wave-length electromagnetic modes in the pedestal.[173,174,388]
- Demonstrated the quantitative link between pedestal height and core performance across a wide range of operating conditions, validating the theoretically predicted dependence of turbulence on R/L$_T$.[17,266]
- Discovered and explored large self-generated toroidal flows in the core plasma.[205,213]
- Demonstrated creation of Internal Transport Barriers via self-generated plasma flows and demonstrated transport control with on-axis RF heating, identifying TEM turbulence via first direct comparison of experiment to nonlinear gyrokinetic simulations processed with synthetic diagnostic.[202,217,253,254,256,282]
- Validated gyrokinetic models simultaneously for ion energy, electron energy, and particle transport through groundbreaking, multi-scale simulations.[268,274]
- Proved experimentally that impurity asymmetry on flux surfaces occurs through mechanisms other than centrifugal force.[389–391]
- Carried out extensive studies of the spectroscopy and atomic physics of highly ionized atoms, including high n transitions and satellites, critical for development of plasma diagnostics and validation of atomic physics codes.[392–395]
- Operated ICRF systems routinely at power densities above 10 MW/m^2.[340,396,397]
- Validated full-wave ICRF models by comparison with measured wave fields, fast particle distributions, and local heating.[288,313,314,318,398]
- Demonstrated RF flow drive by ICRF mode conversion.[324]
- Pioneered the field aligned-antenna concept that dramatically reduced high-Z impurity levels in ICRF heated plasmas.[340]
- Demonstrated efficient off-axis current drive with lower hybrid.[347,351]
- Developed the first full-wave LH codes, using these to explain the decrease in current drive efficiency at high densities.[304,358,361,366,399]
- Showed the importance of spatial asymmetries and fast dynamics for disruption halo currents and disruption mitigation radiation.[372,386]

- Advanced the state-of-the-art for diagnosing the core, edge, and SOL plasma and plasma-material interactions.
- Developed MDSplus, a data acquisition and data management system that has become a standard for fusion experiments.[24,400]
- Trained over 170 graduate students in fusion science, engineering, and plasma physics.

APPENDIX: ALCATOR C-MOD CONTRIBUTORS

The following is a list of contributors to the facility design, construction, operation, and research. It is limited by the accuracy of our records and memories—our apologies if we have left anyone off.

P. Acedo, M. Agostini, J. Alex, A. Alfier, J. P. Allain, A. J. Allen, S. Allen, B. Alper, D. Andelin, R. A. Anderl, Y. Andrew, C. Angioni, G. Y. Antar, K. Arai, J. M. A. Ashbourn, M. E. Austin, A. Y. Aydemir, A. Ayyad, A. Bader, S. G. Baek, B. Bai, K. Bajwa, M. Bakhtiari, M. J. Baldwin, R. Ballinger, H. Barnard, M. Barnes, N. P. Basse, G. Bateman, O. V. Batishchev, A. A. Batishcheva, J. A. Baumgaertel, D. F. Beals, W. K. Beck, H. Becker, W. Beek, P. Beiersdorfer, E. M. Belli, P. Belo, R. D. Bengtson, W. F. Bergerson, S. Bernabei, L. A. Berry, I. Bespamyatnov, M. N. A. Beurskens, T. M. Biewer, A. S. Binus, A. Blair, J. A. Boedo, R. L. Boivin, F. Bombarda, A. Bondeson, X. Bonnin, P. T. Bonoli, P. Borner, M. C. Borras, A. Bortolon, J. Bosco, B. Bose, C. J. Boswell, M. Brambilla, S. Brandstetter, J. Brandwein, R. V. Bravenec, N. L. Bretz, J. U. Brill, C. Broennimann, J. N. Brooks, D. Brower, G. V. Brown, D. Brunner, R. Budny, W. M. Burke, C. E. Bush, D. N. Butner, W. Byford, D. Caldwell, A. Calisti, J. Candy, W. J. Carmack, B. A. Carreras, M. D. Carter, J. A. Casey, T. A. Casper, P. J. Catto, T. H. Chan, C. S. Chang, R. Chatterjee, R. Childs, M. A. Chilenski, B. Chin, M. Choi, C. Christensen, T. K. Chung, R. M. Churchill, G. Cima, J. Clementson, W. Cochran, T. Cochrane, J. W. Connor, G. D. Conway, B. Coppi, D. P. Coster, G. F. Counsell, I. Cziegler,

J. Daigle, R. Danforth, D. S. Darrow, E. M. Davis, W. Davis-Lee, J. Decker, P. P. Deichuli, G. Dekow, D. Del-Castillo-Negrete, L. F. Delgado-Aparicio, M. Demaria, A. Diallo, P. H. Diamond, W. X. Ding, D. A. D'ippolito, R. P. Doerner, C. W. Domier, A. Dominguez, J. Doody, W. Dorland, J. Dorris, J. F. Drake, B. P. Duval, E. M. Edlund, E. F. Eikenberry, E. C. Eisner, J. D. Elder, R. Ellis, R. C. Elton, P. C. Ennever, S. K. Erents, D. R. Ernst, T. E. Evans, S. Fairfax, A. Fasoli, I. Faust, M. Ferrara, M. Finkenthal, C. L. Fiore, E. Fitzgerald, K. B. Fournier, E. Fredd, T. W. Fredian, J. Friedberg, R. Gandy, S. Gangadhara, C. Gao, D. Garnier, D. Gates, K. Gentle, J. A. Goetz, W. H. Goldstein, T. Golfinopoulos, S. N. Golovato, N. N. Gorelenkov, A. Graf, M. A. Graf, R. S. Granetz, T. Graves, D. L. Green, N. Greenough, M. Greenwald, H. R. Griem, M. Grimes, F. J. Groebner, O. Grulke, M. F. Gu, D. Gwinn, T. S. Hahm, K. Hallatschek, G. R. Hanson, L. K. Harra, S. Harrison, R. W. Harvey, R. J. Hastie, J. Heard, T. C. Hender, K. W. Hill, E. M. Hollmann, S. F. Horne, J. C. Hosea, N. T. Howard, D. F. Howell, T. Hsu, A. E. Hubbard, J. W. Hughes, D. A. Humphreys, D. P. Hutchinson, I. H. Hutchinson, Y. In, A. Ince-cushman, J. Irby, V. A. Izzo, D. Jablonski, E. F. Jaeger, T. Jernigan, D. K. Johnson, K. Kamiya, A. D. Kanojia, C. F. Karney, F. P. Keenan, J. Kesner, C. Kessel, D. A. Knoll, S. Knowlton, J. A. Ko, P. Koert, W. Kondo, D. Kopon, G. J. Kramer, T. Kumagai, C. C. Kung, C. Kurz, B. Labombard, L. L. Lao, C. Lau, B. Leblanc, R. Leccacorvi, J. Lee, S. G. Lee, W. D. Lee, K. T. Liao, L. Lin, Y. Lin, B. Lipschultz, J. Liptac, S. Lisgo, D. H. Lo, A. Loarte, G. D. Loesser, T. Luke, D. Lumma, A. Lynn, C. H. Ma, Y. Ma, P. Macgibbon, G. P. Maddison, E. W. Magee, R. Maingi, R. Majeski, T. Manabe, R. J. Maqueda, E. S. Marmar, K. Marr, M. J. May, A. Mazurenko, S. M. Mccann, G. M. McCracken, R. M. McDermott, O. Meneghini, S. Migliuolo, D. R. Mikkelsen, H. W. Moos, D. Mossessian, R. A. Moyer, R. Mumgaard, R. Murray, L. Myatt, J. R. Myra, R. Nachtrieb, R. Nazikian, E. Nelson-Melby, W. M. Nevins, A. Niemczewski, R. Ochoukov, H. Ohkawa, P. J. Oshea, N. Oyama, N. Pablant, D. C. Pace, D. A. Pappas, A. Parisot, R. R. Parker, W. Parkin, P. B. Parks, J. Payne, T. S. Pedersen, R. D. Petrasso, A. Pfeiffer, C. K. Phillips, K. J. H. Phillips, P. E. Phillips, A. Y. Pigarov, S. D. Pinches, R. Pinsker, C. S. Pitcher, Y. Podpaly, M. Porkolab, E. Rachlewkallne, A. K. Ram, J. J. Ramos, J. C. Reardon, M. H. Redi, S. P. Regan, M. L. Reinke, D. Reiter, J. E. Rice, R. K. Richards, B. N. Rogers, T. D. Rognlien, Y. Rokhman, D. W. Ross, J. C. Rost, W. L. Rowan, J. Rushinski, D. A. Russell, M. Sampsell, J. Schachter, G. Schilling, A. E. Schmidt, D. Schmittdiel, R. Schneider, S. Scott, J. T. Scoville, J. Sears, S. Shiraiwa, D. J. Sigmar, A. N. Simakov, D. Simon, C. H. Skinner, N. Smick, A. P. Smirnov, D. Smith, J. A. Snipes, P. B. Snyder, M. Sohma, J. Sorci, P. C. Stangeby, P. Stek, J. A. Stillerman, P. B. Stotler, L. Sugiyama, C. Sung, Y. Takase, V. Tang, G. Taylor, D. R. Terry, J. L. Terry, C. Theiler, G. Tinios, P. H. Titus, N. Tsujii, K. Tsukada, M. Ulrickson, M. V. Umansky, E. Valeo, R. Vieira, J. R. Walk, G. Wallace, R. E. Waltz, W. R. Wampler, Y. Wang, R. Watterson, C. Watts, J. L. Weaver, B. L. Welch, J. C. Wesley, A. E. White, D. G. Whyte, J. Wilgen, H. Wilson, J. R. Wilson, M. Wilson, F.

Wising, S. M. Wolfe, A. J. Wootton, P. Woskov, G. M. Wright, J. C. Wright, S. J. Wukitch, G. A. Wurden, P. Xu, X. Q. Xu, I. Yamaguchi, B. Youngblood, H. Yuh, J. Zaks, X. Zhong, K. Zhurovich, and S. J. Zweben.

[1]B. B. Kadomtsev, Sov. J. Plasma Phys. **1**, 295 (1975).

[2]J. W. Connor and J. B. Taylor, Nucl. Fusion **17**, 1047 (1977).

[3]T. C. Hender, P. J. Knight, and I. Cook, Fusion Technol. **30**, 1605 (1996).

[4]D. Shafranov, Sov. Phys. Tech. Phys. USSR **15**, 175 (1970).

[5]M. Greenwald, J. L. Terry, S. M. Wolfe, S. Ejima, M. G. Bell, S. M. Kaye, and G. H. Neilson, Nucl. Fusion **28**, 2199 (1988).

[6]F. Troyon, R. Gruber, H. Saurenmann, S. Semenzato, and S. Succi, Plasma Phys. Controlled Fusion **26**, 209 (1984).

[7]ITER Physics Expert Group, Nucl. Fusion **39**, 2137 (1999).

[8]F. Najmabadi, T. A. Team, A. Abdou, L. Bromberg, T. Brown, V. C. Chan, M. C. Chu, F. Dahlgren, L. El-Guebaly, P. Heitzenroeder *et al.*, Fusion Eng. Des. **80**, 3 (2006).

[9]R. J. Goldston, Fusion Technol. **21**, 1050 (1992).

[10]D. M. Meade, Fusion Technol. **39**, 336 (2001).

[11]L. Bromberg, H. Hashizume, S. Ito, J. V. Minervini, and N. Yanagi, Fusion Sci. Technol. **60**, 635 (2011).

[12]B. N. Sorbom, J. Ball, T. Palmer, F. Mangiarotti, J. Sierchio, P. Bonoli, C. Kasten, D. Sutherland, H. Barnard, C. Haakonsen, J. Goh, C. Sung, and D. Whyte, "ARC: A compact, high-field fusion nuclear science facility and demonstration power plant with demountable magnets," Fusion Eng. Des. (submitted).

[13]I. H. Hutchinson, R. Boivin, F. Bombarda, P. Bonoli, S. Fairfax, C. Fiore, J. Goetz, S. Golovato, R. Granetz, M. Greenwald *et al.*, Phys. Plasmas **1**, 1511 (1994).

[14]E. S. Marmar, Fusion Sci. Technol. **51**, 261 (2007).

[15]M. Greenwald, D. Gwinn, S. Milora, J. Parker, R. Parker, S. Wolfe, M. Besen, F. Camacho, S. Fairfax, C. Fiore *et al.*, Phys. Rev. Lett. **53**, 352 (1984).

[16]M. Wakatani, V. S. Mukhovatov, K. H. Burrell, J. W. Connor, J. G. Cordey, Y. V. Esipchuk, X. Garbet, S. V. Lebedev, M. Mori, K. Toi *et al.*, Nucl. Fusion **39**, 2175 (1999).

[17]M. Greenwald, R. L. Boivin, F. Bombarda, P. T. Bonoli, C. L. Fiore, D. Garnier, J. A. Goetz, S. N. Golovato, M. A. Graf, R. S. Granetz *et al.*, Nucl. Fusion **37**, 793 (1997).

[18]M. Shimada, Nucl. Fusion **48**, 1 (2008).

[19]J. Irby, D. Gwinn, W. Beck, B. LaBombard, R. Granetz, and R. Vieira, Fusion Sci. Technol. **51**, 460 (2007).

[20]P. H. Titus, H. Becker, D. Gwinn, K. Rettman, and P. Stahle, in *Proceedings of the 18th IEEE Symposium on Fusion Engineering* (IEEE, New York, 1999), Vol. 1, p. 427.

[21]P. F. Isoz, J. B. Lister, and P. Marmillod, in *Proceedings of the 16th IEEE/IPSS Symposium on Fusion Engineering* (1990), Vol. 2, p. 1264.

[22]J. A. Stillerman, M. Ferrara, T. W. Fredian, and S. M. Wolfe, Fusion Eng. Des. **81**, 1905 (2006).

[23]J. Bosco and S. Fairfax, in *Proceedings of the 14th IEEE/NPSS Symposium on Fusion Engineering* (San Diego, 1991), Vol. 2, p. 782.

[24]T. W. Fredian and J. A. Stillerman, Fusion Eng. Des. **60**, 229 (2002).

[25]S. F. Horne, M. Greenwald, T. W. Fredian, I. H. Hutchinson, B. L. Labombard, J. Stillerman, Y. Takase, S. M. Wolfe, T. A. Casper, D. N. Butner *et al.*, Fusion Technol. **32**, 152 (1997).

[26]E. Hinnov, K. Bol, D. Dimock, R. J. Hawryluk, D. Johnson, M. Mattioli, E. Meservey, and S. Von Goeler, Nucl. Fusion **18**, 1305 (1978).

[27]B. LaBombard, B. Lipschultz, and S. Kochan, in *Proceedings of the 14th IEEE/NPSS Symposium on Fusion Engineering* (IEEE, New York, 1991), Vol. 1, p. 31.

[28]R. T. Nachtrieb, B. L. LaBombard, J. L. Terry, J. C. Reardon, W. L. Rowan, and W. R. Wampler, J. Nucl. Mater. **266–269**, 896 (1999).

[29]B. Lipschultz, Y. Lin, M. L. Reinke, A. Hubbard, I. H. Hutchinson, J. Irby, B. LaBombard, E. S. Marmar, K. Marr, J. L. Terry *et al.*, Phys. Plasmas **13**, 56117 (2006).

[30]B. Lipschultz, D. B. Montgomery, P. A. Politzer, and S. M. Wolfe, J. Nucl. Mater. **121**, 441 (1984).

[31]B. Lipschultz, B. LaBombard, J. L. Terry, C. Boswell, and I. H. Hutchinson, Fusion Sci. Technol. **51**, 369 (2007).

[32]P. C. Stangeby and A. W. Leonard, Nucl. Fusion **51**, 063001 (2011).

[33]D. G. Whyte, G. M. Olynyk, H. S. Barnard, P. T. Bonoli, L. Bromberg, M. L. Garrett, C. B. Haakonsen, Z. S. Hartwig, R. T. Mumgaard, and V. A. Podpaly, Fusion Eng. Des. **87**, 234 (2012).

[34]G. Federici, C. H. Skinner, J. N. Brooks, J. P. Coad, C. Grisolia, A. A. Haasz, A. Hassanein, V. Philipps, C. S. Pitcher, J. Roth *et al.*, Nucl. Fusion **41**, 1967 (2001).

[35]D. G. Whyte, J. Nucl. Mater. **390–391**, 911 (2009).

[36]G. Federici, P. Andrew, P. Barabaschi, J. Brooks, R. Doerner, A. Geier, A. Herrmann, G. Janeschitz, K. Krieger, A. Kukushkin *et al.*, J. Nucl. Mater. **313–316**, 11 (2003).

[37]S. Mirnov, J. Wesley, N. Fujisawa, Y. Gribov, O. Gruber, T. Hender, N. Ivanov, S. Jardin, J. Lister, F. Perkins *et al.*, Nucl. Fusion **39**, 2577 (1999).

[38]J. A. Snipes, R. S. Granetz, M. Greenwald, I. H. Hutchinson, D. Garnier, J. A. Goetz, S. N. Golovato, A. Hubbard, J. H. Irby, B. Labombard *et al.*, Nucl. Fusion **34**, 1039 (1994).

[39]S. J. Wukitch, D. Brunner, M. L. Garrett, B. LaBombard, C. Lau, Y. Lin, B. Lipschultz, R. Ochoukov, M. L. Reinke, J. L. Terry, and D. Whyte, in *Proceedings of the 24th IAEA Fusion Energy Conference* (San Diego, 2013), p. 406, see http://www-naweb.iaea.org/napc/physics/FEC/FEC2012/papers/287_FTP11.pdf.

[40]C. Angioni, H. Weisen, O. Kardaun, M. Maslov, A. Zabolotsky, C. Fuchs, L. Garzotti, C. Giroud, B. Kurzan, P. Mantica *et al.*, Nucl. Fusion **47**, 1326 (2007).

[41]J. W. Hughes, B. LaBombard, J. Terry, A. Hubbard, and B. Lipschultz, Nucl. Fusion **47**, 1057 (2007).

[42]Y. Takase, R. L. Boivin, F. Bombarda, P. T. Bonoli, C. L. Fiore, D. Garnier, J. A. Goetz, S. N. Golovato, R. S. Granetz, M. J. Greenwald *et al.*, Plasma Phys. Controlled Fusion **38**, 2215 (1996).

[43]B. Lipschultz, D. A. Pappas, B. LaBombard, J. E. Rice, D. Smith, and S. J. Wukitch, Nucl. Fusion **41**, 585 (2001).

[44]R. L. Neu, S. Brezinsek, M. Beurskens, V. Bobkov, P. de Vries, C. Giroud, E. Joffrin, A. Kallenbach, G. F. Matthews, M. L. Mayoral *et al.*, IEEE Trans. Plasma Sci. **42**, 552 (2014).

[45]W. R. Wampler, C. H. Skinner, C. S. Pitcher, B. LaBombard, B. Lipschultz, and C. Fiore, in *Proceedings of the 18th IEEE Symposium on Fusion Engineering* (1999), Vol. 1, p. 267.

[46]H. S. Barnard, B. Lipschultz, and D. G. Whyte, J. Nucl. Mater. **415**, S301 (2011).

[47]D. G. Whyte, J. N. Brooks, C. P. C. Wong, W. P. West, R. Bastasz, W. R. Wampler, and J. Rubenstein, J. Nucl. Mater. **241–243**, 660 (1997).

[48]B. Lipschultz, D. G. Whyte, J. Irby, B. LaBombard, and G. M. Wright, Nucl. Fusion **49**, 045009 (2009).

[49]K. L. Wilson, R. Bastasz, R. A. Causey, D. K. Brice, B. L. Doyle, W. R. Wampler, W. Moller, B. M. U. Scherzer, and T. Tanabe, Nucl. Fusion **1**, 31 (1991).

[50]K. B. Woller, D. G. Whyte, G. M. Wright, R. P. Doerner, and G. De Temmerman, J. Nucl. Mater. **438**, S913 (2013).

[51]G. M. Wright, D. Brunner, M. J. Baldwin, R. P. Doerner, B. Labombard, B. Lipschultz, J. L. Terry, and D. G. Whyte, Nucl. Fusion **52**, 042003 (2012).

[52]G. M. Wright, D. Brunner, M. J. Baldwin, K. Bystrov, R. P. Doerner, B. Labombard, B. Lipschultz, G. De Temmerman, J. L. Terry, D. G. Whyte *et al.*, J. Nucl. Mater. **438**, S84 (2013).

[53]Z. S. Hartwig and D. G. Whyte, Rev. Sci. Instrum. **81**, 10E106 (2010).

[54]Z. S. Hartwig, H. S. Barnard, R. C. Lanza, B. N. Sorbom, P. W. Stahle, and D. G. Whyte, Rev. Sci. Instrum. **84**, 123503 (2013).

[55]H. Barnard, Ph.D. thesis, Massachusetts Institute of Technology, 2014, see http://dspace.mit.edu/handle/1721.1/58385.

[56]Z. Hartwig, H. Barnard, B. Sorbom, R. Lanza, B. Lipschultz, P. Stahle, and D. Whyte, "Fuel retention measurements in Alcator C-Mod using accelerator-based in-situ materials surveillance," J. Nucl. Mater. (submitted).

[57]Z. Hartwig, Ph.D. thesis, Massachusetts Institute of Technology, 2014, see http://dspace.mit.edu/handle/1721.1/87488.

[58]B. LaBombard, J. Goetz, C. Kurz, D. Jablonski, B. Lipschultz, G. Mccracken, A. Niemczewski, R. L. Boivin, F. Bombarda, C. Christensen *et al.*, Phys. Plasmas **2**, 2242 (1995).

[59]B. LaBombard, J. A. Goetz, I. Hutchinson, D. Jablonski, J. Kesner, C. Kurz, B. Lipschultz, G. M. McCracken, A. Niemczewski, J. Terry *et al.*, J. Nucl. Mater. **241–243**, 149 (1997).

[60]B. Lipschultz, J. A. Goetz, I. Hutchinson, B. LaBombard, G. M. McCracken, Y. Takase, J. Terry, and P. Bonoli, in *Proceedings of the 16th International Atomic Energy Agency Conference on Fusion Energy* (IAEA, Montreal, 1996), Vol. 1, p. 425.

[61]A. S. Kukushkin, H. D. Pacher, V. Kotov, D. Reiter, D. Coster, and G. W. Pacher, Nucl. Fusion **45**, 608 (2005).

[62] J. L. Terry, B. Lipschultz, A. Y. Pigarov, C. Boswell, S. I. Krasheninnikov, B. LaBombard, and D. A. Pappas, At. Processes Plasmas **443**, 43 (1998).

[63] J. L. Terry, B. Lipschultz, A. Y. Pigarov, S. I. Krasheninnikov, B. LaBombard, D. Lumma, H. Ohkawa, D. Pappas, and M. Umansky, Phys. Plasmas **5**, 1759 (1998).

[64] A. Niemczewski, I. H. Hutchinson, B. LaBombard, B. Lipschultz, and G. M. McCracken, Nucl. Fusion **37**, 151 (1997).

[65] B. Lipschultz, B. LaBombard, S. Lisgo, and J. L. Terry, Fusion Sci. Technol. **51**, 390 (2007).

[66] J. A. Goetz, B. Lipschultz, C. S. Pitcher, J. L. Terry, P. T. Bonoli, J. E. Rice, and S. J. Wukitch, J. Nucl. Mater. **266–269**, 354 (1999).

[67] J. A. Goetz, C. S. Pitcher, B. LaBombard, B. Lipschultz, J. E. Rice, and J. L. Terry, Nucl. Fusion **41**, 1751 (2001).

[68] S. Lisgo, P. C. Stangeby, C. J. Boswell, J. D. Elder, B. LaBombard, B. Lipschultz, C. S. Pitcher, D. Reiter, and J. L. Terry, J. Nucl. Mater. **313–316**, 1089 (2003).

[69] S. Lisgo, P. Borner, C. Boswell, D. Elder, B. LaBombard, B. Lipschultz, C. S. Pitcher, D. Reiter, P. C. Stangeby, J. L. Terry *et al.*, J. Nucl. Mater. **337–339**, 139 (2005).

[70] J. L. Terry, B. LaBombard, D. Brunner, J. Payne, and G. A. Wurden, Rev. Sci. Instrum. **81**, 10E513 (2010).

[71] D. Brunner, B. LaBombard, J. Payne, and J. L. Terry, J. Nucl. Mater. **415**, S375 (2011).

[72] B. LaBombard, J. L. Terry, J. W. Hughes, D. Brunner, J. Payne, M. L. Reinke, I. Cziegler, R. Granetz, M. Greenwald, I. H. Hutchinson *et al.*, Phys. Plasmas **18**, 056104 (2011).

[73] B. LaBombard, J. L. Terry, J. W. Hughes, D. Brunner, J. Payne, M. L. Reinke, Y. Lin, and S. Wukitch, J. Nucl. Mater. **415**, S349 (2011).

[74] D. Brunner and B. LaBombard, Rev. Sci. Instrum. **83**, 033501 (2012).

[75] D. Brunner, Ph.D. thesis, Massachusetts Institute of Technology, 2013, see http://dspace.mit.edu/handle/1721.1/86420.

[76] D. Brunner, B. LaBombard, R. M. Churchill, J. Hughes, B. Lipschultz, R. Ochoukov, T. D. Rognlien, C. Theiler, J. Walk, M. V. Umansky *et al.*, Plasma Phys. Controlled Fusion **55**, 095010 (2013).

[77] D. Brunner, B. LaBombard, R. Ochoukov, and D. Whyte, Rev. Sci. Instrum. **84**, 033502 (2013).

[78] J. L. Terry, B. LaBombard, D. Brunner, J. W. Hughes, M. L. Reinke, and D. G. Whyte, J. Nucl. Mater. **438**, S212 (2013).

[79] A. Loarte, S. Bosch, A. Chankin, S. Clement, A. Herrmann, D. Hill, K. Itami, J. Lingertat, B. Lipschultz, K. McCormick *et al.*, J. Nucl. Mater. **266–269**, 587 (1999).

[80] G. Kirnev, W. Fundamenski, and G. Corrigan, Plasma Phys. Controlled Fusion **49**, 689 (2007).

[81] T. Eich, A. W. Leonard, R. A. Pitts, W. Fundamenski, R. J. Goldston, T. K. Gray, A. Herrmann, A. Kirk, A. Kallenbach, O. Kardaun *et al.*, Nucl. Fusion **53**, 093031 (2013).

[82] J. A. Goetz, B. LaBombard, B. Lipschultz, C. S. Pitcher, J. L. Terry, C. Boswell, S. Gangadhara, D. Pappas, J. Weaver, B. Welch *et al.*, Phys. Plasmas **6**, 1899 (1999).

[83] J. W. Hughes, A. Loarte, M. L. Reinke, J. L. Terry, D. Brunner, M. Greenwald, A. E. Hubbard, B. LaBombard, B. Lipschultz, Y. Ma *et al.*, Nucl. Fusion **51**, 083007 (2011).

[84] A. Loarte, J. W. Hughes, M. L. Reinke, J. L. Terry, B. LaBombard, D. Brunner, M. Greenwald, B. Lipschultz, Y. Ma, S. Wukitch *et al.*, Phys. Plasmas **18**, 056105 (2011).

[85] S. Wukitch, M. Garrett, H. Barnard, B. LaBombard, Y. Lin, B. Lipschultz, E. Marmar, R. Ochoukov, M. Reinke, D. Whyte, and G. Wright, in *Proceedings of the 23rd IAEA Fusion Energy Conference* (IAEA, Taejon, 2010), see http://www-pub.iaea.org/mtcd/meetings/PDFplus/2010/cn180/cn180_papers/exd_p3–37.pdf.

[86] B. LaBombard, D. Jablonski, B. Lipschultz, G. McCracken, and J. Goetz, J. Nucl. Mater. **220–222**, 976 (1995).

[87] B. LaBombard, R. L. Boivin, M. Greenwald, J. Hughes, B. Lipschultz, D. Mossessian, C. S. Pitcher, J. L. Terry, S. J. Zweben, and A. Grp, Phys. Plasmas **8**, 2107 (2001).

[88] B. LaBombard, J. W. Hughes, D. Mossessian, M. Greenwald, B. Lipschultz, J. L. Terry, and A. C. M. Team, Nucl. Fusion **45**, 1658 (2005).

[89] B. Scott, Plasma Phys. Controlled Fusion **39**, 1635 (1997).

[90] B. N. Rogers, J. F. Drake, and A. Zeiler, Phys. Rev. Lett. **81**, 4396 (1998).

[91] B. LaBombard, J. W. Hughes, N. Smick, A. Graf, K. Marr, R. McDermott, M. Reinke, M. Greenwald, B. Lipschultz, J. L. Terry *et al.*, Phys. Plasmas **15**, 056106 (2008).

[92] S. I. Krasheninnikov, Phys. Lett. A **283**, 368 (2001).

[93] J. L. Terry, R. Maqueda, C. S. Pitcher, S. J. Zweben, B. LaBombard, E. S. Marmar, A. Pigarov, and G. Wurden, J. Nucl. Mater. **290–293**, 757 (2001).

[94] S. J. Zweben, D. P. Stotler, J. L. Terry, B. LaBombard, M. Greenwald, M. Muterspaugh, C. S. Pitcher, K. Hallatschek, R. J. Maqueda, B. Rogers *et al.*, Phys. Plasmas **9**, 1981 (2002).

[95] S. J. Zweben and S. S. Medley, Phys. Fluids B **1**, 2058 (1989).

[96] B. LaBombard, M. V. Umansky, R. L. Boivin, J. A. Goetz, J. Hughes, B. Lipschultz, D. Mossessian, C. S. Pitcher, and J. L. Terry, Nucl. Fusion **40**, 2041 (2000).

[97] C. S. Pitcher, B. LaBombard, R. Danforth, W. Pina, M. Silveira, and B. Parkin, Rev. Sci. Instrum. **72**, 103 (2001).

[98] C. S. Pitcher, C. J. Boswell, J. A. Goetz, B. LaBombard, B. Lipschultz, J. E. Rice, and J. L. Terry, Phys. Plasmas **7**, 1894 (2000).

[99] J. L. Terry, S. J. Zweben, O. Grulke, M. J. Greenwald, and B. LaBombard, J. Nucl. Mater. **337–339**, 322 (2005).

[100] S. J. Zweben, J. L. Terry, M. Agostini, B. Davis, O. Grulke, R. Hager, J. Hughes, B. Labombard, D. A. D'Ippolito, J. R. Myra *et al.*, in *Proceedings of the 38th EPS Conference on Plasma Physics* (European Physical Society (EPS), Strasbourg, France, 2011), Vols. 35 and 2, p. 1608.

[101] O. E. Garcia, Phys. Rev. Lett. **108**, 265001 (2012).

[102] O. E. Garcia, I. Cziegler, R. Kube, B. LaBombard, and J. L. Terry, J. Nucl. Mater. **438**, S180 (2013).

[103] O. E. Garcia, S. M. Fritzner, R. Kube, I. Cziegler, B. LaBombard, and J. L. Terry, Phys. Plasmas **20**, 055901 (2013).

[104] M. Greenwald, Plasma Phys. Controlled Fusion **44**, R27 (2002).

[105] J. A. Wesson, R. D. Gill, M. Hugon, F. C. Schuller, J. A. Snipes, D. J. Ward, D. V. Bartlett, D. J. Campbell, P. A. Duperrex, A. W. Edwards *et al.*, Nucl. Fusion **29**, 641 (1989).

[106] K. Borrass, Nucl. Fusion **31**, 1035 (1991).

[107] B. Lipschultz, J. A. Goetz, B. Labombard, G. M. McCracken, H. Ohkawa, Y. Takase, and J. Terry, J. Nucl. Mater. **241–243**, 771 (1997).

[108] B. LaBombard, M. Greenwald, R. Boivin, B. Carreras, J. Hughes, B. Lipschultz, D. Mossessian, C. S. Pitcher, J. L. Terry, and S. Zweben, in *Proceedings of the 19th IAEA Fusion Energy Conference* (IAEA, Lyon, Vienna, 2002), see http://www-pub.iaea.org/MTCD/publications/PDF/csp_019c/html/node120.htm.

[109] X. Q. Xu, W. M. Nevins, T. D. Rognlien, R. H. Bulmer, M. Greenwald, A. Mahdavi, L. D. Pearlstein, and P. Snyder, Phys. Plasmas **10**, 1773 (2003).

[110] J. L. Terry, N. P. Basse, I. Cziegler, M. Greenwald, O. Grulke, B. LaBombard, S. J. Zweben, E. M. Edlund, J. W. Hughes, L. Lin *et al.*, Nucl. Fusion **45**, 1321 (2005).

[111] N. Smick and B. LaBombard, Rev. Sci. Instrum. **80**, 023502 (2009).

[112] B. LaBombard, J. E. Rice, A. E. Hubbard, J. W. Hughes, M. Greenwald, J. H. Irby, Y. Lin, B. Lipschultz, E. S. Marmar, N. Smick *et al.*, Nucl. Fusion **44**, 1047 (2004).

[113] B. LaBombard, J. E. Rice, A. E. Hubbard, J. W. Hughes, M. Greenwald, R. S. Granetz, J. H. Irby, Y. Lin, B. Lipschultz, E. S. Marmar *et al.*, Phys. Plasmas **12**, 056111 (2005).

[114] N. Smick, B. LaBombard, and I. H. Hutchinson, Nucl. Fusion **53**, 023001 (2013).

[115] J. W. Hughes, D. A. Mossessian, A. E. Hubbard, E. S. Marmar, D. Johnson, and D. Simon, Rev. Sci. Instrum. **72**, 1107 (2001).

[116] R. M. McDermott, B. Lipschultz, J. W. Hughes, P. J. Catto, A. E. Hubbard, I. H. Hutchinson, R. S. Granetz, M. Greenwald, B. LaBombard, K. Marr *et al.*, Phys. Plasmas **16**, 056103 (2009).

[117] R. M. Churchill, C. Theiler, B. Lipschultz, R. Dux, T. Putterich, E. Viezzer, C. M. T. Alcator, and A. U. Team, Rev. Sci. Instrum. **84**, 093505 (2013).

[118] S. Coda, M. Porkolab, and T. N. Carlstrom, Rev. Sci. Instrum. **63**, 4974 (1992).

[119] Y. Lin, J. Irby, P. Stek, I. Hutchinson, J. Snipes, R. Nazikian, and M. McCarthy, Rev. Sci. Instrum. **70**, 1078 (1999).

[120] J. A. Snipes, B. LaBombard, M. Greenwald, I. H. Hutchinson, J. Irby, Y. Lin, A. Mazurenko, and M. Porkolab, Plasma Phys. Controlled Fusion **43**, L23 (2001).

[121] A. Mazurenko, M. Porkolab, D. Mossessian, J. A. Snipes, X. Q. Xu, and W. M. Nevins, Phys. Rev. Lett. **89**, 225004 (2002).

[122] J. A. Snipes, R. S. Granetz, R. J. Hastie, A. E. Hubbard, Y. In, D. Mossessian, J. E. Rice, J. J. Ramos, D. Schmittdiel, G. Taylor *et al.*, Plasma Phys. Controlled Fusion **44**, 381 (2002).

[123]N. P. Basse, A. Dominguez, E. M. Edlund, C. L. Fiore, R. S. Granetz, A. E. Hubbard, J. W. Hughes, I. H. Hutchinson, J. H. Irby, B. LaBombard *et al.*, Fusion Sci. Technol. **51**, 476 (2007).

[124]B. LaBombard and L. Lyons, Rev. Sci. Instrum. **78**, 073501 (2007).

[125]J. L. Terry, S. J. Zweben, M. V. Umansky, I. Cziegler, O. Grulke, B. LaBombard, and D. P. Stotler, J. Nucl. Mater. **390–391**, 339 (2009).

[126]I. Cziegler, J. L. Terry, J. W. Hughes, and B. LaBombard, Phys. Plasmas **17**, 056120 (2010).

[127]W. F. Bergerson, P. Xu, J. H. Irby, D. L. Brower, W. X. Ding, and E. S. Marmar, Rev. Sci. Instrum. **83**, 10E316 (2012).

[128]C. P. Kasten, J. H. Irby, R. Murray, A. E. White, and D. C. Pace, Rev. Sci. Instrum. **83**, 10E301 (2012).

[129]Y. R. Martin and T. Takizuka, in *Proceedings of the 11th IAEA Technical Meeting on H-Mode Physics and Transport Barriers*, edited by T. Takizuka (IOP Publishing Ltd., Bristol, 2008), Vol. 123.

[130]J. A. Snipes, A. E. Hubbard, D. T. Garnier, S. N. Golovato, R. S. Granetz, M. Greenwald, I. H. Hutchinson, J. Irby, B. LaBombard, E. S. Marmar *et al.*, Plasma Phys. Controlled Fusion **38**, 1127 (1996).

[131]ASDEX, Nucl. Fusion **29**, 1959 (1989).

[132]Y. Ma, J. W. Hughes, A. E. Hubbard, B. LaBombard, R. M. Churchill, T. Golfinopolous, N. Tsujii, and E. S. Marmar, Nucl. Fusion **52**, 023010 (2012).

[133]J. Snipes, M. Greenwald, A. Hubbard, J. Hughes, B. LaBombard, and J. Rice, in Proceedings of the 35th European Physical Society Conference on Plasma Physics (ECA, Hersonissos, 2008), Vol. 32D, p. 1.074.

[134]C. F. Maggi, E. Delabie, T. M. Biewer, M. Groth, N. C. Hawkes, M. Lehnen, E. de la Luna, K. McCormick, C. Reux, F. Rimini *et al.*, Nucl. Fusion **54**, 023007 (2014).

[135]W. Fundamenski, F. Militello, D. Moulton, and D. C. McDonald, Nucl. Fusion **52**, 062003 (2012).

[136]Y. Ma, J. W. Hughes, A. E. Hubbard, B. LaBombard, and J. Terry, Plasma Phys. Controlled Fusion **54**, 082002 (2012).

[137]A. Hubbard, J. A. Goetz, M. Greenwald, I. Hutchinson, Y. In, J. Irby, and B. LaBombard, in Proceedings of the 16th International Atomic Energy Agency Conference on Fusion Energy (IAEA, Montreal, 1996), Vol. 1, p. 875.

[138]A. E. Hubbard, R. L. Boivin, J. F. Drake, M. Greenwald, Y. In, J. H. Irby, B. N. Rogers, and J. A. Snipes, Plasma Phys. Controlled Fusion **40**, 689 (1998).

[139]P. N. Guzdar and A. B. Hassam, Phys. Plasmas **3**, 3701 (1996).

[140]A. E. Hubbard, B. LaBombard, J. E. Rice, J. W. Hughes, M. Greenwald, R. S. Granetz, J. H. Irby, Y. Lin, B. Lipschultz, E. S. Marmar *et al.*, in *Proceedings of the 31st European Conference on Controlled Fusion and Plasma Physics* (European Physical Society, Geneva, London, UK, 2004), Vol. 28B, see http://130.246.71.128/pdf/O1_04.pdf.

[141]A. E. Hubbard, B. A. Carreras, R. L. Boivin, J. W. Hughes, E. S. Marmar, D. Mossessian, and S. J. Wukitch, Plasma Phys. Controlled Fusion **44**, A359 (2002).

[142]A. E. Hubbard, B. A. Carreras, N. P. Bassel, D. del-Castillo-Negrete, J. W. Hughes, A. Lynn, E. S. Marmar, D. Mossessian, P. Phillips, and S. Wukitch, Plasma Phys. Controlled Fusion **46**, A95 (2004).

[143]I. Cziegler, G. R. Tynan, P. H. Diamond, A. E. Hubbard, J. W. Hughes, J. Irby, and J. L. Terry, Plasma Phys. Controlled Fusion **56**, 075013 (2014).

[144]A. Fujisawa, Nucl. Fusion **49**, 013001 (2009).

[145]P. Manz, G. Birkenmeier, M. Ramisch, and U. Stroth, Phys. Plasmas **19**, 082318 (2012).

[146]M. Keilhacker, Plasma Phys. Controlled Fusion **29**, 1401 (1987).

[147]R. J. Groebner and T. Carlstrom, Plasma Phys. Controlled Fusion **40**, 673 (1998).

[148]J. E. Rice, A. E. Hubbard, J. W. Hughes, M. J. Greenwald, B. LaBombard, J. H. Irby, Y. Lin, E. S. Marmar, D. Mossessian, S. M. Wolfe *et al.*, Nucl. Fusion **45**, 251 (2005).

[149]R. J. Groebner, K. H. Burrell, and R. P. Seraydarian, Phys. Rev. Lett. **64**, 3015 (1990).

[150]A. E. Hubbard, K. Kamiya, N. Oyama, N. Basse, T. Biewer, E. Edlund, J. W. Hughes, L. Lin, M. Porkolab, W. Rowan *et al.*, Plasma Phys. Controlled Fusion **48**, A121 (2006).

[151]J. R. Walk, J. W. Hughes, A. Hubbard, J. Terry, D. Whyte, A. WHite, S. Baek, M. Reinke, C. Theiler, R. Churchill, J. Rice, P. Snyder, T. Osborne, A. Dominguez, and I. Cziegler, Phys. Plasmas **21**, 056103 (2014).

[152]P. B. Snyder, T. H. Osborne, K. H. Burrell, R. J. Groebner, A. W. Leonard, R. Nazikian, D. M. Orlov, O. Schmitz, M. R. Wade, and H. R. Wilson, Phys. Plasmas **19**, 056115 (2012).

[153]J. R. Walk, P. B. Snyder, J. W. Hughes, J. L. Terry, A. E. Hubbard, and P. E. Phillips, Nucl. Fusion **52**, 063011 (2012).

[154]J. W. Hughes, P. B. Snyder, J. R. Walk, E. M. Davis, A. Diallo, B. LaBombard, S. G. Baek, R. M. Churchill, M. Greenwald, R. J. Groebner *et al.*, Nucl. Fusion **53**, 043016 (2013).

[155]A. Diallo, J. W. Hughes, M. Greenwald, B. LaBombard, E. Davis, S. G. Baek, C. Theiler, P. Snyder, J. Canik, J. Walk *et al.*, Phys. Rev. Lett. **112**, 115001 (2014).

[156]J. L. Terry, I. Cziegler, A. E. Hubbard, J. A. Snipes, J. W. Hughes, M. J. Greenwald, B. LaBombard, Y. Lin, P. Phillips, and S. Wukitch, J. Nucl. Mater. **363–365**, 994 (2007).

[157]G. Federici, A. Loarte, and G. Strohmayer, Plasma Phys. Controlled Fusion **45**, 1523 (2003).

[158]A. Loarte, G. Saibene, R. Sartori, D. Campbell, M. Becoulet, L. Horton, T. Eich, A. Herrmann, G. Matthews, N. Asakura *et al.*, Plasma Phys. Controlled Fusion **45**, 1549 (2003).

[159]T. E. Evans, M. E. Fenstermacher, R. A. Moyer, T. H. Osborne, J. G. Watkins, P. Gohil, I. Joseph, M. J. Schaffer, L. R. Baylor, M. Bécoulet *et al.*, Nucl. Fusion **48**, 024002 (2008).

[160]L. R. Baylor, N. Commaux, T. C. Jernigan, S. J. Meitner, S. K. Combs, R. C. Isler, E. A. Unterberg, N. H. Brooks, T. E. Evans, A. W. Leonard *et al.*, Phys. Plasmas **20**, 082513 (2013).

[161]Y. Takase, R. L. Boivin, F. Bombarda, P. T. Bonoli, C. Christensen, C. Fiore, D. Garnier, J. A. Goetz, S. N. Golovato, R. Granetz *et al.*, Phys. Plasmas **4**, 1647 (1997).

[162]M. Greenwald, R. Boivin, P. Bonoli, R. Budny, C. Fiore, J. Goetz, R. Granetz, A. Hubbard, I. Hutchinson, J. Irby *et al.*, Phys. Plasmas **6**, 1943 (1999).

[163]J. W. Hughes, A. E. Hubbard, D. A. Mossessian, B. LaBombard, T. M. Biewer, R. S. Granetz, M. Greenwald, I. H. Hutchinson, J. H. Irby, Y. Lin *et al.*, Fusion Sci. Technol. **51**, 317 (2007).

[164]P. N. Yushmanov, T. Takizuka, K. S. Riedel, O. Kardaun, J. G. Cordey, S. M. Kaye, and D. E. Post, Nucl. Fusion **30**, 1999 (1990).

[165]K. Thomsen, G. Bracco, C. E. Bush, T. Carlstrom, A. Chudnovskii, G. Cordey, J. C. DeBoo, S. J. Fielding, T. Fukuda, M. Greenwald *et al.*, in Proceedings of the 17th International Conference on Plasma Physics and Controlled Nuclear Fusion Research (IAEA, Yokohama, 1998), Vol. 3, p. 987, see http://www-pub.iaea.org/MTCD/publications/PDF/csp_008c/fec1998/pdf/itp1_07.pdf.

[166]ITER Physics Expert Group, Nucl. Fusion **39**, 2175 (1999).

[167]D. A. Mossessian, P. Snyder, A. Hubbard, J. W. Hughes, M. Greenwald, B. LaBombard, J. A. Snipes, S. Wolfe, and H. Wilson, Phys. Plasmas **10**, 1720 (2003).

[168]J. W. Hughes, D. A. Mossessian, A. E. Hubbard, B. LaBombard, and E. S. Marmar, Phys. Plasmas **9**, 3019 (2002).

[169]D. A. Mossessian, R. J. Groebner, R. A. Moyer, T. H. Osborne, J. W. Hughes, M. Greenwald, A. Hubbard, and T. L. Rhodes, Phys. Plasmas **10**, 689 (2003).

[170]R. J. Groebner, C. S. Chang, J. W. Hughes, R. Maingi, P. B. Snyder, X. Q. Xu, J. A. Boedo, D. P. Boyle, J. D. Callen, J. M. Canik *et al.*, Nucl. Fusion **53**, 093024 (2013).

[171]R. J. Groebner, M. A. Mahdavi, A. W. Leonard, T. H. Osborne, N. S. Wolf, G. D. Porter, P. C. Stangeby, N. S. Brooks, R. J. Colchin, and L. W. Owen, Nucl. Fusion **44**, 204 (2004).

[172]J. W. Hughes, B. LaBombard, D. A. Mossessian, A. E. Hubbard, J. Terry, and T. Biewer, Phys. Plasmas **13**, 056103 (2006).

[173]D. G. Whyte, A. E. Hubbard, J. W. Hughes, B. Lipschultz, J. E. Rice, E. S. Marmar, M. Greenwald, I. Cziegler, A. Dominguez, T. Golfinopoulos *et al.*, Nucl. Fusion **50**, 105005 (2010).

[174]A. E. Hubbard, D. G. Whyte, R. M. Churchill, I. Cziegler, A. Dominguez, T. Golfinopoulos, J. W. Hughes, J. E. Rice, I. Bespamyatnov, M. J. Greenwald *et al.*, Phys. Plasmas **18**, 056115 (2011).

[175]A. E. White, M. Barnes, A. Dominguez, M. Greenwald, N. T. Howard, A. Hubbard, J. W. Hughes, D. Mikkelsen, F. Parra, M. Reinke, C. Sung, J. Walk, and D. Whyte, Nucl. Fusion **54**, 083019 (2014).

[176]G. D. Conway, C. Angioni, F. Ryter, P. Sauter, J. Vicente, and A. U. Team, Phys. Rev. Lett. **106**, 065001 (2011).

[177]F. Ryter, W. Suttrop, B. Brusehaber, M. Kaufmann, V. Mertens, H. Murmann, A. G. Peeters, J. Stober, J. Schweinzer, and H. Zohm, Plasma Phys. Controlled Fusion **40**, 725 (1998).

[178]A. E. Hubbard, J. W. Hughes, I. O. Bespamyatnov, T. Biewer, I. Cziegler, B. LaBombard, Y. Lin, R. McDermott, J. E. Rice, W. L. Rowan *et al.*, Phys. Plasmas **14**, 056109 (2007).

[179]A. E. Hubbard, E. Marmar, S. Baek, I. Ciegler, A. Dominguez, M. Greenwald, N. Howard, J. Hughes, B. LaBombard, M. Reinke *et al.*, in *Proceedings of the 24th IAEA Fusion Energy Conference* (IAEA,

San Diego, 2012), see http://www-naweb.iaea.org/napc/physics/FEC/FEC2012/papers/171_EX13.pdf.

[180]C. Theiler, R. M. Churchill, B. Lipschultz, M. Landreman, D. Ernst, J. Hughes, P. Catto, F. Parra, I. Hutchinson, M. Reinke, A. Hubbard, E. Marmar, J. Terry, and J. Walk, Nucl. Fusion **54**, 083017 (2014).

[181]N. T. Howard, M. Greenwald, and J. E. Rice, Rev. Sci. Instrum. **82**, 033512 (2011).

[182]M. Greenwald, C. Angioni, J. W. Hughes, J. Terry, and H. Weisen, Nucl. Fusion **47**, L26 (2007).

[183]P. Stek, Ph.D. thesis, MIT, 1997, see http://dspace.mit.edu/handle/1721.1/10367.

[184]B. LaBombard, T. Golfinopoulos, J. L. Terry, D. Brunner, E. Davis, M. Greenwald, J. W. Hughes, and Alcator C-Mod Team, Phys. Plasmas **21**, 056108 (2014).

[185]M. Greenwald, N. Basse, P. Bonoli, R. Bravenec, E. Edlund, D. Ernst, C. Fiore, R. Granetz, A. Hubbard, J. Hughes *et al.*, Fusion Sci. Technol. **51**, 266 (2007).

[186]X. Q. Xu, R. H. Cohen, T. D. Rognlien, and J. R. Myra, Phys. Plasmas **7**, 1951 (2000).

[187]A. E. White, P. Phillips, D. G. Whyte, A. E. Hubbard, C. Sung, J. W. Hughes, A. Dominguez, J. Terry, and I. Cziegler, Nucl. Fusion **51**, 113005 (2011).

[188]A. Dominguez, Ph.D. thesis, Massachusetts Institute of Technology, 2012, see http://dspace.mit.edu/handle/1721.1/79261.

[189]I. Cziegler, P. H. Diamond, N. Fedorczak, P. Manz, G. R. Tynan, M. Xu, R. M. Churchill, A. E. Hubbard, B. Lipschultz, J. M. Sierchio *et al.*, Phys. Plasmas **20**, 055904 (2013).

[190]J. W. Connor, R. J. Hastie, H. R. Wilson, and R. L. Miller, Phys. Plasmas **5**, 2687 (1998).

[191]H. R. Wilson, P. B. Snyder, G. T. A. Huysmans, and R. L. Miller, Phys. Plasmas **9**, 1277 (2002).

[192]A. Burckhart, E. Wolfrum, R. Fischer, K. Lackner, H. Zohm, and A. U. Team, Plasma Phys. Controlled Fusion **52**, 105010 (2010).

[193]W. Dorland, F. Jenko, M. Kotschenreuther, and B. N. Rogers, Phys. Rev. Lett. **85**, 5579 (2000).

[194]J. W. Hughes, A. E. Hubbard, G. Wallace, M. Greenwald, B. LaBombard, L. Lin, R. M. McDermott, R. R. Parker, M. L. Reinke, J. E. Rice *et al.*, Nucl. Fusion **50**, 064001 (2010).

[195]T. Golfinopoulos, B. LaBombard, R. Parker, W. Burke, E. Davis, R. Granetz, M. Greenwald, J. Irby, R. Leccacorvi, E. Marmar *et al.*, Phys. Plasmas **21**, 056111 (2014).

[196]T. Golfinopoulos, B. LaBombard, W. Burke, R. R. Parker, W. Parkin, and P. Woskov, Rev. Sci. Instrum. **85**, 043510 (2014).

[197]M. Greenwald, A. Bader, S. Baek, H. Barnard, W. Beck, W. Bergerson, I. Bespamyatnov, M. Bitter, P. Bonoli, M. Brookman *et al.*, Nucl. Fusion **53**, 104004 (2013).

[198]T. C. Luce, C. C. Petty, J. G. Cordey, B. Balet, R. Budny, M. Greenwald, and J. Schachter, Nucl. Fusion **42**, 1193 (2002).

[199]M. Kotschenreuther, W. Dorland, Q. P. Liu, G. W. Hammett, M. A. Beer, S. A. Smith, A. Bondeson, and S. C. Cowley, in Proceedings of the 16th IAEA Fusion Energy Conference (IAEA, Vienna, 1996), Vol. 2, p. 371.

[200]D. R. Mikkelsen and W. Dorland, Phys. Rev. Lett. **101**, 135003 (2008).

[201]N. P. Basse, E. M. Edlund, D. R. Ernst, C. L. Fiore, M. J. Greenwald, A. E. Hubbard, J. W. Hughes, J. H. Irby, L. Lin, Y. Lin *et al.*, Phys. Plasmas **12**, 052512 (2005).

[202]S. J. Wukitch, R. L. Boivin, P. T. Bonoli, C. L. Fiore, R. S. Granetz, M. J. Greenwald, A. E. Hubbard, I. H. Hutchinson, Y. In, J. Irby *et al.*, Phys. Plasmas **9**, 2149 (2002).

[203]A. Ince-Cushman, J. E. Rice, M. Bitter, M. L. Reinke, K. W. Hill, M. F. Gu, E. Eikenberry, C. Broennimann, S. Scott, Y. Podpaly *et al.*, Rev. Sci. Instrum. **79**, 10E302 (2008).

[204]J. E. Rice, E. S. Marmar, F. Bombarda, and L. Qu, Nucl. Fusion **37**, 421 (1997).

[205]J. E. Rice, M. Greenwald, I. H. Hutchinson, E. S. Marmar, Y. Takase, S. M. Wolfe, and F. Bombarda, Nucl. Fusion **38**, 75 (1998).

[206]I. H. Hutchinson, J. E. Rice, R. S. Granetz, and J. A. Snipes, Phys. Rev. Lett. **84**, 3330 (2000).

[207]J. E. Rice, J. A. Goetz, R. S. Granetz, M. J. Greenwald, A. E. Hubbard, I. H. Hutchinson, E. S. Marmar, D. Mossessian, T. S. Pedersen, J. A. Snipes *et al.*, Phys. Plasmas **7**, 1825 (2000).

[208]J. E. Rice, P. T. Bonoli, J. A. Goetz, M. J. Greenwald, I. H. Hutchinson, E. S. Marmar, M. Porkolab, S. M. Wolfe, S. J. Wukitch, and C. S. Chang, Nucl. Fusion **39**, 1175 (1999).

[209]J. E. Rice, E. S. Marmar, P. T. Bonoli, R. S. Granetz, M. J. Greenwald, A. E. Hubbard, J. W. Hughes, I. H. Hutchinson, J. H. Irby, B. LaBombard *et al.*, Fusion Sci. Technol. **51**, 288 (2007).

[210]M. Yoshida, S. Kaye, J. Rice, W. Solomon, T. Tala, R. E. Bell, K. H. Burrell, J. Ferreira, Y. Kamada, D. McDonald *et al.*, Nucl. Fusion **52**, 123005 (2012).

[211]W. D. Lee, J. E. Rice, E. S. Marmar, M. J. Greenwald, I. H. Hutchinson, and J. A. Snipes, Phys. Rev. Lett. **91**, 205003 (2003).

[212]J. E. Rice, W. D. Lee, E. S. Marmar, P. T. Bonoli, R. S. Granetz, M. J. Greenwald, A. E. Hubbard, I. H. Hutchinson, J. H. Irby, Y. Lin *et al.*, Nucl. Fusion **44**, 379 (2004).

[213]J. E. Rice, J. W. Hughes, P. H. Diamond, Y. Kosuga, Y. A. Podpaly, M. L. Reinke, M. J. Greenwald, O. D. Gurcan, T. S. Hahm, A. E. Hubbard *et al.*, Phys. Rev. Lett. **106**, 215001 (2011).

[214]H. Biglari, P. H. Diamond, and P. W. Terry, Phys. Fluids B **2**, 1 (1990).

[215]P. W. Terry, Rev. Mod. Phys. **72**, 109 (2000).

[216]J. E. Rice, P. T. Bonoli, C. L. Fiore, W. D. Lee, E. S. Marmar, S. J. Wukitch, R. S. Granetz, A. E. Hubbard, J. W. Hughes, J. H. Irby *et al.*, Nucl. Fusion **43**, 781 (2003).

[217]C. L. Fiore, D. R. Ernst, Y. A. Podpaly, D. Mikkelsen, N. T. Howard, J. Lee, M. L. Reinke, J. E. Rice, J. W. Hughes, Y. Ma *et al.*, Phys. Plasmas **19**, 056113 (2012).

[218]J. E. Rice, A. C. Ince-Cushman, M. L. Reinke, Y. Podpaly, M. J. Greenwald, B. LaBombard, and E. S. Marmar, Plasma Phys. Controlled Fusion **50**, 124042 (2008).

[219]J. E. Rice, M. J. Greenwald, Y. A. Podpaly, M. L. Reinke, P. H. Diamond, J. W. Hughes, N. T. Howard, Y. Ma, I. Cziegler, B. P. Duval *et al.*, Phys. Plasmas **19**, 056106 (2012).

[220]A. Bortolon, B. P. Duval, A. Pochelon, and A. Scarabosio, PRL **97**, 235003 (2006).

[221]C. Sung, A. E. White, N. T. Howard, C. Y. Oi, J. E. Rice, C. Gao, P. Ennever, M. Porkolab, F. Parra, D. Mikkelsen *et al.*, Nucl. Fusion **53**, 083010 (2013).

[222]R. R. Parker, M. Greenwald, S. C. Luckhardt, E. S. Marmar, M. Porkolab, and S. M. Wolfe, Nucl. Fusion **25**, 1127 (1985).

[223]J. E. Rice, B. P. Duval, M. L. Reinke, Y. A. Podpaly, A. Bortolon, R. M. Churchill, I. Cziegler, P. H. Diamond, A. Dominguez, P. C. Ennever *et al.*, Nucl. Fusion **51**, 083005 (2011).

[224]S. M. Wolfe, M. Greenwald, R. Gandy, R. Granetz, C. Gomez, D. Gwinn, B. Lipschultz, S. Mccool, E. Marmar, J. Parker *et al.*, Nucl. Fusion **26**, 329 (1986).

[225]J. E. Rice, C. Gao, M. L. Reinke, P. H. Diamond, N. T. Howard, H. J. Sun, I. Cziegler, A. E. Hubbard, Y. A. Podpaly, W. L. Rowan *et al.*, Nucl. Fusion **53**, 033004 (2013).

[226]C. Gao, J. E. Rice, H. J. Sun, M. L. Reinke, N. T. Howard, D. Mikkelson, A. E. Hubbard, M. A. Chilenski, J. R. Walk, J. W. Hughes *et al.*, Nucl. Fusion **54**, 083025 (2014).

[227]A. Ince-Cushman, J. E. Rice, M. Reinke, M. Greenwald, G. Wallace, R. Parker, C. Fiore, J. W. Hughes, P. Bonoli, S. Shiraiwa *et al.*, Phys. Rev. Lett. **102**, 035002 (2009).

[228]J. E. Rice, A. C. Ince-Cushman, P. T. Bonoli, M. J. Greenwald, J. W. Hughes, R. R. Parker, M. L. Reinke, G. M. Wallace, C. L. Fiore, R. S. Granetz *et al.*, Nucl. Fusion **49**, 025004 (2009).

[229]J. E. Rice, Y. A. Podpaly, M. L. Reinke, C. Gao, S. Shiraiwa, J. L. Terry, C. Theiler, G. M. Wallace, P. T. Bonoli, D. Brunner *et al.*, Nucl. Fusion **53**, 093015 (2013).

[230]J. E. Rice, Y. A. Podpaly, M. L. Reinke, R. Mumgaard, S. D. Scott, S. Shiraiwa, G. M. Wallace, B. Chouli, C. Fenzi-Bonizec, M. F. F. Nave *et al.*, Phys. Rev. Lett. **111**, 125003 (2013).

[231]M. L. Reinke, J. E. Rice, A. E. White, M. Greenwald, N. T. Howard, P. Ennever, C. Gao, A. E. Hubbard, and J. W. Hughes, Plasma Phys. Controlled Fusion **55**, 012001 (2013).

[232]T. Luke, Ph.D. thesis, Massachusetts Institute of Technology, 1995, see http://dspace.mit.edu/handle/1721.1/11755.

[233]D. Mikkelsen, M. Greenwald, J. Candy, and R. Waltz, Bull. Am. Phys. Soc. **52**, 154 (2007).

[234]C. Angioni, E. Fable, M. Greenwald, M. Maslov, A. G. Peeters, H. Takenaga, and H. Weisen, Plasma Phys. Controlled Fusion **51**, 124017 (2009).

[235]J. E. Rice, J. L. Terry, J. A. Goetz, Y. Wang, E. S. Marmar, M. Greenwald, I. Hutchinson, Y. Takase, S. Wolfe, H. Ohkawa *et al.*, Phys. Plasmas **4**, 1605 (1997).

[236]J. E. Rice, J. L. Terry, E. S. Marmar, R. S. Granetz, M. J. Greenwald, A. E. Hubbard, J. H. Irby, S. M. Wolfe, and T. S. Pedersen, Fusion Sci. Technol. **51**, 357 (2007).

[237]R. A. Hulse, *Modeling of Impurity Transport in the Core Plasma* (Elsevier Science Publ B V, Amsterdam, 1993); R. K. Janev, *Atomic and Plasma-Material Interaction Processes in Controlled Thermonuclear Fusion* (Elsevier, 1993).

[238]T. S. Pedersen and R. S. Granetz, Rev. Sci. Instrum. **70**, 586 (1999).

[239]T. S. Pedersen, R. S. Granetz, A. E. Hubbard, I. H. Hutchinson, E. S. Marmar, J. E. Rice, and J. Terry, Nucl. Fusion **40**, 1795 (2000).

[240]R. M. Churchill, B. Lipschultz, C. Theiler, and C. M. T. Alcator, Nucl. Fusion **53**, 122002 (2013).

[241]R. Dux, STRAHL User Manual, 2000, see http://www.edoc.mpg.de/285559.

[242]M. L. Reinke, P. Beiersdorfer, N. T. Howard, E. W. Magee, Y. Podpaly, J. E. Rice, and J. L. Terry, Rev. Sci. Instrum. **81**, 10D736 (2010).

[243]N. T. Howard, M. Greenwald, D. R. Mikkelsen, M. L. Reinke, A. E. White, D. Ernst, Y. Podpaly, and J. Candy, Nucl. Fusion **52**, 063002 (2012).

[244]N. T. Howard, A. E. White, M. L. Reinke, M. Greenwald, C. Holland, J. Candy, and J. R. Walk, Nucl. Fusion **53**, 123011 (2013).

[245]R. C. Wolf, Plasma Phys. Controlled Fusion **45**, R1 (2003).

[246]J. W. Connor, T. Fukuda, X. Garbet, C. Gormezano, V. Mukhovatov, M. Wakatani, I. T. B. D. Grp, and I. T. G. T. Intern, Nucl. Fusion **44**, R1 (2004).

[247]A. C. C. Sips, A. Peeters, F. Ryter, R. Wolf, M. Greenwald, P. Gohil, C. Greenfield, J. Kinsey, E. Barbato, G. Bracco *et al.*, Plasma Phys. Controlled Fusion **44**, A391 (2002).

[248]C. L. Fiore, D. R. Ernst, J. E. Rice, K. Zhurovich, N. Basse, P. T. Bonoli, M. J. Greenwald, E. S. Marmar, and S. J. Wukitch, Fusion Sci. Technol. **51**, 303 (2007).

[249]D. T. Garnier, E. S. Marmar, C. L. Fiore, J. A. Goetz, S. N. Golovato, M. J. Greenwald, A. E. Hubbard, J. H. Irby, P. J. O'Shea, J. J. Ramos *et al.*, in *Proceedings of the 16th IAEA Fusion Energy Conference* (IAEA, 1996), Vol. 1, p. 907.

[250]C. L. Fiore, J. E. Rice, P. T. Bonoli, R. L. Boivin, J. A. Goetz, A. E. Hubbard, I. H. Hutchinson, R. S. Granetz, M. J. Greenwald, E. S. Marmar *et al.*, Phys. Plasmas **8**, 2023 (2001).

[251]J. E. Rice, R. L. Boivin, P. T. Bonoli, J. A. Goetz, R. S. Granetz, M. J. Greenwald, I. H. Hutchinson, E. S. Marmar, G. Schilling, J. A. Snipes *et al.*, Nucl. Fusion **41**, 277 (2001).

[252]M. Greenwald, M. Besen, F. Camacho, C. Fiore, M. Foord, R. Gandy, C. Gomez, R. Granetz, D. Gwinn, S. Knowlton *et al.*, in *Proceedings of the IAEA 11th International Conference on Plasma Physics and Controlled Nuclear Fusion Research* (IAEA, Kyoto, 1986), Vol. 1, p. 139.

[253]J. E. Rice, P. T. Bonoli, E. S. Marmar, S. J. Wukitch, R. L. Boivin, C. L. Fiore, R. S. Granetz, M. J. Greenwald, A. E. Hubbard, J. W. Hughes *et al.*, Nucl. Fusion **42**, 510 (2002).

[254]C. L. Fiore, P. T. Bonoli, D. R. Ernst, M. J. Greenwald, E. S. Marmar, M. H. Redi, J. E. Rice, S. J. Wukitch, and K. Zhurovich, Plasma Phys. Controlled Fusion **46**, B281 (2004).

[255]C. L. Fiore, P. T. Bonoli, D. R. Ernst, A. E. Hubbard, M. J. Greenwald, A. Lynn, E. S. Marmar, P. Phillips, M. H. Redi, J. E. Rice *et al.*, Phys. Plasmas **11**, 2480 (2004).

[256]D. R. Ernst, P. T. Bonoli, P. J. Catto, W. Dorland, C. L. Fiore, R. S. Granetz, M. Greenwald, A. E. Hubbard, M. Porkolab, M. H. Redi *et al.*, Phys. Plasmas **11**, 2637 (2004).

[257]C. L. Fiore, J. E. Rice, Y. Podpaly, I. O. Bespamyatnov, W. L. Rowan, J. W. Hughes, and M. Reinke, Nucl. Fusion **50**, 064008 (2010).

[258]K. Zhurovich, C. L. Fiore, D. R. Ernst, P. T. Bonoli, M. J. Greenwald, A. E. Hubbard, J. W. Hughes, E. S. Marmar, D. R. Mikkelsen, P. Phillips *et al.*, Nucl. Fusion **47**, 1220 (2007).

[259]D. R. Ernst, N. Basse, P. T. Bonoli, P. J. Catto, W. Dorland, C. L. Fiore, M. Greenwald, A. E. Hubbard, E. S. Marmar, M. Porkolab *et al.*, in *Proceedings of the 20th Int'l. Atomic Energy Agency Fusion Energy Conference* (IAEA, Vilamoura, 2004), see http://www-naweb.iaea.org/napc/physics/fec/fec2004/datasets/TH_4-1.html.

[260]D. Ernst, N. Basse, W. Dorland, C. Fiore, L. Lin, A. Long, M. Porkolab, K. Zeller, and K. Zhurovich, in *Proceedings of the 21st International Atomic Energy Agency Fusion Energy Conference*, edited by IAEA (IAEA, Chengdu, 2006), see *http://*www-pub.iaea.org/MTCD/Meetings/FEC2006/th_1-3.pdf.

[261]M. Greenwald, Comput. Phys. Commun. **164**, 1 (2004).

[262]P. W. Terry, M. Greenwald, J. N. Leboeuf, G. R. McKee, D. R. Mikkelsen, W. M. Nevins, D. E. Newman, and D. P. Stotler, Phys. Plasmas **15**, 062503 (2008).

[263]M. Greenwald, Phys. Plasmas **17**, 058101 (2010).

[264]G. Bateman, A. H. Kritz, J. E. Kinsey, and A. J. Redd, Phys. Plasmas **5**, 2355 (1998).

[265]A. M. Dimits, G. Bateman, M. A. Beer, B. I. Cohen, W. Dorland, G. W. Hammett, C. Kim, J. E. Kinsey, M. Kotschenreuther, A. H. Kritz *et al.*, Phys. Plasmas **7**, 969 (2000).

[266]D. Mikkelsen, W. Dorland, W. Ross, M. Greenwald, S. Wolfe, P. Bonoli, C. Fiore, A. Hubbard, I. Irby, E. Marmar *et al.*, in *Proceedings of the 19th*

[266]*IAEA Fusion Energy Conference* (IAEA, 2002), see http://www-pub.iaea.org/MTCD/publications/PDF/csp_019c/pdf/exp5_03.pdf.

[267]N. T. Howard, A. E. White, M. Greenwald, C. Holland, J. Candy, and J. Rice, Plasma Phys. Control. Fusion **56**, 124004 (2014).

[268]N. T. Howard, M. Greenwald, D. R. Mikkelsen, A. E. White, M. L. Reinke, D. Ernst, Y. Podpaly, and J. Candy, Phys. Plasmas **19**, 056110 (2012).

[269]N. T. Howard, A. E. White, M. Greenwald, M. L. Reinke, J. Walk, C. Holland, J. Candy, and T. Gorler, Phys. Plasmas **20**, 032510 (2013).

[270]J. Candy and R. E. Waltz, Phys. Rev. Lett. **91**, 045001 (2003).

[271]C. Holland, A. E. White, G. R. McKee, M. W. Shafer, J. Candy, R. E. Waltz, L. Schmitz, and G. R. Tynan, Phys. Plasmas **16**, 052301 (2009).

[272]T. L. Rhodes, C. Holland, S. P. Smith, A. E. White, K. H. Burrell, J. Candy, J. C. DeBoo, E. J. Doyle, J. C. Hillesheim, J. E. Kinsey *et al.*, Nucl. Fusion **51**, 063022 (2011).

[273]D. A. Batchelor, M. Beck, A. Becoulet, R. V. Budny, C. S. Chang, P. H. Diamond, J. Q. Dong, G. Y. Fu, A. Fukuyama, T. S. Hahm *et al.*, Plasma Sci. Technol. **9**, 312 (2007).

[274]N. T. Howard, A. E. White, M. Greenwald, C. Holland, and J. Candy, Phys. Plasmas **21**, 032308 (2014).

[275]N. T. Howard, C. Holland, A. E. White, M. Greenwald, and J. Candy, "Synergistic Cross-Scale Coupling of Turbulence in a Tokamak Plasma," Phys. Plasmas (to be published).

[276]L. Lin, M. Porkolab, E. M. Edlund, J. C. Rost, M. Greenwald, N. Tsujii, J. Candy, R. E. Waltz, and D. R. Mikkelsen, Plasma Phys. Controlled Fusion **51**, 065006 (2009).

[277]J. E. Rice, I. Cziegler, P. H. Diamond, B. P. Duval, Y. A. Podpaly, M. L. Reinke, P. C. Ennever, M. J. Greenwald, J. W. Hughes, Y. Ma *et al.*, Phys. Rev. Lett. **107**, 265001 (2011).

[278]M. Porkolab, J. Dorris, P. Ennever, C. Fiore, M. Greenwald, A. Hubbard, Y. Ma, E. Marmar, Y. Podpaly, M. L. Reinke *et al.*, Plasma Phys. Controlled Fusion **54**, 124029 (2012).

[279]D. R. Ernst, S. Batha, M. Beer, M. G. Bell, R. E. Bell, R. V. Budny, B. Coppi, W. Dorland, P. C. Efthimion, T. S. Hahm *et al.*, in *Proceedings of the 17th IAEA Fusion Energy Conference* (IAEA, Yokahama, 1998), see http://www-pub.iaea.org/MTCD/publications/PDF/csp_008c/fec1998/pdf/exp1_14.pdf.

[280]G. McKee, K. Burrell, R. Fonck, G. Jackson, M. Murakami, G. Staebler, D. Thomas, and P. West, Phys. Rev. Lett. **84**, 1922 (2000).

[281]A. E. White, N. T. Howard, D. R. Mikkelsen, M. Greenwald, J. Candy, and R. E. Waltz, Plasma Phys. Controlled Fusion **53**, 115003 (2011).

[282]D. Ernst, Bull. Am. Phys. Soc. **57**, 73 (2012).

[283]P. H. Diamond, C. J. McDevitt, O. D. Gurcan, T. S. Hahm, W. X. Wang, E. S. Yoon, I. Holod, Z. Lin, V. Naulin, and R. Singh, Nucl. Fusion **49**, 045002 (2009).

[284]O. D. Gurcan, P. H. Diamond, P. Hennequin, C. J. McDevitt, X. Garbet, and C. Bourdelle, Phys. Plasmas **17**, 112309 (2010).

[285]A. E. White, N. T. Howard, M. Greenwald, M. L. Reinke, C. Sung, S. Baek, M. Barnes, J. Candy, A. Dominguez, D. Ernst *et al.*, Phys. Plasmas **20**, 056106 (2013).

[286]M. Barnes, F. I. Parra, J. P. Lee, E. A. Belli, M. F. F. Nave, and A. E. White, Phys. Rev. Lett. **111**, 055005 (2013).

[287]S. J. Wukitch, R. L. Boivin, P. T. Bonoli, J. A. Goetz, J. Irby, I. Hutchinson, Y. Lin, A. Parisot, M. Porkolab, E. Marmar *et al.*, Plasma Phys. Control. Fusion **46**, 1479 (2004).

[288]P. T. Bonoli, R. Parker, S. J. Wukitch, Y. Lin, M. Porkolab, J. C. Wright, E. Edlund, T. Graves, L. Lin, J. Liptac *et al.*, Fusion Sci. Technol. **51**, 401 (2007).

[289]S. J. Wukitch, P. T. Bonoli, C. Fiore, I. H. Hutchinson, Y. Lin, E. Marmar, A. Parisot, M. Porkolab, J. Rice, G. Schilling *et al.*, Radio Freq. Power Plasmas **694**, 178 (2003).

[290]S. J. Wukitch, B. Lipschultz, E. Marmar, Y. Lin, A. Parisot, M. Reinke, J. Rice, and J. Terry, J. Nucl. Mater. **363–365**, 491 (2007).

[291]Y. Lin, A. Binus, A. Parisot, and S. Wukitch, Radio Freq. Power Plasmas **933**, 187 (2007).

[292]Y. Lin, J. A. Stillerman, A. Binus, A. Parisot, and S. Wukitch, Fusion Eng. Des. **83**, 241 (2008).

[293]Y. Takase, P. T. Bonoli, A. Hubbard, A. Mazurenko, P. J. OShea, I. Porkolab, J. Reardon, S. Wukitch, R. Boivin, F. Bombarda *et al.*, in *Proceedings of the 12th Topical Conference on Radio Frequency Power in Plasmas* (AIP, Savannah, 1997), Vol. 403, p. 33.

[294]S. J. Wukitch, R. L. Boivin, P. T. Bonoli, C. Fiore, M. Greenwald, J. A. Goetz, J. Hosea, A. Hubbard, I. H. Hutchinson, J. Irby *et al.*, Radio Freq. Power Plasmas **595**, 43 (2001).

[295]S. Wukitch, Y. Lin, M. Reinke, J. Terry, G. Wallace, I. Cziegler, I. Faust, M. Garrett, J. Hillairet, C. Lau *et al.*, in *Proceedings of the 24th IAEA Fusion Energy Conference* (IAEA, San Diego, 2012), p. 406 (2012), http://www-naweb.iaea.org/napc/physics/FEC/FEC2012/papers/287_FTP11.pdf.

[296]S. J. Wukitch, P. T. Bonoli, M. Porkolab, C. K. Phillips, G. Schilling, J. R. Wilson, and Y. Takase, in Proceedings of the 2nd Europhysics Topical Conference on Radio Frequency Heating and Current Drive of Fusion Devices (European Physical Society, 1998).

[297]M. Porkolab, C. Fiore, M. Greenwald, J. C. Hosea, A. Hubbard, I. Hutchinson, J. Irby, E. Nelson-Melby, E. Marmar, C. K. Phillips *et al.*, Radio Freq. Power Plasmas **485**, 79 (1999).

[298]P. T. Bonoli, M. Brambilla, E. Nelson-Melby, C. K. Phillips, M. Porkolab, G. Schilling, G. Taylor, S. J. Wukitch, R. L. Boivin, C. J. Boswell *et al.*, Phys. Plasmas **7**, 1886 (2000).

[299]Y. Lin, S. J. Wukitch, P. T. Bonoli, E. Marmar, D. Mossessian, E. Nelson-Melby, P. Phillips, M. Porkolab, G. Schilling, S. Wolfe *et al.*, Plasma Phys. Controlled Fusion **45**, 1013 (2003).

[300]Y. Lin, S. J. Wukitch, P. T. Bonoli, A. Mazurenko, E. Nelson-Melby, A. Porkolab, J. C. Wright, I. H. Hutchinson, E. S. Marmar, D. Mossessian *et al.*, Radio Freq. Power Plasmas **694**, 50 (2003).

[301]S. J. Wukitch, Y. Lin, A. Parisot, J. C. Wright, P. T. Bonoli, M. Porkolab, N. Basse, E. Edlund, A. Hubbard, L. Lin *et al.*, Phys. Plasmas **12**, 056104 (2005).

[302]T. H. Stix, Phys. Fluids B **2**, 1729 (1990).

[303]T. H. Stix, *Waves in Plasmas* (AIP Publishing, New York, 1992).

[304]J. C. Wright, P. T. Bonoli, M. Brambilla, F. Meo, E. D'Azevedo, D. B. Batchelor, E. F. Jaeger, L. A. Berry, C. K. Phillips, and A. Pletzer, Phys. Plasmas **11**, 2473 (2004).

[305]J. C. Wright, P. T. Bonoli, E. D'Azevedo, and M. Brambilla, Comput. Phys. Commun. **164**, 330 (2004).

[306]E. Nelson-Melby, M. Porkolab, P. T. Bonoli, Y. Lin, A. Mazurenko, and S. J. Wukitch, Phys. Rev. Lett. **90**, 155004 (2003).

[307]E. F. Jaeger, L. A. Berry, S. D. Ahern, R. F. Barrett, D. B. Batchelor, M. D. Carter, E. F. D'Azevedo, R. D. Moore, R. W. Harvey, J. R. Myra *et al.*, Phys. Plasmas **13**, 056101 (2006).

[308]F. W. Perkins, Nucl. Fusion **17**, 1197 (1977).

[309]Y. Lin, S. Wukitch, A. Parisot, J. C. Wright, N. Basse, P. Bonoli, E. Edlund, L. Lin, M. Porkolab, G. Schilling *et al.*, Plasma Phys. Controlled Fusion **47**, 1207 (2005).

[310]V. Tang, J. Liptac, R. R. Parker, P. T. Bonoli, C. L. Fiore, R. S. Granetz, J. H. Irby, Y. Lin, S. J. Wukitch, and C. M. T. Alcator, Rev. Sci. Instrum. **77**, 083501 (2006).

[311]G. W. Hammett, Ph.D. thesis, Princeton University, University Microfilms No. GAX86–12694, 1986.

[312]R. Harvey and M. McCoy, in Proceedings of the IAEA Technical Committee Meeting on Advances in Simulation and Modeling of Thermonuclear Plasmas (IAEA, Montreal, 1992), p. 489.

[313]V. Tang, R. R. Parker, P. T. Bonoli, J. C. Wright, R. S. Granetz, R. W. Harvey, E. F. Jaeger, J. Liptac, C. L. Fiore, M. Greenwald *et al.*, Plasma Phys. Controlled Fusion **49**, 873 (2007).

[314]A. Bader, R. S. Granetz, R. R. Parker, P. T. Bonoli, I. H. Hutchinson, J. Sears, and S. J. Wukitch, Nucl. Fusion **52**, 094019 (2012).

[315]J. C. Wright, A. Bader, L. A. Berry, P. T. Bonoli, R. W. Harvey, E. F. Jaeger, J. P. Lee, A. Schmidt, E. D'Azevedo, I. Faust *et al.*, Plasma Phys. Controlled Fusion **56**, 045007 (2014).

[316]M. Choi, D. Green, W. W. Heidbrink, R. Harvey, D. Liu, V. S. Chan, L. A. Berry, F. Jaeger, L. L. Lao, R. I. Pinsker *et al.*, Phys. Plasmas **17**, 056102 (2010).

[317]R. Harvey, Y. Petrov, E. Jaeger, P. Bonoli, A. Bader, and RF-SciDAC, in Proceedings of the 24th Fusion Energy Conference (IAEA, San Diego, 2012), p. 374, see http://www-naweb.iaea.org/napc/physics/FEC/FEC2012/papers/207_THP608.pdf.

[318]P. J. OShea, P. Bonoli, A. Hubbard, M. Porkolab, and Y. Takase, in Proceedings of the 11th Conference on Radio Frequency Power in Plasmas (AIP, 1997), Vol. 403, p. 89.

[319]M. Brambilla, Plasma Phys. Controlled Fusion **41**, 1 (1999).

[320]E. J. Strait, T. S. Taylor, A. D. Turnbull, J. R. Ferron, L. L. Lao, B. Rice, O. Sauter, S. J. Thompson, and D. Wroblewski, Phys. Rev. Lett. **74**, 2483 (1995).

[321]B. P. LeBlanc, R. E. Bell, S. Bernabei, J. C. Hosea, R. Majeski, M. Ono, C. K. Phillips, J. H. Rogers, G. Schilling, C. H. Skinner *et al.*, Phys. Rev. Lett. **82**, 331 (1999).

[322]L. A. Berry, E. F. Jaeger, and D. B. Batchelor, Phys. Rev. Lett. **82**, 1871 (1999).

[323]E. F. Jaeger, L. A. Berry, J. R. Myra, D. B. Batchelor, and E. D'Azevedo, in *Proceedings of the 15th Topical Conference on Radio Frequency Power in Plasmas*, edited by C. B. Forest (Amer Inst Physics, Melville, 2003), Vol. 694, p. 475.

[324]Y. Lin, J. E. Rice, S. J. Wukitch, M. J. Greenwald, A. E. Hubbard, A. Ince-Cushman, L. Lin, M. Porkolab, M. L. Reinke, and N. Tsujii, Phys. Rev. Lett. **101**, 235002 (2008).

[325]Y. Lin, J. E. Rice, S. J. Wukitch, M. J. Greenwald, A. E. Hubbard, A. Ince-Cushman, L. Lin, E. S. Marmar, M. Porkolab, M. L. Reinke *et al.*, Phys. Plasmas **16**, 056102 (2009).

[326]Y. Lin, J. E. Rice, S. J. Wukitch, M. L. Reinke, M. J. Greenwald, A. E. Hubbard, E. S. Marmar, Y. Podpaly, M. Porkolab, N. Tsujii *et al.*, Nucl. Fusion **51**, 063002 (2011).

[327]J. Adam, Plasma Phys. Controlled Fusion **29**, 443 (1987).

[328]B. Lipschultz, Y. Lin, E. S. Marmar, D. G. Whyte, S. Wukitch, I. H. Hutchinson, J. Irby, B. LaBombard, M. L. Reinke, J. L. Terry *et al.*, J. Nucl. Mater. **363–365**, 1110 (2007).

[329]S. J. Wukitch, Y. Lin, B. Lipschultz, A. Parisot, M. Reinke, P. T. Bonoli, M. Porkolab, I. H. Hutchinson, E. Marmar, and A. C.-M. Team, Radio Freq. Power Plasmas **933**, 75 (2007).

[330]S. J. Wukitch, B. LaBombard, Y. Lin, B. Lipschultz, E. Marmar, M. L. Reinke, D. G. Whyte, and A. C.-M. Team, J. Nucl. Mater. **390–391**, 951 (2009).

[331]F. Waelbroeck, J. Winter, G. Esser, B. Giesen, L. Konen, V. Philipps, U. Samm, J. Schluter, P. Weinhold, and T. Banno, Plasma Phys. Controlled Fusion **31**, 185 (1989).

[332]F. W. Perkins, Nucl. Fusion **29**, 583 (1989).

[333]H. Kohno, J. R. Myra, and D. A. D'Ippolito, Phys. Plasmas **19**, 012508 (2012).

[334]R. Ochoukov, D. G. Whyte, D. Brunner, I. Cziegler, B. LaBombard, B. Lipschultz, J. Myra, J. Terry, and S. Wukitch, J. Nucl. Mater. **438**, S875 (2013).

[335]J. R. Myra and D. A. D'Ippolito, Phys. Rev. Lett. **101**, 195004 (2008).

[336]R. Ochoukov, D. Whyte, D. Brunner, D. D'Ippolito, B. LaBombard, B. Lipschultz, J. Myra, J. Terry, and S. Wukitch, Plasma Phys. Controlled Fusion **56**, 015004 (2014).

[337]D. A. D'Ippolito, J. R. Myra, R. Ochoukov, and D. G. Whyte, Plasma Phys. Controlled Fusion **55**, 015004 (2013).

[338]J. Terry, I. Cziegler, S. Wukitch, M. Garrett, C. Lau, Y. Lin, R. Ochoukov, D. Whyte, and S. Zweben, in *Proceedings of the 24th IAEA Fusion Energy Conference* (IAEA, San Diego, 2012), see http://www-naweb.iaea.org/napc/physics/FEC/FEC2012/papers/46_EXP539.pdf.

[339]M. L. Garrett and S. J. Wukitch, Fusion Eng. Des. **87**, 1570 (2012).

[340]S. J. Wukitch, M. L. Garrett, R. Ochoukov, J. L. Terry, A. Hubbard, B. Labombard, C. Lau, Y. Lin, B. Lipschultz, D. Miller *et al.*, Phys. Plasmas **20**, 056117 (2013).

[341]A. Bader, P. T. Bonoli, R. S. Granetz, R. W. Harvey, E. F. Jaeger, R. Parker, and S. J. Wukitch, in *Proceedings of the 19th Topical Conference on Radio Frequency Power in Plasmas* (2011), Vol. 1406.

[342]C. Gormezano, Plasma Phys. Controlled Fusion **28**, 1365 (1986).

[343]J. R. Wilson, R. R. Parker, P. T. Bonoli, A. E. Hubbard, J. W. Hughes, A. Ince-Cushman, C. Kessel, J. S. Ko, O. Meneghini, M. Porkolab *et al.*, Radio Freq. Power Plasmas **1187**, 327 (2009).

[344]P. Bonoli, Phys. Plasmas **21**, 061508 (2014).

[345]S. Shiraiwa, O. Meneghini, R. Parker, P. Bonoli, M. Garrett, M. C. Kaufman, J. C. Wright, and S. Wukitch, Phys. Plasmas **17**, 056119 (2010).

[346]O. Meneghini, S. Shiraiwa, I. Faust, R. R. Parker, A. Schmidt, and G. Wallace, Fusion Sci. Technol. **60**, 40 (2011).

[347]S. Shiraiwa, O. Meneghini, R. R. Parker, G. Wallace, J. Wilson, I. Faust, C. Lau, R. Mumgaard, S. Scott, S. Wukitch *et al.*, Nucl. Fusion **51**, 103024 (2011).

[348]C. Lau, G. R. Hanson, B. Labombard, Y. Lin, O. Meneghini, R. Ochoukov, R. Parker, S. Shiraiwa, J. Terry, G. Wallace *et al.*, Plasma Phys. Controlled Fusion **55**, 025008 (2013).

[349]C. Lau, Y. Lin, G. Wallace, S. J. Wukitch, G. R. Hanson, B. Labombard, R. Ochoukov, S. Shiraiwa, and J. Terry, Plasma Phys. Controlled Fusion **55**, 095003 (2013).

[350]P. T. Bonoli, J. Ko, R. Parker, A. E. Schmidt, G. Wallace, J. C. Wright, C. L. Fiore, A. E. Hubbard, J. Irby, E. Marmar *et al.*, Phys. Plasmas **15**, 056117 (2008).

[351]J. R. Wilson, R. Parker, M. Bitter, P. T. Bonoli, C. Fiore, R. W. Harvey, K. Hill, A. E. Hubbard, J. W. Hughes, A. Ince-Cushman *et al.*, Nucl. Fusion **49**, 115015 (2009).

[352]A. E. Schmidt, P. T. Bonoli, R. Parker, M. Porkolab, G. Wallace, J. C. Wright, J. R. Wilson, R. W. Harvey, and A. P. Smirnov, Radio Freq. Power Plasmas **1187**, 339 (2009).

[353]A. Schmidt, P. T. Bonoli, O. Meneghini, R. R. Parker, M. Porkolab, S. Shiraiwa, G. Wallace, J. C. Wright, R. W. Harvey, and J. R. Wilson, Phys. Plasmas **18**, 056122 (2011).

[354]J. S. Ko, S. Scott, M. Bitter, and S. Lerner, Rev. Sci. Instrum. **79**, 10F520 (2008).

[355]R. Parker, P. T. Bonoli, O. Meneghini, M. Porkolab, A. E. Schmidt, S. Shiraiwa, G. Wallace, J. R. Wilson, A. E. Hubbard, J. W. Hughes *et al.*, in *18th Topical Conference on Radio Frequency Power in Plasmas*, edited by V. Bobkov, and J. M. Noterdaeme (American Institute of Physics, Melville, 2009), Vol. 1187, p. 319.

[356]R. Mumgaard, S. Scott, S. Shiraiwa, G. Wallace, R. Parker, J. Hughes, and R. Granetz, in AIP Conference Proceedings (AIP, 2014), Vol. 1580, p. 394.

[357]S. Shiraiwa, G. Baek, P. T. Bonoli, I. C. Faust, A. E. Hubbard, O. Meneghini, R. R. Parker, G. M. Wallace, J. R. Wilson, R. W. Harvey *et al.*, Nucl. Fusion **53**, 113028 (2013).

[358]G. M. Wallace, R. R. Parker, P. T. Bonoli, A. E. Hubbard, J. W. Hughes, B. L. LaBombard, O. Meneghini, A. E. Schmidt, S. Shiraiwa, D. G. Whyte *et al.*, Phys. Plasmas **17**, 082508 (2010).

[359]G. M. Wallace, I. C. Faust, O. Meneghini, R. R. Parker, S. Shiraiwa, S. G. Baek, P. T. Bonoli, A. E. Hubbard, J. W. Hughes, B. L. LaBombard *et al.*, Phys. Plasmas **19**, 062505 (2012).

[360]A. P. Smirnov and R. Harvey, Bull. Am. Phys. Soc. **40**, 1837 (1995).

[361]O. Meneghini, S. Shiraiwa, and R. Parker, Phys. Plasmas **16**, 090701 (2009).

[362]J. C. Wright, P. T. Bonoli, A. E. Schmidt, C. K. Phillips, E. J. Valeo, R. W. Harvey, and M. A. Brambilla, Phys. Plasmas **16**(7), 072502 (2009).

[363]N. Bertelli, G. Wallace, P. T. Bonoli, R. W. Harvey, A. P. Smirnov, S. G. Baek, R. R. Parker, C. K. Phillips, E. J. Valeo, J. R. Wilson *et al.*, Plasma Phys. Controlled Fusion **55**, 074003 (2013).

[364]S. G. Baek, R. R. Parker, S. Shiraiwa, G. M. Wallace, P. T. Bonoli, D. Brunner, I. C. Faust, A. E. Hubbard, B. LaBombard, and M. Porkolab, Plasma Phys. Controlled Fusion **55**, 052001 (2013).

[365]S. G. Baek, R. Parker, S. Shiraiwa, G. Wallace, P. Bonoli, M. Porkolab, Y. Takase, D. Brunner, I. Faust, A. Hubbard *et al.*, Phys. Plasmas **21**, 061511 (2014).

[366]S. G. Baek, S. Shiraiwa, R. R. Parker, P. T. Bonoli, E. S. Marmar, G. M. Wallace, A. Dominguez, G. J. Kramer, and C. Lau, Phys. Plasmas **21**, 012506 (2014).

[367]Y. Takase, M. Porkolab, J. J. Schuss, R. L. Watterson, C. L. Fiore, R. E. Slusher, and C. M. Surko, Phys. Fluids **28**, 983 (1985).

[368]G. M. Wallace, S. Shiraiwa, J. Hillairet, M. Preynas, W. Beck, J. A. Casey, J. Doody, I. C. Faust, E. Fitzgerald, D. K. Johnson *et al.*, Nucl. Fusion **53**, 073012 (2013).

[369]F. C. Schuller, Plasma Phys. Controlled Fusion **37**, A135 (1995).

[370]M. A. Pick, P. Noll, P. Barabaschi, F. B. Marcus, and L. Rossi, in *Proceedings of the 14th IEE/NPSS Symposium on Fusion Engineering* (IEEE, San Diego, 1991), Vol. 1, p. 187, see http://dx.doi.org/10.1109/FUSION.1991.218918.

[371]R. S. Granetz, I. H. Hutchinson, J. Sorci, D. T. Garnier, J. H. Irby, B. LaBombard, and E. S. Marmar, in *Proceedings of the 16th IAEA Conference on Fusion Energy* (IAEA, Montreal, 1996), Vol. 1, p. 757.

[372]R. S. Granetz, I. H. Hutchinson, J. Sorci, J. H. Irby, B. LaBombard, and D. Gwinn, Nucl. Fusion **36**, 545 (1996).

[373]ITER Physics Expert Group, Nucl. Fusion **39**, 2251 (1999).

[374]V. A. Izzo, E. M. Hollmann, A. N. James, J. H. Yu, D. A. Humphreys, L. L. Lao, P. B. Parks, P. E. Sieck, J. C. Wesley, R. S. Granetz *et al.*, Nucl. Fusion **51**, 063032 (2011).

[375]J. W. Connor and R. J. Hastie, Nucl. Fusion **15**, 415 (1975).

[376]R. Granetz, B. Esposito, J. H. Kim, R. Koslowski, M. Lehnen, J. Martin-Solis, C. Paz-Soldan, T. Rhee, J. Wesley, and L. Zeng, Phys. Plasmas **21**, 072506 (2014).

[377]S. L. Milora, S. K. Combs, and C. R. Foust, Rev. Sci. Instrum. **57**, 2356 (1986).

[378]D. G. Whyte, T. C. Jernigan, D. A. Humphreys, A. W. Hyatt, C. J. Lasnier, P. B. Parks, T. E. Evans, M. N. Rosenbluth, P. L. Taylor, A. G. Kellman *et al.*, Phys. Rev. Lett. **89**, 055001 (2002).

[379]R. Granetz, D. G. Whyte, V. A. Izzo, T. Biewer, M. L. Reinke, J. Terry, A. Bader, M. Bakhtiari, T. Jernigan, and G. Wurden, Nucl. Fusion **46**, 1001 (2006).

[380]D. G. Whyte, R. Granetz, M. Bakhtiari, V. Izzo, T. Jernigan, J. Terry, M. Reinke, and B. Lipschultz, J. Nucl. Mater. **363–365**, 1160 (2007).

[381]M. Bakhtiari, G. Olynyk, R. Granetz, D. G. Whyte, M. L. Reinke, K. Zhurovich, and V. Izzo, Nucl. Fusion **51**, 063007 (2011).

[382]A. H. Glasser, C. R. Sovinec, R. A. Nebel, T. A. Gianakon, S. J. Plimpton, M. S. Chu, D. D. Schnack, and N. Team, Plasma Phys. Controlled Fusion **41**, A747 (1999).

[383]V. A. Izzo, Nucl. Fusion **46**, 541 (2006).

[384]V. A. Izzo, D. G. Whyte, R. S. Granetz, P. B. Parks, E. M. Hollmann, L. L. Lao, and J. C. Wesley, Phys. Plasmas **15**, 056109 (2008).

[385]M. L. Reinke, D. G. Whyte, R. Granetz, and I. H. Hutchinson, Nucl. Fusion **48**, 125004 (2008).

[386]G. M. Olynyk, R. S. Granetz, M. L. Reinke, D. G. Whyte, T. Golfinopoulos, J. W. Hughes, J. R. Walk, V. A. Izzo, S. K. Combs, S. L. Milora *et al.*, Nucl. Fusion **53**, 092001 (2013).

[387]J. L. Terry, B. LaBombard, B. Lipschultz, M. J. Greenwald, J. E. Rice, and S. J. Zweben, Fusion Sci. Technol. **51**, 342 (2007).

[388]M. Greenwald, R. Boivin, P. Bonoli, C. Fiore, J. Goetz, R. Granetz, A. Hubbard, I. Hutchinson, J. Irby, Y. Lin *et al.*, Plasma Phys. Controlled Fusion **42**, A263 (2000).

[389]J. E. Rice, J. L. Terry, E. S. Marmar, and F. Bombarda, Nucl. Fusion **37**, 241 (1997).

[390]M. L. Reinke, I. H. Hutchinson, J. E. Rice, N. T. Howard, A. Bader, S. Wukitch, Y. Lin, D. C. Pace, A. Hubbard, J. W. Hughes *et al.*, Plasma Phys. Controlled Fusion **54**, 045004 (2012).

[391]M. L. Reinke, J. E. Rice, I. H. Hutchinson, M. Greenwald, N. T. Howard, J. W. Hughes, J. Irby, Y. Podpaly, J. L. Terry, and A. White, Nucl. Fusion **53**, 043006 (2013).

[392]J. E. Rice, K. B. Fournier, J. A. Goetz, E. S. Marmar, and J. L. Terry, J. Phys. B: At., Mol. Opt. Phys. **33**, 5435 (2000).

[393]J. E. Rice, I. L. Terry, K. B. Fournier, and E. S. Marmar, Fusion Sci. Technol. **51**, 451 (2007).

[394]J. E. Rice, M. L. Reinke, J. M. A. Ashbourn, A. C. Ince-Cushman, Y. A. Podpaly, M. F. Gu, M. Bitter, K. Hill, and E. Rachlew, J. Phys. B: At., Mol. Opt. Phys. **44**, 165702 (2011).

[395]J. E. Rice, M. L. Reinke, J. M. A. Ashbourn, C. Gao, M. M. Victora, M. A. Chilenski, L. Delgado-Aparicio, N. T. Howard, A. E. Hubbard, J. W. Hughes *et al.*, J. Phys. B: At., Mol. Opt. Phys. **47**, 075701 (2014).

[396]Y. Takase, S. N. Golovato, M. Porkolab, K. Bajwa, H. Becker, and D. Caldwell, in *Proceedings of the 9th Topical Conference on Radio Frequency Power in Plasmas* (Charleston, 1992), Vol. 244, p. 189.

[397]S. N. Golovato, M. Porkolab, Y. Takase, R. Boivin, F. Bombarda, P. Bonoli, C. Christensen, C. Fiore, D. Garnier, J. Goetz *et al.*, Proceedings of the 11th Topical Conference on Radio Frequency Power in Plasmas, Palm Springs, 1996, AIP Conf. Proc. **355**, 23 (1996).

[398]N. Tsujii, M. Porkolab, P. T. Bonoli, Y. Lin, J. C. Wright, S. J. Wukitch, E. F. Jaeger, D. L. Green, and R. W. Harvey, Phys. Plasmas **19**, 082508 (2012).

[399]S. Shiraiwa, J. Ko, O. Meneghini, R. Parker, A. E. Schmidt, S. Scott, M. Greenwald, A. E. Hubbard, J. Hughes, Y. Ma *et al.*, Phys. Plasmas **18**, 080705 (2011).

[400]J. Stillerman and T. W. Fredian, Fusion Eng. Design **43**, 301 (1999).